Progress in Nuclear Magnetic Resonance Spectroscopy 146–147 (2025) 101557

Contents lists available at ScienceDirect

Progress in Nuclear Magnetic Resonance Spectroscopy

journal homepage: www.elsevier.com/locate/pnmrs

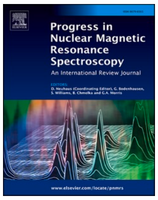

Nonlinear effects in magnetic resonance localized spectroscopy and images

Dan Eugen Demco [a,d,e], Ana-Maria Oros-Peusquens [a,e], Nadim Jon Shah [a,b,c,*]

[a] *Institute of Neuroscience and Medicines, Forschungszentrum Jülich, INM-4 52428 Jülich, Germany*
[b] *Institute of Neuroscience and Medicines, Forschungszentrum Jülich, INM-11 52428 Jülich, Germany*
[c] *Department of Neurology, RWTH Aachen University, Aachen 52074 Germany*
[d] *DWI-Leibniz Institute for Interactive Materials, RWTH Aachen University, Aachen 52074 Germany*
[e] *BrainQ, INSPIRE Platform, University Babes-Bolyai, Cluj-Napoca, Romania*

ARTICLE INFO

Edited by Steven Williams and David Neuhaus

Keywords:
NMR
Intermolecular multiple-quantum coherences
Magnetic resonance spectroscopy and images
Distant dipolar fields
Magnetic resonance thermometry
Collective effects
Hyperpolarized liquids and gases

ABSTRACT

The nonlinear effects associated with intermolecular multiple-quantum coherences (iMQCs) that are present in magnetic resonance imaging (MRI), localized spectroscopy (MRS), and spatially resolved thermometry of biological tissues are reviewed. These nonlinear effects occur especially for samples with a high concentration of resonant nuclei, at ultra-high magnetic fields or under hyperpolarization conditions. The classical Bloch equations and approaches based on quantum mechanical density operator evolution were employed for description of nonlinear effects on the spin system response in the presence of distant (long-range) dipolar field in samples containing high molecular mobility like liquids. The multiple spin echoes that appear in the presence of dipolar demagnetization fields in the presence of homogenous and heterogenous spin interactions and their applications are also discussed. One emphasis of the review is on the excitation, evolution, and detection of intermolecular zero-quantum coherences (iZQCs) and intermolecular double-quantum coherences (iDQCs) in the presence of correlated field gradients that represent the basis for CRAZED pulse sequences (*Warren et al. Science 262 (1993) 2005–2009*). The physics behind these methods employed for magnetically equivalent and non-equivalent spins, *J*-coupled spin, in homonuclear and heteronuclear systems is discussed. The principles of magnetic resonance localized spectroscopy and imaging applications for brain investigations to reduce the effect of inhomogeneous magnetic fields and to increase the image resolution is reviewed. The physics related to the used of CRAZED methods to produce fundamentally different contrast than does conventional imaging is also addressed. Collective effects in the presence of strong nuclear magnetization that can affect MRI and MRS results such as spectral clustering and spin turbulence are summarized.

Contents

---

[*] Corresponding author at: Institute of Neuroscience and Medicines, Forschungszentrum Jülich, INM-4, 52428 Jülich, Germany.
E-mail addresses: demco@dwi.rwth-aachen.de (D.E. Demco), n.j.shah@fz-juelich.de (N.J. Shah).

https://doi.org/10.1016/j.pnmrs.2025.101557
Received 30 September 2024; Accepted 9 January 2025

1. Introduction

1.1. The goal

Nuclear Magnetic Resonance (NMR) is the most versatile and widely applicable form of spectroscopy in the radio-frequency (RF) range [1–4]. This technique having a well-developed theoretical framework based mostly on a quantum-mechanics formalism, allows one to obtain information about structure and dynamics of a variety of substances having microscopic or macroscopic structures [3–10]. For liquid and gaseous samples with a high spin concentration, in the case of the NMR experiments made at ultrahigh magnetic fields (for flux density $B_0 > 20$ T), or under hyperpolarization conditions in the presence of magnetic gradients the conventional assumptions made in all experiments have to be discarded. To explain one and two-dimensional NMR experiments performed in the above conditions new assumptions need to be taken into account concerning: (i) the dipolar interactions of all spins leading to the demagnetization dipolar field and (ii) the exact description of the thermal equilibrium for the spin systems. The spin system response becomes nonlinear in the presence of multiple quantum coherences that manifest in multiple spin echoes and anomalous peaks resulting from two-dimensional pulse sequences. The discoveries of nonlinear spin echoes [11,12] and nonlinear coherence transfer echoes [13–17] open a new era in NMR leading to important applications in the field of magnetic resonance spectroscopy (MRS) and imaging (MRI). Nonlinear and collective effects in hyperpolarized liquids and gases in the presence of distant dipolar field are also reviewed in Refs. [18–20]. In conventional NMR spectroscopy nonlinear effects are well known and are represented by saturation effects, line broadening, and line shifts by strong radiofrequency perturbations. In some cases structure and dynamics of molecular systems can only be noticed through nonlinear effects, e.g. longitudinal relaxation processes and the connectivity of the various transitions in the energy level scheme [3,4].

The aim of this work is to review the physical principles and applications of the nonlinear and collective effects that occurs in spin system responses to specific pulse sequences in the presence of long-range dipolar spin interactions and to consider the exact expression for the thermal equilibrium density operator. This partially overlaps with the review of Desvaux that mainly discussed the nonlinear effects in hyperpolarized liquid state NMR [18]. However, the emphasis of the present review is more on the applications of nonlinear NMR spectroscopy including volume localized spectroscopy, imaging, and spatially resolved thermometry. The spin system response is mainly discussed using the fully justified formalism of quantum statistical mechanics even though the classical magnetization evolution treatment leads in some cases to equivalent results [21,22]. We shall note that full quantitative agreement between experiments and simulations has only been reached with the classical formalism [21]. Collective effects in the presence of strong nuclear magnetization that can possible affect MRI and MRS are summarized such as spectral clustering, spin turbulence, and spin noise.

1.2. Long-range dipolar interactions

Interesting effects were revealed by NMR experiments when the magnetic flux density $\boldsymbol{B}_0$ acting on a diamagnetic sample by the external static magnetic field is modulated by the nuclear magnetization of the concentrated spins. The sample density magnetization is described by a vector field $\boldsymbol{M}(\boldsymbol{r})$, where the vector $\boldsymbol{r}$ defines the position of a small volume element within the sample. The change in the total magnetic flux density by the sample magnetization is associated with the demagnetization field as introduced in classical magnetostatics [22,23]. For a spherical sample the magnetization $\boldsymbol{M}(\boldsymbol{r})$ is spatially uniform and parallel to the applied field $\boldsymbol{B}_0$. The uniform internal magnetic flux is valid for an ellipsoidal sample with one of its principal axes along the external field. In the case of an infinite cylindrical sample, oriented with its long axis parallel to the applied field the magnetization is also uniform in the same direction [22]. The dipolar demagnetization field $\boldsymbol{B}_{\mathrm{d}}(\boldsymbol{r})$ that is related to $\boldsymbol{M}(\boldsymbol{r})$ depends on the spin concentration and temperature but not on the sample volume.

The nonlinear effects in liquid NMR experiments detected in multiple spin echoes or 2D intermolecular multiple quantum coherences (iMQCs) are induced by anisotropic long-range dipolar interactions or as it is sometimes called the dipolar demagnetization field (DDF) [11,22]. These effects are most strongly manifested when spatially modulated transverse magnetization evolves in the presence of similarly modulated longitudinal magnetization. The periodic modulation of the nuclear magnetization due to non-averaged DDF can be produced by the application of magnetic field gradients and radio-frequency pulses.

The long-range dipolar field is characterized by the local magnetic flux density $\boldsymbol{B}_{\mathrm{d}}(\boldsymbol{r})$ and was discovered by analyzing the origin of multiple echoes in ^{3}He [11,24] and pure water [12,25]. Furthermore, the dipolar demagnetization field was the origin of the dependence of peak frequency shifts and line shapes on the RF pulse angles in samples with high proton concentration [26]. The origin of DDF in liquid or gaseous samples, i.e. for samples with high molecular mobility, can be understood if we consider the spatial proportionality factor $\left(3cos^{2}\theta_{ij}-1\right)/r_{ij}^{3}$, of dipolar coupling between i and j spins separated by the internuclear vector $\mathbf{r}_{\mathrm{ij}}$ that makes a θ_{ij} polar angle with direction of the static magnetic field $\boldsymbol{B}_0$. In the presence of isotropic, fast molecular diffusion on the NMR time scales the dipolar interaction vanishes, i.e., $\left\langle 3cos^{2}\theta_{ij}-1\right\rangle=0$. That means the short-range dipolar interaction average to zero through molecular diffusion process. The situation is different for long-range dipolar interactions. In this case the dipolar interaction falls off as $1/r_{ij}^{3}$, but the total number of spins at a given distance $|\boldsymbol{r}|$ is proportional to $\left|\boldsymbol{r}^{2}\right|$, and therefore produces a divergent total radial distribution [14]. This is valid for internuclear distances larger than the distance molecules diffuse on an NMR timescale [11]. Nevertheless, for a sample with uniform spin density the angular part of the total DDF vanishes. If the spatial spin distribution is made nonuniform by the combination of multiple pulses and field gradients long-range dipolar effects can reappear [13–16].

The nonlocal dipolar demagnetization field $\boldsymbol{B}_{\mathrm{d}}(\boldsymbol{r})$ is related to sample magnetization $\boldsymbol{M}(\boldsymbol{r})$, and can be written in the secular approximation [11,14,16],

$$B_{d}(\boldsymbol{r})=\frac{\mu_{0}}{4\pi}\int d^{3}r'\,\frac{1-3\cos^{2}\theta_{rr'}}{2|\boldsymbol{r}-\boldsymbol{r}'|^{3}}\left[3M_{z}(\boldsymbol{r}')\widehat{\boldsymbol{z}}-M(\boldsymbol{r}')\right] \tag{1}$$

A spatial Fourier transform simplifies the relation between $\boldsymbol{B}_{\mathrm{d}}(\boldsymbol{r})$ and $\boldsymbol{M}(\boldsymbol{r})$ as given below

$$\boldsymbol{B}_{d}(\boldsymbol{k})=\int d^{3}r\exp(i\boldsymbol{k}\cdot\boldsymbol{r})\boldsymbol{B}_{d}(\boldsymbol{r}) \tag{2}$$

$$\boldsymbol{M}(\boldsymbol{k})=\int d^{3}r\exp(i\boldsymbol{k}\cdot\boldsymbol{r})\boldsymbol{M}(\boldsymbol{r}) \tag{3}$$

From the above relations it is possible to write [11],

$$\boldsymbol{B}_{d}(\boldsymbol{k})=\frac{1}{3}\mu_{0}\Delta_{k}\left[3M_{z}(\boldsymbol{k})\widehat{\boldsymbol{z}}-\frac{1}{3}\boldsymbol{M}(\boldsymbol{k})\right] \tag{4}$$

where Δ_{k} is the second order Legendre polynomial of variable $(\boldsymbol{k}\cdot\widehat{\boldsymbol{z}})/|\boldsymbol{k}|$. When the magnetization $\boldsymbol{M}(\boldsymbol{r})$ is spatially modulated in a single direction $\boldsymbol{s}$, as will happen if gradient pulses are applied, Fourier transformation back into the spatial domain will create a local relation for $\boldsymbol{B}_{\mathrm{d}}(\boldsymbol{r})$, that depends only on the variable $\boldsymbol{r}\cdot\boldsymbol{s}=s$. The local DDF is given by

$$\boldsymbol{B}_{d}(s)=\frac{1}{3}\mu_{0}\Delta\left[3M_{z}(s)\widehat{\boldsymbol{z}}-\boldsymbol{M}(s)\right] \tag{5}$$

where $\Delta=\left[3(\boldsymbol{s}\cdot\widehat{\boldsymbol{z}})^{2}-1\right]/2$. The dipolar field $\boldsymbol{B}_{d}(s)$ gives an additional contribution $[\boldsymbol{M}\times\gamma\boldsymbol{B}_{\mathrm{d}}(\boldsymbol{r})]$ to the Bloch equations and therefore, only $\mathbf{M}_{\mathrm{z}}(s)$ in Eq. (5) matters in generating a resonance frequency variation across the sample at maximum when the gradient is applied parallel to the $\boldsymbol{B}_0$ field, i.e. for $\Delta=1$. At the magic angle $\Delta=0$, and the dipolar field $\boldsymbol{B}_{d}(s)$ vanishes. Extensions of the above arguments to two spin species were given in Refs. [27,28]. When the magnetization is spatially modulated on a length scale that is small compared with any sample structure, the dipolar demagnetization field becomes local in real space and is a one dimensional function $\boldsymbol{B}_{d}(s)$ along the direction of modulation $\widehat{\boldsymbol{s}}$. Warren and coworkers mention that a correction to Eqs. (4) and (5), describing the classical dipolar demagnetization field in solution is needed because this relation has a singularity near $\boldsymbol{k}=0$, that is important if there is any average magnetization after the action of the pulse sequence [27,29]. The correction proposed for $\boldsymbol{B}_{d}(s)$ depend on the sample shape and size. Moreover, a gradient pulse of strength G and duration T will winds both the transverse and longitudinal magnetization into helices. Spins separated by half the repeat distances of these helices with correlation distances $d=\pi/\gamma\mathrm{GT}$, create detectable NMR signals [29]. The helix pitch is $p=2\pi/\gamma\mathrm{GT}$ or $p=2\pi/k$, where k is the modulation of $\boldsymbol{k}$ reciprocal space. Sample shape effects can be neglected if the sample dimensions are much bigger than the modulation period.

There are several conditions that have to be fulfilled by the dipolar demagnetization field in order for it to induce multiple spin echoes or "anomalous" cross-peaks that can be quantitatively interpreted as was initially discussed by Deville et al. [11]. The dipolar field $\boldsymbol{B}_{\mathrm{d}}(\boldsymbol{r})$, is independent of time and $\boldsymbol{B}_{d}(\boldsymbol{r})\ 4\pi\boldsymbol{M}_0$, where $\boldsymbol{M}_0$ is the thermal equilibrium magnetization of the sample. Moreover, the dipolar field $\boldsymbol{B}_{\mathrm{d}}(\boldsymbol{r})$, is negligible with respect to the gradient field variation over the size L of the sample, i.e., $GL\gg B_{\mathrm{d}}(\boldsymbol{r})$, or $\frac{4\pi M_0}{GL}\ll 1$. The condition that the dipolar demagnetization field becomes local in real space requires that $L/p\ll 1$, or $\gamma GTL\ll 1$. In the evaluation of the spin system response for 2D experiments it is convenient to introduce a new variable, the dipolar demagnetization time τ_{d} defined as $\tau_{d}=\frac{1}{\mu_{0}\gamma M_{0}}$, [16]. This time constant reflects the action of the dipolar coupling in the evolution of multiple-quantum coherences. Thus, the dipolar demagnetization field is expected to have an important effect at times $t>\tau_{\mathrm{d}}$, which must occur before relaxation effect appears. For instance, the condition for observing large multiple echoes is $t\ T_2$, which becomes $\mu_{0}\gamma M_{0}T_{2}>1$, [11].

1.3. Exact expression for multi-spin density operator at thermodynamic equilibrium

For a multispin system at temperature T, the thermal equilibrium density operator has a form different from that valid in high-temperature approximation and is generally nonlinear in the Boltzmann exponent $\frac{\hbar H}{k_{B}T}$, where $\hbar H$ is the total spin Hamiltonian dominated by the Zeeman interaction and k_{B} is the Boltzmann constant. The $\frac{\hbar\omega_{0}}{k_{B}T}$ exponent is very small of the order 10^{-4} for protons at magnetic flux density of 10 T. The high temperature approximation was used in the theoretical prediction of conventional NMR experiments in gases, liquids and solids [3–10] where nonlinear effects are weak and in conventional conditions are difficult to detect. As noted by Goldman the high temperature assumption is extremely restrictive [8]. For a spin system composed of nuclei with spin number $I=1/2$ the Zeeman energy levels have the energy ε and –ε. The eigenvalues of the total Hamiltonian describing a system of N spins can vary from $N\epsilon/\hbar$ to $-N\epsilon/\hbar$. If N is very large the difference $2N\epsilon/\hbar$ is also large even if $\left(\frac{\varepsilon}{\hbar}\right)/(k_{B}T)$ is small. Hence, the linear approximation in $\frac{\hbar H}{k_{B}T}$, is no longer justified.

A Zeeman Hamiltonian for a system of N magnetically equivalent spins is given by

$$H=\omega_{0}\sum_{i=1}^{N}I_{iz} \tag{6}$$

where ω_0 is the Larmor angular frequency and I_{iz} is the z-component of the *i*-spin operator. For a canonic spin ensemble the reduced equilibrium density operator has the general form [3,8,15,16]

$$\sigma_0 = \frac{\prod_{i=1}^{N} exp\{-\hbar\omega_0 I_{zi}/k_B T\}}{Tr\{\hbar H/k_B T\}} \tag{7}$$

If we ignore all inter-spin couplings the equation below holds,

$$\sigma_0 = \sigma_{0,1} \otimes \sigma_{0,2} \otimes \sigma_{0,3} \otimes \cdots \otimes \sigma_{0,N} \tag{8}$$

and finally it is possible to write the exact expression for multi-spin density operator at thermal equilibrium,

$$\sigma_0 = (2)^{-N} \prod_{i=1}^{N} (1 - \Im I_{zi}) \tag{9}$$

where $\Im = 2tanh\left(\frac{\hbar\omega_0}{2k_B T}\right)$, [15]. As the temperature increases the following approximation becomes valid $\Im \approx \frac{\hbar\omega_0}{2k_B T}$. The exact Eq. (7) is a product of *N*-spin operators and hence convergence is not an issue. The essential physics behind the CRAZED pulse sequence (Section 3) was described by Richter and Warren, [16] using the approximation of bilinear operators $I_{zi}I_{zj}$ in Eq. (9), that occur in connection with $\Im^2$ term. Even though the factor $\Im^2$ is about four orders of magnitude smaller than $\Im$ the number of second order terms is about N^2, and hence, the truncation to first order is in not justified. In the limit of the high-temperature approximation the density operator is proportional to the $\Im$ factor and is not a good approximation for spin systems of macroscopic size. Furthermore, the full form Eq. (7), is required for a quantum statistical description of long-range dipolar interaction effects in NMR experiments [21,30].

The general expression for multi-spin equilibrium density operator was validated a posteriori by evaluation of the 2D spin system response to the CRAZED pulse sequence [13] which is in agreement with experimental results [14–16]. However, if the initial density operator is taken in the high-temperature approximation no peaks related to multiple-quantum coherences can be predicted [15]. Moreover, the experimental confirmation of the phase signal predictions [17], shows that the nonlinear spin echoes (Section 2) provide direct evidence for the breakdown of the high temperature approximation used for the initial thermal equilibrium of multi-spin density operator.

1.4. Intermolecular multiple-quantum coherences

To explain the physics of 1D and 2D NMR experiments in liquid samples based on multi-quantum coherences in the presence of long-range dipolar couplings some rules of the multi-spin operator transformations should be taken into account [3,5–8]. For small spin numbers of molecules and clusters the following rules were proposed and are also valid for “macroscopic” or intermolecular multiple quantum coherences as given below [3,5–8].

1. Hard RF pulses can change the order *m* of multiple quantum coherences. In the free evolution periods of NMR experiments the order of multiple quantum coherences remains constant but the number of spins can increase or decrease.
2. A phase shift with angle ϕ of an RF pulse will lead for *m*-order quantum coherence to $m\phi$-fold phase-shift.
3. The evolution of multiple quantum coherences is not affected by couplings between nuclei actively involved in the transition. If total spin coherences are excited the spin dynamics are not affected by dipolar couplings or *J*-indirect couplings.
4. Multiple quantum coherences evolving under couplings to “passive” spins, will lead to multiples in the multiple quantum spectrum.
5. For *m*-order multiple quantum coherence an *m*-fold amplification of any resonance offset take place that enhances the effective strength of the field gradient. This has a beneficial effect on MRI and for the sensitivity to molecular diffusion.
6. Multiple quantum coherence relaxation contains via correlated fluctuation fields more information about molecular dynamics than conventional T_2 measurements.

NMR experiments based on multiple-quantum coherences were useful for homonuclear and heteronuclear spectral simplification and filtering, tickling, decoupling, cross-polarization, selection of multiplets, and removal of magnetic field inhomogeneity as well as increasing MRI resolution [3,5–10].

The effect of the intermolecular dipolar spin interaction on the secular approximation induced by Zeeman interaction during free evolution periods on the density operator terms that contains *n*-spins and *m*-order quantum operators was introduced and justified by Lee et al. [15]. We will summarize below these rules taking into account that in the dipolar Hamiltonian between equivalent spins the scalar term $\mathbf{I}_i \cdot \mathbf{I}_j$ can be ignored and the spin operator evolutions under the dipolar term $I_{zi}I_{zj}$ are well-know [3].

(i) The specific *n*-spin, one-quantum operator $I_{xi}, I_{zj} \ldots I_{zn}$ can be converted into an NMR observable (I_{xi} or I_{yi}) by (*n*-1) successive dipolar interactions. For instance, for an antiphase product operator of two spins *i* and *j*, we can write

$$exp\{-iD_{ij}I_{zi}I_{zj}t\}2I_{xi}I_{zj}exp\{iD_{ij}I_{zi}I_{zj}t\} = 2I_{xi}I_{zj}\cos\left(\frac{D_{ij}t}{2}\right) + I_{yi}\sin\left(\frac{D_{ij}t}{2}\right) \tag{10}$$

i.e., each dipolar operation gives an extra factor of $\sin\left(\frac{D_{ij}t}{2}\right)$, where D_{ij} is the dipolar coupling factor for *i* and *j* spins.

(ii) In the evaluation of the spin system response only the most direct route from a *n*-spin, one-quantum term to an one-spin, one-quantum term, i.e., the one with (*n*-1) commutators, need ever be considered. The assumptions $D_{ij}t \ll 1$ makes the coefficients of all the indirect pathways negligibly small.

(iii) In the case of small intermolecular dipolar couplings the only dipolar sums which lead to observable signals have the form $\Im^n \left(\sum_i D_{ij}\right)^n$.

The justification for the above rules used for the quantum–mechanical evaluation of spin system in experiments based on intermolecular multiple-quantum coherences are given in Ref. [15].

1.5. Radiation damping

One of the effect in NMR experiments that provides an important decay for the time domain signal is related to radiation damping [31,32]. The qualitative explanation of this nonlinear NMR effect is that precessing spin magnetization induces an oscillating current in the tuned radio-frequency coil, hence an oscillating RF magnetic field is produced that tends to rotate the transverse magnetization back to its thermal equilibrium direction. This collective effect induces a shift and broadening of the resonance lines as well as line-shape distortion [4,33–36]. The classical approach based on the Bloch equations has been used for analyzing quantitatively radiation damping [4,33–36]. The presence of an additional magnetic field which depends explicitly upon the average state of the spins, induces nonlinear behavior of the Bloch equation [33]. Hence, new effects due to radiation damping are present in spin-echo and 2D NMR experiments as were demonstrated in Refs. [14,33], and [36]. The effect of radiation damping in the presence of intramolecular *J*-coupled spin systems was discussed in a COSY experiment [37]. The RF field induced by radiation damping generates an effect equivalent to soft pulse with bandwidth of order $1/\tau_r$, where τ_r is the radiation damping time [14]. When the above condition is not fulfilled the cross-peaks can be detected originating from radiation damping soft pulses [37]. In this review, we will not discuss the radiation damping effects that could be of importance alone or in combination with intramolecular *J* coupling or the dipolar demagnetization field because an active electronic feedback techniques was developed to suppress this effect without hampering multiple pulse experiments [38].

2. Multiple spin echoes in the presence of long-range dipolar field

The spin echo is a fundamental phenomenon in NMR spectroscopy and imaging [3,5]. Spin echoes are produced based on the general scheme: *excitation-evolution-mixing-evolution-detection* [3–9]. The evolution of spin coherences can take place in laboratory or rotating reference frames under the effect of linear spin interactions like inhomogeneity of static magnetic fields, field gradients or heteronuclear couplings and bilinear spin interactions as *J*-indirect couplings, dipolar and quadrupolar couplings. If the quantum mechanics propagator *P*, during the mixing period is inducing a sign reversal of linear or bilinear spin interaction Hamiltonian H_i, i.e., $PH_iP^{-1} = -kH_i$, where *k* is a number, the coherence evolution during the first evolution interval is "time reversed" in the second evolution period and a spin echo is detected at the end of the last evolution period of same duration for $k = 1$. This picture changes drastically when local dipolar interactions modulated by field gradients are active in the second evolution period as these lead to nonlinear coherence evolution and finally to multiple (nonlinear) spin echoes.

The conventional Bloch equations are linear in sample magnetization $\boldsymbol{M}$, which means by taking $k\boldsymbol{M}$, the dynamics will not change. In the presence of a demagnetization field the additional term $d\boldsymbol{M}/dt = \gamma\boldsymbol{M} \times \boldsymbol{B}_d$ is nonlinear in $\boldsymbol{M}$, since considering $k\boldsymbol{M}$ will lead to $k\boldsymbol{B}_d$, where $\boldsymbol{B}_d$ is the flux density of the demagnetization field. Furthermore, in the framework of quantum mechanics the presence of $\boldsymbol{B}_d$ essentially modifies the Liouville-von Neumann equation for the density matrix. Therefore, this equation becomes nonlinear because evolution propagators depends explicitly on the initial state of the spin system.

Multiple-quantum coherences can be also refocused and detected by conversion to (-1) single-quantum coherences. In 2D NMR spectroscopy coherence transfer echoes are an important source of information about molecular structure via *J*-couplings [3]. We will review below only the single-quantum coherences refocused under multiple spin echoes in the presence of a nuclear demagnetization field.

2.1. Multiple spin echoes

The conventional spin echo or Hahn spin echo [3,39], is analyzed in the simplest case when the spins are non-interacting between themselves and single-quantum coherences evolve in the presence of magnetic linear or inhomogenous gradients. For such conditions the pulse sequence producing the spin echo is: $(\pi/2)_x - \tau\text{-}(\pi)_{x,y} - \tau$-echo-acquisition, where the phase of the refocusing π-pulse can by *x* or *y*. This spin echo is produced by "Hamiltonian time reversal". i.e. sign reversal of the dominant spin interaction, induced by the π-pulse acting on the external interactions linear in the spin operator I_z. In the presence of a long-range dipolar field induces by a field gradient the spin system response becomes nonlinear producing multiple spin echoes. A sinusoidal demagnetization field partially modulates the NMR resonance frequency so that the transverse magnetization is a superposition of helical configuration with pitch p*k*, yielding multiple echoes at time pτ, where *k* is the wave vector defined below and p is an integer.

The density operator formalism of quantum mechanics was used by Kimmich [9], to describe in an elegant manner the production of multiple spin echoes [11,12]. The pulse sequence: $(\pi/2)_x\text{-}\tau\text{-}(\pi/2)_y\text{-}t$ acting on the spin system in the presence of a local, gradient-induced frequency offset from resonance and a dipolar demagnetization field $\boldsymbol{B}_d(z) = \mu_0 M_z(z)\boldsymbol{u}_z$ where $\boldsymbol{u}_z$ is the unit vector in the direction of the z-axis defining the orientation of $\boldsymbol{B}_0$, and $M_z(z)$ is the z component of the slab of spins located at coordinate z. The spin-dependent reduced density operator $\sigma(z,\tau^+)$ just after the second $\pi/2$ RF pulse can be written as

$$\sigma(z,\tau^+) \propto I_y\cos(kz) + I_z\sin(kz), \tag{11}$$

where the wave number describing the spatial modulation of magnetization due to field gradient of strength *G* is $k = \gamma G\tau$. We note that both transverse and longitudinal magnetization that can be computed from Eq. (11) are spatially modulated and the effect of long-range dipolar fields can be neglected. The *z* component of magnetization is given by

$$M_z(z,\tau^+) = N\gamma\hbar Tr\{\sigma(z,\tau^+)I_z\} \tag{12}$$

and from Eq. (11) and Eq. (12), we obtain

$$M_z(z,\tau^+) = M_0\sin(kz) \tag{13}$$

Equation (13) shows that the effect of the gradient is to break the rotational symmetry of magnetization around $\boldsymbol{B}_0$, inducing a spin magnetization grid. The long-range dipolar interaction generated by the spatially encoded spin magnetization can be written as

$$\boldsymbol{B}_d(z) = \mu_0 M_z(z)\boldsymbol{u}_z \tag{14}$$

From Eq. (14) we obtain the total offset of the magnetic flux density at a position *z* in the sample,

$$\Delta B_d(z) = \frac{\Omega_d + \Omega_G}{\gamma} \tag{15}$$

In the above Equation, $\Omega_d = \gamma\mu_o M_0\sin(\Omega_G\tau)$, and $\Omega_G = Gz$. In the detection period of duration *t*, after the second pulse the spatially modulated density operator is given by

$$\sigma(z,\tau+t) = exp\{i(\Omega_d+\Omega_G)tI_z\}\sigma(z,\tau^+)exp\{-i(\Omega_d+\Omega_G)tI_z\} \tag{16}$$

The single-quantum coherence (SQC) related to the *z* localized signal $\langle I_-(z,t)\rangle$, can be easily evaluated from Eq. (16), *i.e.*, $\langle I_-(z,\ t)\rangle = Tr\{I_-\sigma(z,\tau+t)\}$. For the NMR signal of the whole sample, the average over all *z* position in other words over all phase angles $\Omega_G\tau$, has to be taken. The only detected SQC that survive this spatial averaging have the phase factor given by the Fourier series

$$exp\{i\Omega_G t\}exp\{-i(\Omega_G\tau - \Omega_d t)\} = exp\{i\Omega_G t\}\sum_{m=-\infty}^{\infty} a_m exp\{-im\tau\} \tag{17}$$

The spatial average of the right-hand side of Eq. (17), vanishes unless the relation $\Omega_G t = m\Omega_G\tau$, is fulfilled at the detection time $t = m\tau$, for $m = 1$, 2, 3,…. Hence, multiple spin echoes are detected at integer multiple of the pulse spacing. The amplitude of the spin echo of order *m* is given by the Fourier coefficient

$$a_m = \frac{1}{2\pi}\int_{-\pi}^{\pi} exp\{i(\Omega_d t - \Omega_G\tau\}d(\Omega_G\tau), \tag{18}$$

that is a nonlinear function of the modulations induced by distant dipolar field and gradient. Moreover, Ω_d, being proportional to $\sin(\Omega_G\tau)$, is a nonlinear function of Ω_G. Multiple spin echoes arise after nonlinear evolution of coherences in the presence of the modulated long-range dipolar field [9]. The amplitude of multiple spin echoes depend solely on the ratio $\frac{\Omega_d}{\Omega_G}$, [9].

These multiple echoes were observed for the first time in solid ^{3}He in the mK temperature range and can be explained within the theoretical framework of paramagnetic phase [24]. These types of nonlinear spin echoes were also observed in liquid ^{3}He below 300 mK, generated by Fermi-liquid interaction at the transition to the collisionless regime, and long-range dipolar fields in the slow spin diffusion regime at higher

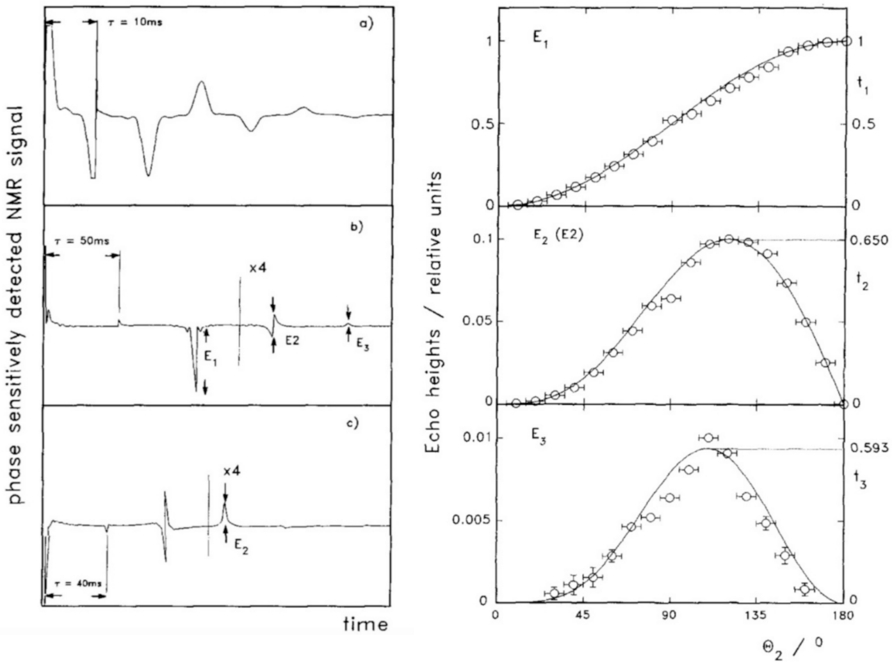

Fig. 1. Left-hand panels: Multiple spin echoes labeled as E_1, E_2, and E_3, for ^{1}H in water at 293 K and resonance frequency of 200 MHz produced by two π/2 RF pulses separated by a τ interval in the presence of the magnetic field gradient applied along B_0. The pulse-pair repetition time is short (a) or long (b, c) compared with T_1 and T_2. The in-phase and quadrature signals are shown in b) and c), respectively. Right-hand panels: Relative echo amplitude as a function of the flip angle of the second RF pulse. The tipping angle for the first pulse was π/2, $\tau = 40$ ms, and $G_z = 2.55\text{x}10^{-3}$ T/m. The solid lines give the tipping angle dependences of the theoretical functions evaluated in Ref. [25]. Adapted from [25] with permission.

temperature [12]. In these samples the local long-range dipolar field is relatively intense due to the comparatively large nuclear magnetization reached at low temperatures. The Bloch-Torrey equations can describe the production of multiple spin echoes encoded by relaxation and diffusion in the framework of classical formalism [25].

Multiple spin echoes generated by the long-range dipolar field have been studied in pure water in high magnetic field [25]. The results are shown in Fig. 1 (left-hand panels) for the first three spin echoes. The echo amplitude was evaluated as a function of the second tipping angle based on nonlinear Bloch equations and the results are also shown in Fig. 1 (right-hand panels).

Spatially modulated long-range dipolar interactions in liquids have recently offered the possibility to obtain structural information on porous media through the two-pulse sequence 90°-τ-120°, that in the presence of a field gradient G refocused a train of echoes at multiple integer values of time τ [40,41]. The second echo shape is modulated by dips. The physical explanation given by Maraviglia and coworkers [40] concerns the relation that occurs between the average pore size and the time positions of the dips through the correlation distance $d = \pi/\gamma G\tau$, defined as half a cycle of the dipolar magnetization helix. When the correlation distance d approaches the average pore size, the second nonlinear echo shows a drop in the intensity. In the case when the correlation distance affected by gradient strength becomes smaller than the pore dimensions, the spins are not subject to internal gradients and the second echo approaches that of a homogeneous sample.

Nonlinear spin echoes can also be generated in heteronuclear spin systems [41–44]. Heteronuclear nonlinear spin echoes were reported by the Kimmich group based on the evolution of ^{13}C coherences in the presence of the spatially modulated demagnetization field originating from the ^{1}H magnetization helix [42]. The pulse sequence used for this purpose is shown in Fig. 2a. The first nonlinear ^{13}C echo amplitude oscillates as a function of the modulation period of the demagnetization field. The Fourier transform of the amplitude modulated nonlinear echo reveals a doublet with a splitting equal to the intramolecular ^{1}H–^{13}C J-coupling constant (Fig. 2b).

We can summarize the key properties of multiple spin echoes that are also present in the rotating or tilted rotation reference frames and in the case of coherence transferred echoes that are the backbone of CRAZED pulse sequences (see Section 3). (i) The multiple spin echoes represent refocused coherences, and therefore they are subject to attenuation by transverse relaxation and translational diffusion. These echoes are more sensitive to the molecular diffusion than an ordinary spin echo would be [9]. (ii) The evolution of spin system can be described quantitatively by the conventional nonlinear Bloch formalism [22,24] or alternatively by the density operator approach [9]. The advantage of the density operator formalism based on the Liouville-von Neumann equation is that a J-coupled spin system can be treated as well. (iii) The multiple spin echoes disappear when no finite gradient exists or when the long-range dipolar field is too small. The last case occurs for low external magnetic field, nuclei with low γ, low spin density, or high temperature. (iv) Multiple spin echoes can be generated in the limit of the high-temperature approximation of the thermal equilibrium density operator. (v) In the first evolution period the transverse magnetization component forms a helical structure. In the presence of field gradient the spatially encoded magnetization induces a helix structure in the distant dipolar field. The second RF pulse transform this helix into a modulated x , y, and z components of magnetization, which vary spatially sinusoidally in the z direction. This spatially modulated nuclear demagnetization field causes after the second pulse, higher harmonics of the spatial oscillation of the transverse magnetization. Multiple spin echoes appear because the phase shifts associated with the mth harmonic are compensated by Larmor precession in the magnetic field gradient after a time $m\tau$, [24]. (vi) Sample shape effects can be neglected if the sample dimension is much bigger than the modulation of the dipolar demagnetization field [22]. (vii) The echo attenuation by molecular translational diffusion is much more efficient for nonlinear echoes than for ordinary spin echo [44,45]. Remarkably, in the case of nonlinear echoes the refocusing process is spoiled by diffusion not only during the gradient intervals but also thereafter.

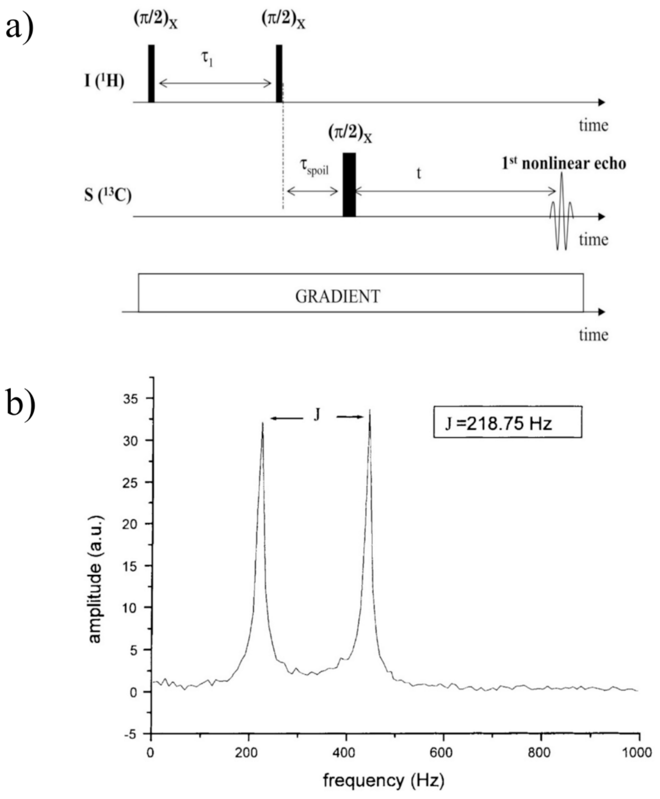

Fig. 2. A) pulse sequence applied in the presence of field gradient for the investigation of the influence of j-coupling on heteronuclear nonlinear spin echoes. b) fourier transform of the amplitude of the first heteronuclear nonlinear spin echo detected by evolution time τ_1. The sample was ^{13}C (S spins) enriched formic acid with deuterated hydroxyl groups. The remaining protons refer to the I spins. The value of the intramolecular ^{1}H–^{13}C J-coupling constant is given in the insert. Adapted from [42] with permission.

2.2. Multiple stimulated spin echoes

Similar to the case of multiple spin echoes, multiple (nonlinear) stimulated echoes (NOSE) were predicted and observed after the action of a three RF pulse sequence: $(\pi/2)_x$-τ_1-$(\pi/2)_y$-τ_2-$(\alpha)_y$-τ-(acquisition), in the presence of a constant field gradient [46,47]. The conventional stimulated echo (STE), [9] arises at time τ_1 after the third pulse, whereas the multiple stimulated echoes are generated at times $2\tau_1$, $3\tau_1$,…, $m\tau_1$. The dependence of the NOSEs as a function of the duration of the 3th RF pulse and times τ_1, and τ_2, are shown in Fig. 3, together with theoretical predictions (solid lines) as discussed in Ref. [48].

A semiclassical formalism employing the spin operators and the relaxation effects taking into account an analogy with the Block equations was used to describe the evolution of the spin system. The three-pulse sequence averaged over spatial dependence induced by the field gradient was considered in Ref. [47,48]. In the limit $\mu_0 M_0 \tau_1 \ll 1$, the following relations were derived

$$\langle(M_x+M_y)\rangle(\tau_1)=\frac{i}{2}M_0e^{-2\tau_1/T_2}e^{-\tau_2/T_1}\sin(\alpha) \qquad (19)$$

$$\langle(M_x+M_y)\rangle(2\tau_1)=-\frac{i}{4}M_0^2\gamma\mu_0M_0\tau_1e^{-4\tau_1/T_2}e^{-2\tau_2/T_1}\sin(2\alpha) \qquad (20)$$

and

$$\langle(M_x+M_y)\rangle(3\tau_1)=i\frac{9}{32}M_0^3(\gamma\mu_0M_0\tau_1)^2e^{-6\tau_1/T_2}e^{-3\tau_2/T_1}\sin(2\alpha)\cos(\alpha) \qquad (21)$$

that correspond to the amplitude of the conventional, second and third stimulated echoes, respectively [47–49]. The solid lines in Fig. 3 represent best fits of experimental multiple stimulated echoes amplitudes based on the above equations. The condition $\gamma\mu_0 M_0 \tau_1 \ll 1$, means that the first stimulated echo, to a good approximation is not affected by the demagnetization field.

The physics behind the non-linear stimulated echoes are similar to those of multiple spin echoes (Section 2.1). The local transverse magnetization develops into a spatial helix after the first pulse and static field gradient. The helix pitch is $p = 2\pi/(\gamma G \tau_1)$, and decreases with increasing evolution time. The evolution of spin coherences after the second pulse is influenced by the demagnetization field. Assuming complete relaxation of all coherences in the interval τ_2, the magnetization induced by the third pulse is split into two components modulated along the z direction of $\boldsymbol{B}_0$, and the field gradient. The transverse component (coherences) evolves in the presence of the demagnetization field created by the longitudinal component. The signal of the entire sample is determined by a spatial average over all spin positions. The coherence interference is nondestructive for $\tau = m\tau_1$, when multiple stimulated echoes will appear.

2.3. Multiple rotary spin echoes

The dephasing of the SQCs in the rotating frame under the action of a radio-frequency field gradient can be "time reversed" generating a conventional rotary spin echo [50,51]. The simplest scheme to generate such an echo is given by the pulse sequence $(\alpha(x, \tau))_x$-$(\alpha(x, \tau))_{-x}$, composed of two on-resonance RF pulses, each with a spatially distributed flip angle $\alpha(x, \tau)=\gamma(\frac{\partial B_1}{\partial x})\tau$, duration τ, having a RF gradient amplitude $\frac{\partial B_1}{\partial x}$, oriented along the x axis of rotating reference frame. The second pulse has a phase –x, that change the sign of the inhomogeneous spin Hamiltonian in the second time interval of duration τ. The total pulse sequence propagator becomes a unity operator leading at the end of the pulse sequence to the initial spin system state, i.e., to a rotary spin echo as discussed in Ref. [51,52]. Conventional rotary echoes have proved to be of interest for self-diffusion and flow measurements [51–56] as well as for NMR imaging [57,58].

The new type of nonlinear spin echoes also called multiple nutation echoes having coherence evolution in rotating and laboratory reference frames were discussed theoretically and experimentally in Refs. [59,60]. As with the other multiple echoes the origin of nonlinear rotary echoes is a consequence of coherence evolution in the modulated demagnetization field produced by the longitudinal magnetization component after the second RF pulse. The pulse sequence and field gradients are shown in Fig. 4a and the multiple rotary echoes obtained for PDMS ($M_w = 17{,}000$) in Fig. 4b. If the coherences are not completely spoiled during the evolution period τ, further echo groups having either linear or nonlinear character can be detected [59]. Besides the coherence evolution in the presence of both radiofrequency and static magnetic field [59], a rotating-frame experiment leading to multiple rotary echoes was described in Ref. [60].

3. Intermolecular multiple-quantum coherences (iMQCs) edited by CRAZED pulse sequences

Multiple-quantum coherences detected by multiple spin echoes were extended in a two-dimensional NMR experiment on liquid samples. This involves intermolecular multiple-quantum coherences (iMQCs) edited by the CRAZED (correlation spectroscopy revamped by asymmetric z-gradient echo detection) pulse sequence (Fig. 5) proposed by Warren and coworkers [13–16,61]. This nonlinear 2D pulse sequence adapted the conventional COSY sequence valid for $\theta_1 = \theta_2 = \pi/2$, $\phi_1 = \phi_2 = x$, and $\mathbf{G}_1 = \mathbf{G}_2 = 0$, (Fig. 5) to the case when long-range dipolar interaction must be taken into account. The CRAZED pulse sequence generate multiple-quantum coherences filtered by a pair of gradients and detected by coherence transfer echoes in the presence of intermolecular distant dipolar interactions. The evolution of iMQCs and intermolecular

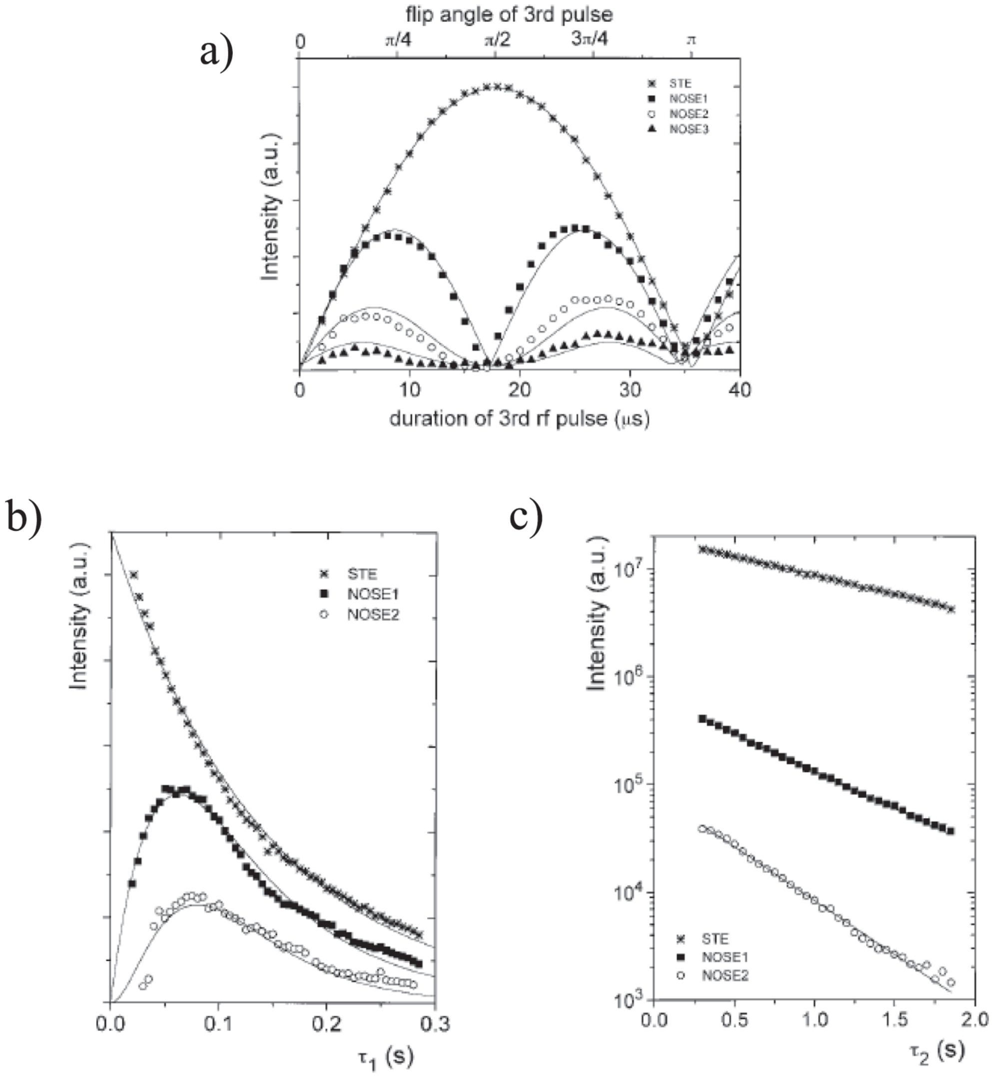

Fig. 3. a) Amplitude of multiple stimulated echoes generated by the pulse sequence $(\pi/2)_x$-τ_1-$(\pi/2)_y$-τ_2-$(\alpha)_y$-τ-(acquisition). The measured intensity are shown for the stimulated echo (STE) at $\tau = \tau_1$, and of the nonlinear stimulated echoes (NOSE1) for $\tau = 2\tau_1$, at $\tau = 3\tau_1$ (NOSE2), and at $\tau = 4\tau_1$ (NOSE3) as a function of the flip angle α of the third RF pulse. The echo intensity are not plotted to scale. Figures b) and c) show intensity of STE, NOSE1 and NOSE2 for $\alpha = \pi/4$, as a function of τ_1 and τ_2 pulses duration, respectively. Poly(dimethylsiloxane) (PDMS with $M_w = 17{,}000$) at room temperature was used as the investigated sample. For this sample it is possible to neglect signal attenuation due to self-diffusion. The solid lines and the values of τ_1 and τ_2 are explained (see text) and given in Ref. [48]. Adapted from [48] with permission.

single-quantum coherences (iSQCs) using pulsed matched gradients can be described using a quantum–mechanical formalism [13–16,45,61,62] especially when indirect *J*-couplings are present. Another equivalent approach as proved by Lee et al. [15], and Jeener [21] is based on nonlinear Bloch equations [22,63,64]. The classical formalism gives no intuition for the pulse sequence design when the sample magnetization is modulated [15]. Nevertheless, this classical approach easily incorporates radiation damping, longitudinal and transverse relaxation, and molecular diffusion. In the following we neglect these effects and concentrate on the density operator formalism for the description of the multiple-quantum coherences evolving under CRAZED and CRAZED-like pulse sequences.

We can note that the dynamics of multiple-quantum coherences in CRAZED experiment are represented by off-diagonal elements of the density operator and therefore, are quantum–mechanical entities with no corresponding classical description [45]. Furthermore, Minot et al. showed that coherence transfer echoes of CRAZED which identify the existence of intermolecular multiple quantum coherence in liquid NMR and nonlinear (multiple) spin echoes reviewed in Section 2 have a common origin [17] (see Section 3.3).

Besides long-range dipolar couplings explored in the CRAZED pulse sequence for structural and dynamical investigation of samples with large molecular translational mobility for instance in liquids, in addition a partially averaged dipolar network was investigated for medium-sized residual dipolar couplings (RDC) in soft matter. For instance, RDC in elastomers were measured using multiple-quantum (MQ) one-dimensional pulse sequences (Fig. 6), [65,66].

In the last case MQ filters are based on pulses and receiver phase cycling and buildup curves of MQ coherences are detected in a similar way as in CRAZED-like experiments [45, 64, and references therein]. The density operator formalism was used to derive the spin system response in the presence of a residual dipolar network. Nevertheless, the CRAZED MQ filters based on a pair of correlated pulse gradients are essential not only to edit the spin system response to select different orders of MQ coherences but also to produce spatially modulated demagnetization fields in liquids. Moreover, for measuring the residual dipolar couplings and their associated dynamic order parameter as discussed in Refs. [65,66], the initial spin density operator describing the thermodynamic equilibrium was used in the high-temperature approximation without employing the exact thermal equilibrium

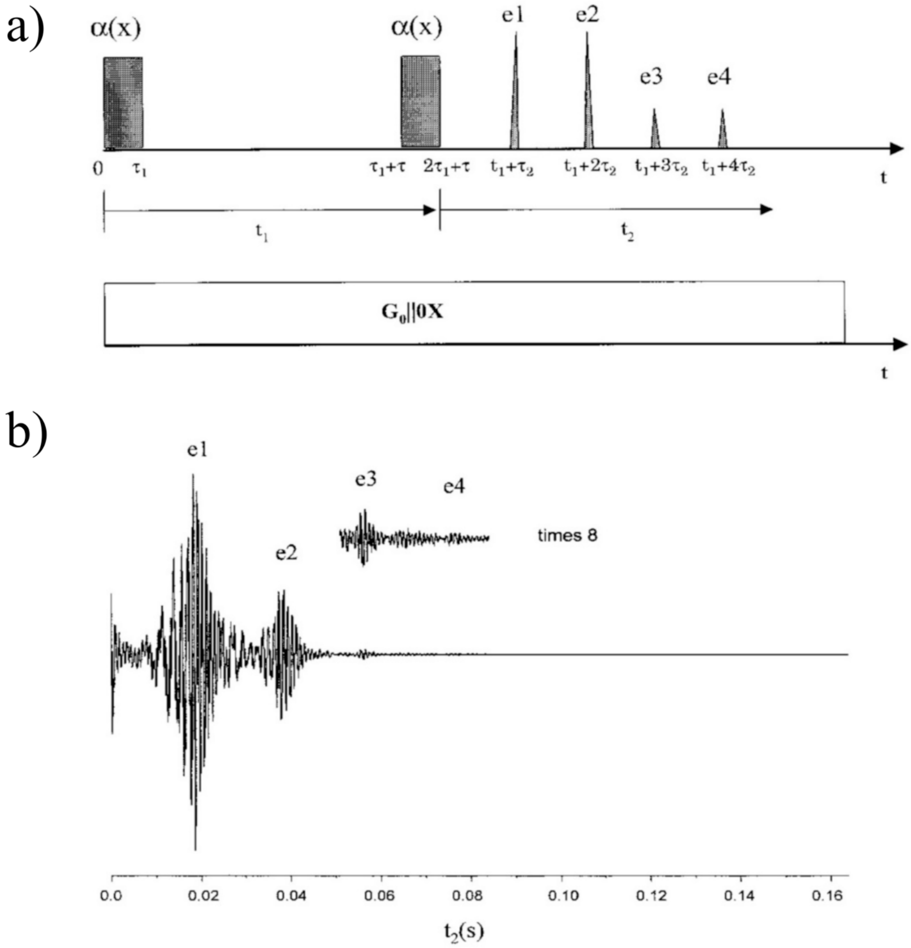

Fig. 4. (a) Radio-frequency pulse sequence used for generation of two-pulse non-linear, multiple rotary echoes. The amplitude of the RF pulses and the static magnetic field are assumed to be subject to gradients G_1 and G_0 ($G_1 \| G_0 \| OX - \mathrm{RF} - \mathrm{coil\,direction}$), respectively. (b) Multiple rotary echoes labeled as e1-e4, were detected in poly(dimethyl siloxane) sample with weight average molecular weight $M_w = 17{,}000$, and $G_1 = 320$ mT/m, $G_0 = 10$ mT/m. The other pulse sequence parameters are given in Ref. [60]. Adapted from [60] with permission.

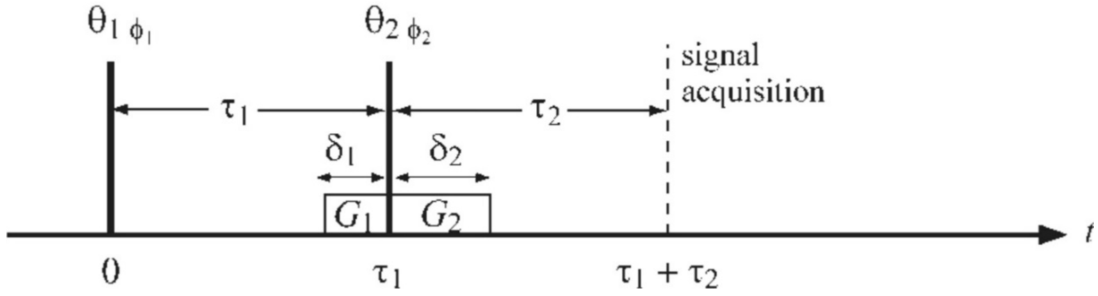

Fig. 5. General scheme of two-dimensional CRAZED pulse sequence [13] using nonselective RF pulses with arbitrary flip angles θ_1 and θ_2, having phases ϕ_1 and ϕ_2, respectively. The pulsed field gradients G_1 and G_2 have duration δ_1 and δ_2, respectively. The gradients area is relevant for the experiment and no importance need be attached to the precise temporal positioning used for coherence transfer selection. The gradient multiple-quantum filter or order n is obtain for $G_2/G_1 = n$ (n is an integer number) and $\delta_1 = \delta_2$. Acquisition is taken in the region of coherence transferred echoes that occurs at $\tau_2 = n\tau_1$, for n = 1, 2, 3,…. Reproduced from [64] with permission.

density operator (see Section 1.3).

3.1. *Spin dynamics for homonuclear CRAZED pulse sequence*

The idea of indirect multiple-quantum spectroscopy dates back to the article of Aue et al. [67]. This pulse sequence was extended to 2D multiple-quantum-filtered COSY by Piantini, Sorensen and Ernst [68] and Shaka et al. [69]. These techniques are based on the scheme shown in Fig. 6 and differences between possible pulse sequences are discussed by Goldman [8]. The spin system response was described using the density operator formalism in the high temperature approximation and the spin dynamics are taking place under intramolecular spin interactions. A novel pulse sequence for obtaining structural and dynamic information in liquids was proposed by Warren and coworkers under the acronym CRAZED [13]. This method is designed in such a way as to excite and detect iMQCs specifically, zero-quantum (ZQ) and double-

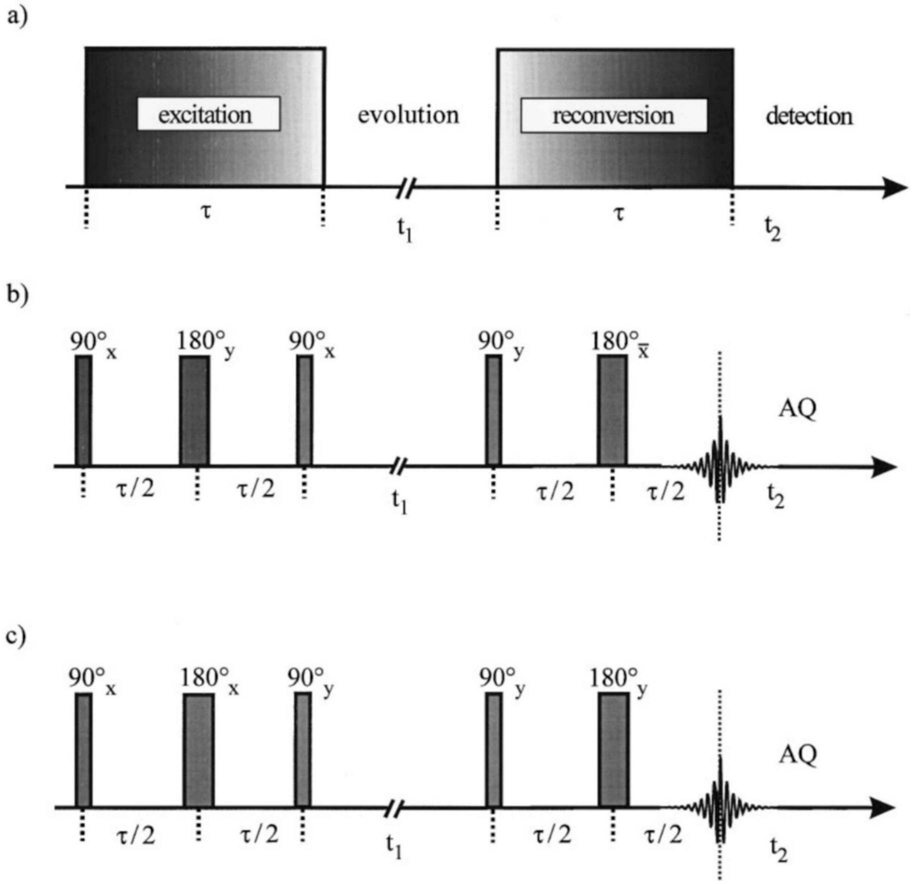

Fig. 6. a) General scheme for excitation, evolution, reconversion, and detection of multiple-quantum (MQ) coherences in 1D and 2D NMR experiments. When the evolution time t_1 is fixed, one-dimensional MQ buildup curves can be measured. b) One-dimensional three-pulse sequence supplemented by 180° refocusing pulses with variable excitation and reconversion times τ, for measuring DQ-filtered coherences in a dipolar network. Adapted from [65] with permission.

quantum (DQ) filtered 2D spectra (Fig. 5). Three new ingredients that are not present in conventional COSY methods (see Ref. [8]) include (i) a general form for the thermal equilibrium density operator (Section 1.3), (ii) the induced long-range dipolar interactions produced by a pulsed gradient filter (Section 1.2), and (iii) coherence echoes produced by spatial averaging. Especially, the last two features of CRAZED edited spectra will lead to new characteristics for MRS and MRI applications. Due to the presence of multiple-quantum coherences the product operator formalism applied to the spin dynamics was the main method used for evaluation of spin system response for the CRAZED pulse sequence [13–15]. However, a classical formalism based on Bloch equations can predict some of the features of CRAZED spectra (see for instance, Ref. [63]).

A simplified discussion of the spin system response in terms of coherences and spin correlations in the CRAZED experiment can be given by the case of two magnetically equivalent spins i and j with $I = 1/2$, without indirect coupling ($J = 0$), [16]. The evolution and detection periods have duration t_1 and t_2, respectively (Fig. 7a). For intermolecular DQ coherences the gradient filter is represented by a pair of pulse gradients with area ratio equal to $A_{G2}/A_{G1} = 2$. The conversion of iMQCs to detected single-spin, single-quantum coherences (iSQC) is produced by the presence of intermolecular dipolar couplings.

The high-temperature term of the density operator cannot contribute to the peaks of the CRAZED sequence, Ref. [16]. The lowest contribution to CRAZED sequence occurs from the quadratic term in the equilibrium density operator, which contains two-spin terms such as $I_{zi}I_{zj}$. The changes in coherence order and spin correlations are shown in Fig. 7a. The first $\pi/2$ pulse transform the $I_{zi}I_{zj}$, product operator into $I_{xi}I_{xj}$, which is a mixture of ZQ and DQ coherences described by products of raising and lowering spin operators $I_i^+I_j^-$ and $I_i^+I_j^+$, respectively Ref. [3]. That means that the first RF pulse can produce multiple-quantum coherences in the presence of nonlinear terms of the thermal equilibrium density operator. Therefore, the excitation period of CRAZED consists of just one pulse. During the evolution period of duration t_1 (see Fig. 7) the spin system evolves under off-resonance effects (Δω) such as chemical shift and the density operator for N spins can be written as, Ref. [16],

$$\sigma\left(t_1^-\right) \propto \sum_{i=1}^{N}\left(I_{xi}\cos(\Delta\omega t_1) + I_{yi}\sin(\Delta\omega t_1)\right) \times \sum_{j=1}^{N}\left(I_{xj}\cos(\Delta\omega t_1) + I_{yj}\sin(\Delta\omega t_1)\right) \tag{22}$$

The modulated ZQ and DQ coherences are described by Eq. (22) and may generate peaks in the t_1 dimension (Fig. 7b).

In an isotropic liquid the long-range dipolar couplings are averaged to zero by molecular diffusion and therefore, are not present in the evolution period. The first pulsed gradient of area GT will break the spin system symmetry and the intermolecular dipolar couplings on the macroscopic scale are introduced into the spin system response. The gradient adds a spatially-dependent evolution frequency of magnitude $\gamma GTs_{i,j}$,where $s_{i,j}$ is the coordinate of the spin i or j along gradient axis. The arguments of trigonometric functions in Eq. (22) will change to $\Delta\omega t_1 \rightarrow \Delta\omega t_1 + \gamma GTs_{i,j}$. The second, nonselective $\pi/2$ pulse applied along the y axis in the rotating frame will produce the transformation $I_x \rightarrow -I_z$ for i and j spin operators. Because no more RF pulses follow (Fig. 7a) only single-quantum coherences must be considered and Eq. (22) becomes as described in Ref. [16],

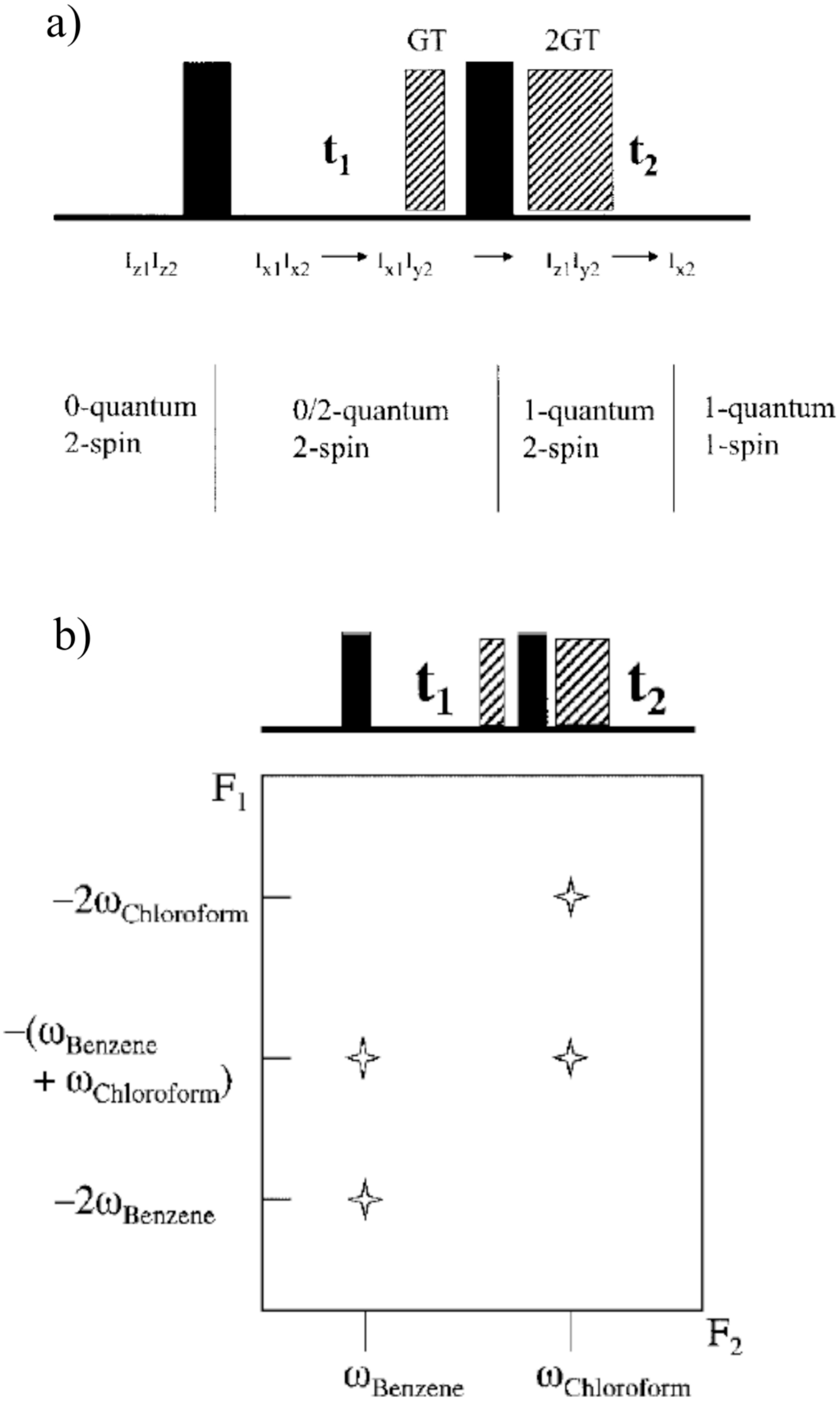

Fig. 7. a) Evolution of relevant spin operators for two spins during homonuclear CRAZED pulse sequence for a spin system without J-couplings. The black blocks represent 90° flip angle pulses and the gradient pulses of areas GT and 2GT are shown by blocks with hatched shading. b) An expected CRAZED spectrum is shown for a mixture of benzene and chloroform. The frequency and phase characteristics of the peaks have the properties of intermolecular DQ coherences. Adapted from Ref. [16] with permission.

$$\sigma(t_1) \propto \sum_{i=1}^{N}\sum_{j=1}^{N}\left[-I_{zi}\cos(\Delta\omega t_1 + \gamma GTs_i) + I_{yj}\sin\left(\Delta\omega t_1 + \gamma GTs_j\right)\right] \tag{23}$$

The second gradient pulse will introduce in the term dependent on I_{yj} a new trigonometric functions with argument $2\gamma GTs_j$. The product of trigonometric functions can generate terms that have arguments dependent on the relative spin positions $\left(s_i - s_j\right)$ and the other terms like $\sin(\gamma GTs_i)$, will be spatially averaged to zero if the gradient winds up a helix with many turns over the sample. After some algebra (see Ref. [16]) the density operator becomes

$$\sigma\left(t_1^+\right)\propto\sum_{i,j=1}^{N}\left[I_{zi}I_{xj}\cos(2\Delta\omega t_1)-I_{zi}I_{yj}\sin(2\Delta\omega t_1)\right]\times\cos\left[\gamma GT\left(s_i-s_j\right)\right]\quad(24)$$

Hence, at the end of the spin system evolution of duration t_1^+, antiphase single-quantum, 2-spin coherences are generated (Fig. 7a). These coherences will evolve during the period t_2 under intermolecular long-range dipolar couplings. The only part of the secular dipolar Hamiltonian that matters here is the longitudinal part that has as a factor the Legendre function Δ_s, [3]. The antiphase product operator evolution for a time t, under this Hamiltonian takes place, for example, as

$$2I_{zi}I_{xj}\xrightarrow{D_{ij}I_{zi}I_{zj}t}2I_{zi}I_{xj}\cos\left(D_{ij}t\right)+I_{yj}\sin\left(D_{ij}t\right)\quad(25)$$

Using the algebra given in Refs. [3,8,9,16] it is possible to write a density operator for single-quantum/single-spin coherences as

$$\sigma(t_1+t_2)\propto\sum_{j=1}^{N}\left[I_{yj}\cos(2\Delta\omega t_1)+I_{xj}\sin\left(I_{yj}\cos(2\Delta\omega t_1)\right]\right.$$
$$\times\sum_{i=1}^{N}\cos\left[\gamma GT\left(s_i-s_j\right)\right]sin\left(D_{ij}t_2\right)\quad(26)$$

The discrete distribution of dipolar couplings can be replaced by a continuous distribution and the summation by an integral. The integral gives the total effect of intermolecular dipolar couplings on a spin at the center of an infinitely large sample. In the limit of the above assumptions the detected signal is given by [16],

$$S(t_1+t_2)\propto\sum_{i=1}^{N}\left[I_{yi}\cos(2\Delta\omega t_1)+I_{xi}\sin\left(I_{yj}\cos(2\Delta\omega t_1)\right]\right.\times\left(-\frac{\Delta_s t_2}{\tau_d}\right)\quad(27)$$

This signal behaves like a SQ transition in the t_2 dimension and like a DQ transition in the t_1 dimension as shown in Fig. 7b. The signal increases during the acquisition time t_2, as shown by similar DQ build-up curves in the experiment using short-range dipolar networks. A complete derivation, as given in Ref. [30], reveals that the SQ detected signal is related to the function $J_2(x)/x$, where J_2 is the second order Bessel function and x is $-\frac{\Delta_s t_2}{\tau_d}$. Furthermore, it is possible to compare the intensities of the crosspeaks obtained by CRAZED and conventional COSY in the limit of the linear term in the Boltzmann factor. Richter and Warren [16] reported the relation

$\frac{S_{CRAZED}}{S_{COSY}}=\frac{1}{4}\,\frac{t_2\Delta_s}{\tau_d}$. (28).

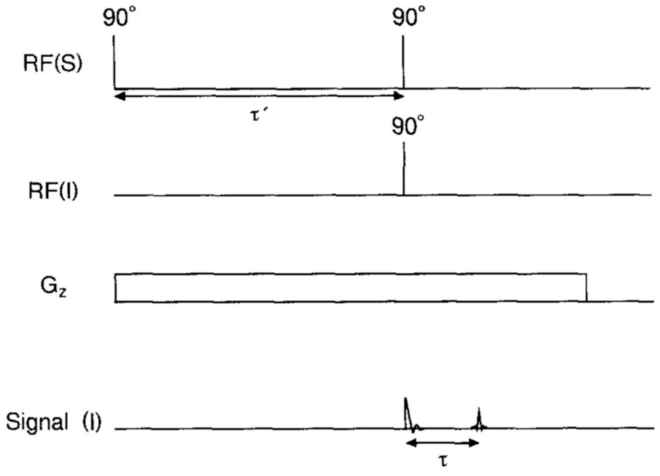

Fig. 8. Radio-frequency (RF) pulse sequence which can be used to produce multiple spin echoes for I spins in the presence of dipolar demagnetization field of S spins. A constant gradient G_z is applied along the direction of static magnetic field B_0. Only one I-spin echo from the possible multiple echoes is shown that occurs at time τ. Reproduced from Ref. [43] with permission.

Due to the behavior of the dipolar demagnetization time τ_d, the ratio S_{CRAZED}/S_{COSY} will increase with the strength of static magnetic field, the concentration of nuclei, and their polarization. A detailed analysis of the evolution of various coherence orders in a CRAZED sequence and optimization of experimental parameters based on phase cycle was previously discussed by Branca et al. [62].

A CRAZED-like sequence called HOMOGENIZED (homogeneity enhancement by intermolecular zero-quantum detection) has been proposed by the Warren group [70,71]. This sequence removes magnetic inhomogeneity while retaining chemical shift differences and J couplings. The HOMOGENIZED sequence is based on the detection of iZQCs between a solute and solvent molecules that are micrometers away. Compared to CRAZED, the HOMOGENIZED pulse sequence is based on the following modifications: (i) for iZQCs detection only one correlation gradient is used; (ii) the second RF pulse has a flip angle of π/4, that achieves maximum detected single-quantum coherence; (iii) at the end of the pulse sequence, a π hard pulse is added to produce a spin echo, in order to reduce the effects of relaxation [70]. This sequence generates images with fundamentally different contrast that comes from variations in the susceptibility over a distance dictated by the gradient strength (see Section 5) [71].

It has been reported that intermolecular double-quantum coherences (iDQCs) possess features similar to those of iZQCs [72,73]. The signal edited by iDQCs can be generated with no additional phase cycling and their intensities are approximately 30 % higher than those from iZQCs [72]. Therefore, a modification of the CRAZED pulse sequence was introduced that can produce high-resolution NMR spectra in inhomogeneous fields, while maintaining quantitative relationships of chemical shifts, J coupling constant, multiplicity patterns, and relative peak areas. This sequence was called IDEAL (intermolecular dipolar-interaction enhanced all lines) [74]. The IDEAL sequence was designed to produce 2D spectra of solvent (I spins) and solute (S spins) of different resonance frequencies and is based on CRAZED having a nonselective first pulse and selective second pulse for the I spins only. A nonselective refocusing π RF pulse is applied at some time interval at the end of the two-pulse sequence and the spin echo is detected in the t_2 dimension of the experiment. Chen et al. [74] discussed the 2D iDQCs spectrum without inhomogeneous broadening and the spectral shearing procedure. The IDEAL sequence ensures that solute–solvent cross-peaks are obtained while solute–solute cross-peaks are effectively suppressed. Several other features of CRAZED-like sequence, such as optimal RF flip pulses and use of intermolecular single-quantum coherences (iSQCs) were reported by Zhonǵs group [75–77].

3.2. Heteronuclear CRAZED-like pulse sequences

A heteronuclear spin echo experiment based on the dipolar demagnetization field was discussed even before the CRAZED experiment was demonstrated by Warren et al. [13]. Indirect detection in a heteronuclear I and S spin system via long–range dipolar couplings in the presence of nonlinear spin echoes was proposed by Bowtell [43]. The dipolar demagnetization field produced by protons was able to enhance ^{13}C detection. This technique does not require that the two spin species I and S having magnetogyric ratios γ_I and γ_S, respectively, be indirectly J-coupled or even on the same molecule and can be applied to 2D NMR spectroscopy using the heteronuclear CRAZED pulse sequence as discussed below. Nonlinear effects were exploited by allowing I spins belonging to one spin species to precess under the influence of the dipolar demagnetization field produced by S spins of a different spin species. The dipolar demagnetization filed generates an echo of the I magnetization that carries information about the state of the S magnetization and so offers a method of indirect detection. A possible pulse sequence than can produce an indirect nonlinear I-spin echo is shown in Fig. 8, [43]. The Bloch equations were used to predict the characteristics of the indirect echoes and it was shown that during the evolution of I-spin complex transverse magnetization $M_I^+(t)$ only the longitudinal

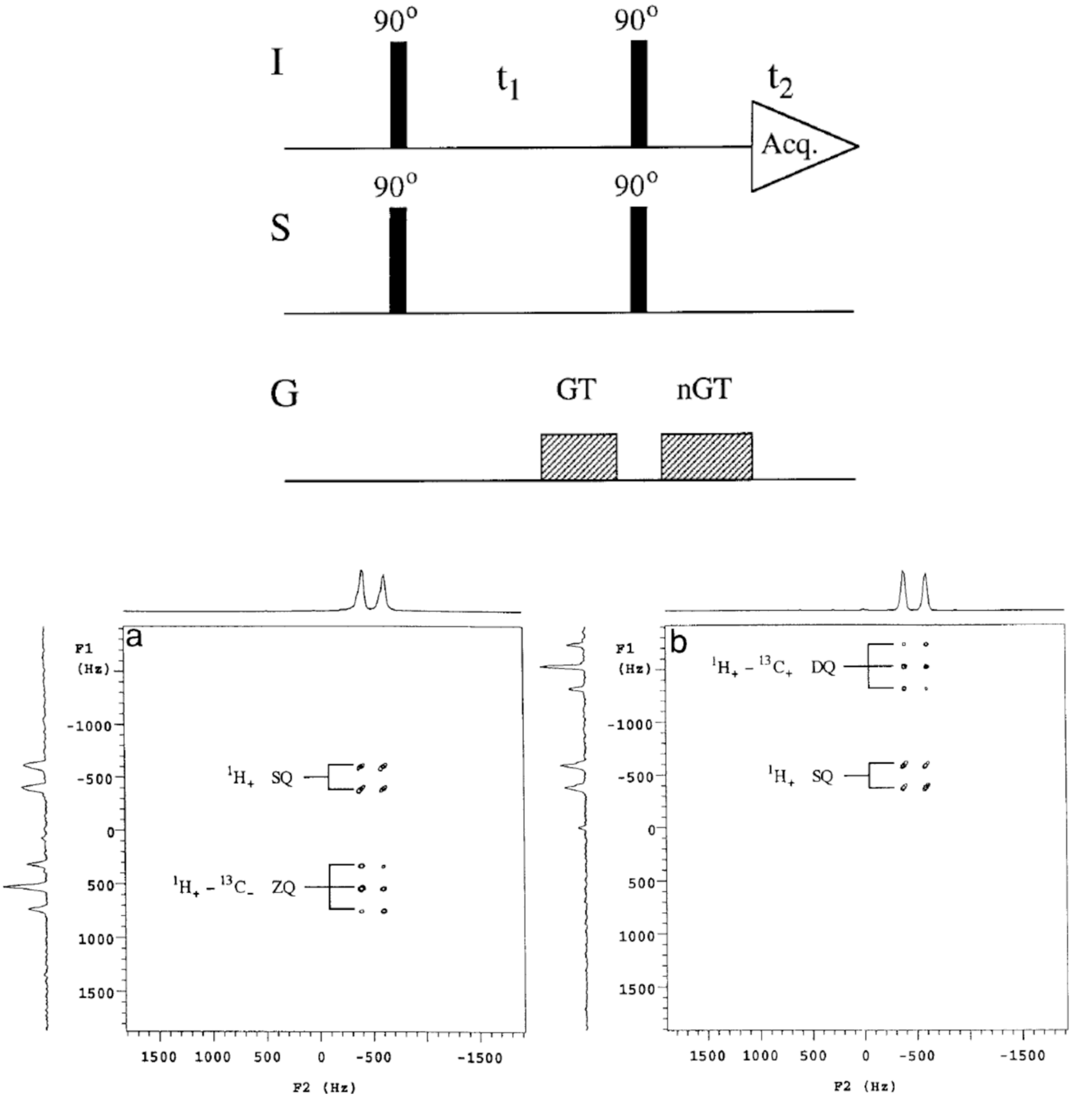

Fig. 9. Top panel: the heteronuclear CRAZED pulse sequence and multiple quantum pulsed gradient filter used to excite and detect heteronuclear multiple quantum coherences in the presence of a dipolar demagnetization field. A portion of the first gradient pulse of strength G and duration T could be applied at the beginning of the t_1 period to prevent radiation damping produced by concentrated I spins. For intermolecular ^{13}C–^{1}H heteronuclear multiple-quantum coherences, a ratio of $\pm 3/4$ selects ZQ terms and a ratio of $\pm 5/4$ selects DQ coherences. The two-steps phase cycling on the first S spin (^{13}C), 90° pulse and receiver phase eliminates the residual I spin (^{1}H) coherences. Bottom panel: 2D spectra of intermolecular heteronuclear ZQ (a) and DQ (b) on carbon-13 enriched chloroform. The peak positions and multiplets are discussed in Ref. [79]. Adapted from Refs. [78–80] with permission.

magnetization of the *S*-spins is spatially modulated and so able to generate echoes. The detected *I*-spin magnetization is given by relation,

$$M_I^+(t) = M_{0I}\sum_{n=-\infty}^{+\infty} J_{|n|}\left(\frac{2}{3}\mu_0\gamma_I M_{0S}t\right)\exp\left\{i\gamma_I G_z\left[\frac{n\tau'\gamma_S}{\gamma_I}\right] - t\right\} \tag{29}$$

where M_{01} and M_{0S} are the equilibrium magnetizations. From Eq. (29) the amplitude of the nth nonlinear echo is proportional to $(\mu_0\gamma_I M_{0S}\tau)^n$ for $\mu_0\gamma_I M_{0S}\tau \ll 1$. The *I* detected nonlinear echoes occur at times $t = n\tau = n\tau'\left(\frac{\gamma_S}{\gamma_I}\right)$, (see Fig. 8). Where longitudinal relaxation times of both spin species can be neglected but where transverse relaxations (T_2) and diffusivity (D) are significant the τ parameter has a value dependent on the field gradient, T_2 and D, [8]. This form of indirect detection involving the dipolar demagnetization field can be applied to a wider class of systems than methods which rely on *J* couplings. However, it also means that indirect detection based on the dipolar demagnetization field does not yield any new information about the system apart from that of spatial correlation of the two spin species.

Heteronuclear nonlinear spin echoes were also investigated with respect to the influence of indirect *J*-coupling in a two-spin ½ system consisting of ^{1}H and ^{13}C [42]. This echo is based on the evolution of the ^{13}C coherence in the presence of the dipolar demagnetization fields originating from the ^{1}H magnetization. The amplitude of the ^{13}C nonlinear echo oscillates as a function of the pitch of the proton magnetization helix. The Fourier transform reveals a doublet with a splitting equal to the intramolecular ^{13}C–^{1}H, *J* coupling constant [41].

Heteronuclear nonlinear spin echoes show strong attenuation by molecular diffusion [42]. The attenuation mechanism by molecular displacement relative to the modulated demagnetization field was demonstrated with the aid of the heteronuclear ^{1}H/^{13}C experiment. The magnetization grid was produced on the proton containing molecules with less translational mobility and ^{13}C coherences were excited in mobile solvent molecules. The pulse sequence employed in this experiment is similar to that shown in Fig. 8, and the first nonlinear ^{13}C spin echo appears after an interval 4 times ($\gamma_I/\gamma_S \approx 4$) larger compared to the time interval of two 90° pulses applied to the ^{1}H system (see Ref. [43]).

A novel form of spatial editing of heteronuclear NMR spectra, restricting signals to those from heteronuclei spatially coincident with high proton concentration was suggested by Morris and coworkers [44]. The pulse sequence empoyed is that shown in Fig. 9 and the spin system is represented by I=^{1}H (H_2O) and S=^{31}P in $Na_2H^{31}PO_4$ water solution.

Warren and coworkers reported the first 2D experiments confirming that intermolecular heteronuclear coherences in solutions can also be detected, using a variation of the homonuclear CRAZED experiment [78]. The HETERO-CRAZED pulse sequence is shown in Fig. 9 (top panel) and was also used in similar experiments [79–81]. The general reduced density operator for I (for instance ^{1}H) and S (for instance ^{13}C) spin systems is given by

$$\sigma_{eq} \propto \sum_i \left(1 - \Im_I I_{zi}\right) \sum_j \left(1 - \Im_S S_{zj}\right) \tag{30}$$

where $\Im_{I,S} = 2\tanh\left(\frac{\hbar\omega_{i,j}}{k_B T}\right)$. The hard I and S pulses of tip angle 90° rotates the z spin operators into x operators and will generate after one pulse homonuclear and heteronuclear multiple quantum coherences. During the t_1-evolution period heteronuclear terms of the form $I_{\pm}S_{\pm}$ will evolve at frequencies corresponding to heteronuclear multiple-quantum (HeMQ) coherences. In order to observe these coherences during the t_2 dimension two conditions have to be fulfilled: (i) HeMQs should be transferred into single-quantum coherences by the second pair of 90° pulses and (ii) the spatial average of the terms evolving at the multiple-quantum frequencies must be nonzero. The gradient pulses filter affects their spatially modulated averages. The second pair of 90° pulse transfers these coherences onto terms such as antiphase coherences $I_{\pm}S_z$. These coherences are rendered observable by the very large number of small intermolecular heteronuclear dipolar couplings that create single-quantum $I_{\pm}$ for detection. Detectable coherences remaining after the gradient filter require the amount of refocusing during the second gradient pulse, $\gamma_I nGT$, to be the same as during the first gradient. This leads a condition for the gradient ratio of $n = \pm\left(1 \pm \frac{\gamma_S}{\gamma_I}\right)$. When the I (^{1}H) spins are detected and S=^{13}C we have $= \pm\frac{3}{4}$, or $n = \pm\frac{5}{4}$. For the first ratio $= \pm\frac{3}{4}$, the heteronuclear ZQ coherences, such as I_+S_- is detected, which correspond to a t_1 frequency in the rotating frame of $\Delta\omega_I - \Delta\omega_S$. For $n = \pm\frac{5}{4}$, the DQ coherences, such as I_+S_+, are detected, whose t_1 frequencies are $\Delta\omega_I + \Delta\omega_S$. An example of heteronuclear multiple quantum coherences 2D spectrum in ^{13}C-enriched chloroform with detection of protons for ZQ and DQ coherences are shown in Fig. 9 (bottom spectra) [79].

Heteronuclear intermolecular multiple-quantum coherences in solutions, while weaker than proton multiple-quantum coherences due to smaller I-S dipolar couplings, were readily observed in concentrated solution for nuclear spins with smaller magnetogyric ratios like ^{13}C. Nevertheless, the ability to use the demagnetization field to indirectly detect the evolution of low-γ nuclei via protons may eventually prove useful in a variety of applications. Furthermore, the quantum and classical approaches give, in principle the same interpretation of heteronuclear intermolecular multiple quantum experiments as described in Refs. [79–81].The Bloch equations approach may have some computational advantages, but it only works in the absence of J-couplings. In the classical approach diffusion and radiation damping can be easily included. However, the density operator approach in combination with product operator formalism gives an intuitive picture of pulse sequence physics and is able to predict the effects of new pulse sequences based on the strong foundation of quantum mechanics.

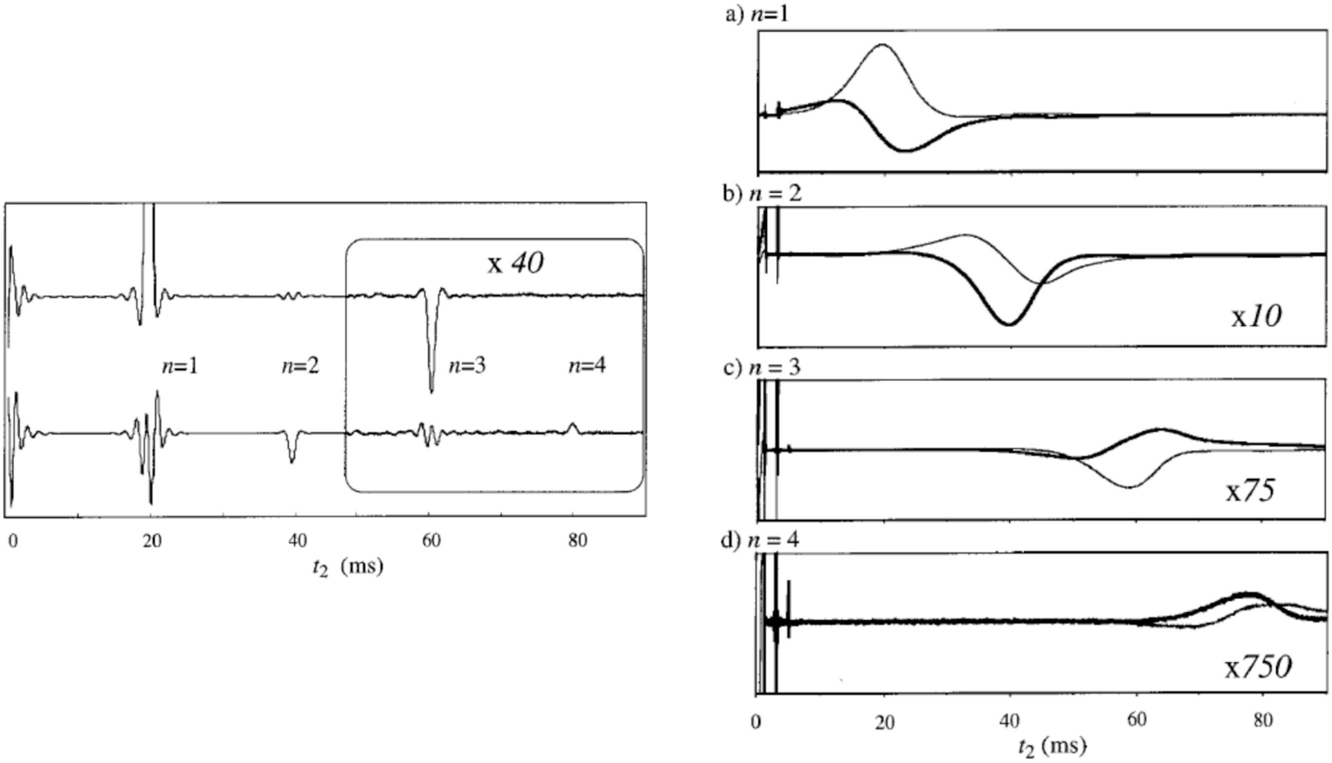

Fig. 10. Left-hand panel: time domain nonlinear spin echoes obtained for the pulse sequence of Fig. 5 using a steady gradient (G = 4x10^{-3} T/m) oriented in the z direction for $\phi_1 = \phi_2 = x$, and τ_1 = 20 ms. The nonlinear spin echoes of order n = 3 and n = 4 are shown magnified 40 times. A polydimethylsiloxane (5000 Da) sample with low values of diffusivity was used for the experiments. The upper and lower lines correspond to the imaginary and real signals, respectively. Right-hand panel: intermolecular coherence transferred echoes from the CRAZED sequence of Fig. 5. Real and imaginary signals are represented by thick and thin lines, respectively. Magnification relative to a) is shown in b) through d). Adapted from Ref. [17] with permission.

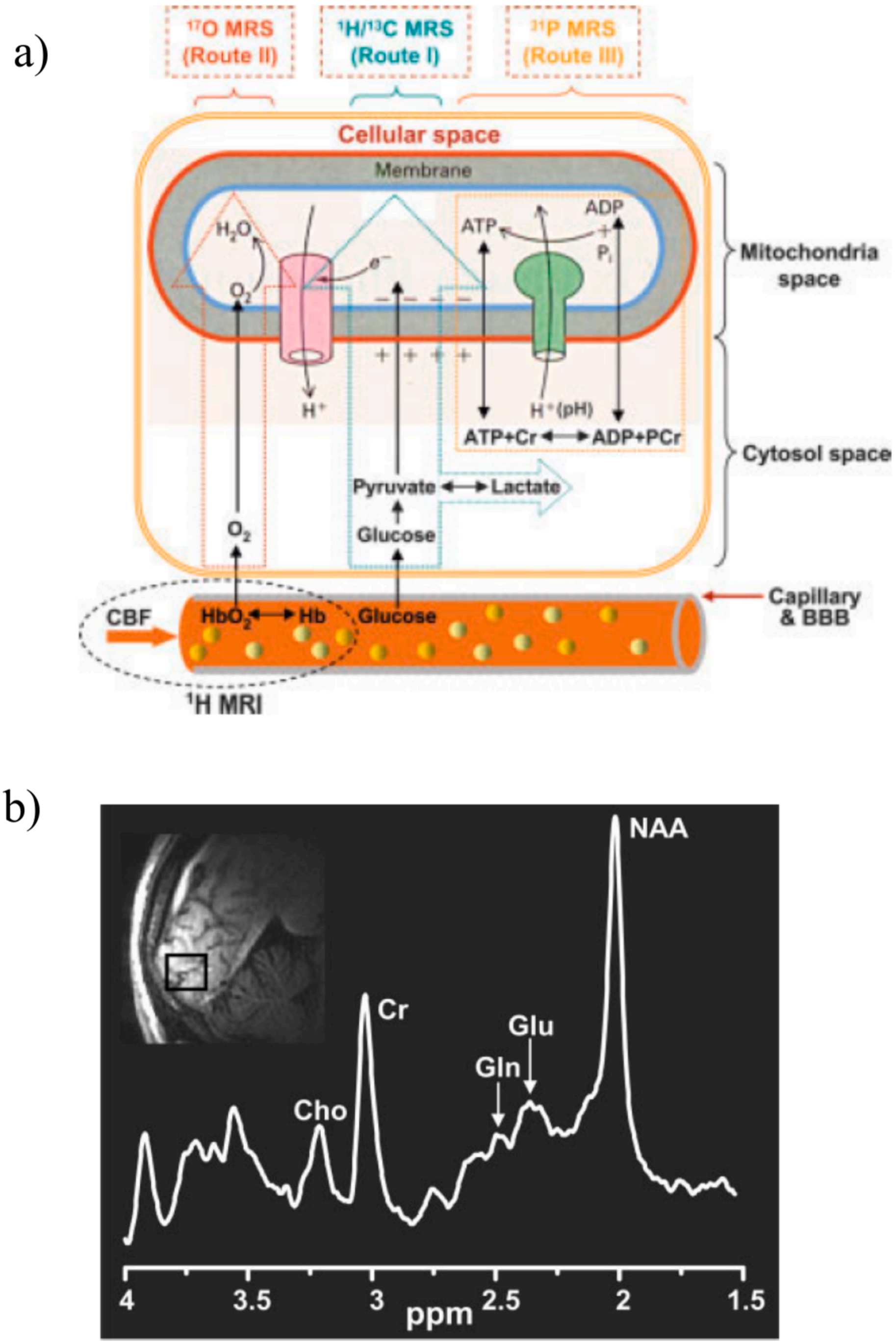

Fig. 11. A) schematic diagram for metabolic and hemodynamic processes occurring in brain. route i, ii, and iii correspond to glucose metabolism, cerebral oxygen use, and^{31}P MRS is useful for studying high-energy phosphate metabolism, respectively. b) Localized in vivo ^{1}H MRS in the human primary visual cortex. Detected metabolites are N-acetyl aspartate (NAA), glutamate (Glu), glutamine (Gln), creatine (Cr) and choline. Adapted from [85] with permission.

3.3. The correspondence between the order of time domain nonlinear spin echoes and that of intermolecular multiple-quantum coherences in CRAZED experiments

The correspondence between intermolecular multiple quantum coherences edited by coherence transferred echoes of n^{th} order in the CRAZED sequence and multiple spin echoes of the same order n was shown to exist in Ref. [17]. This was proved by comparing the signals shown in Fig. 10. In the experiments for nonlinear spin echoes, a continuous gradient is applied and we can compare the gradient areas in the t_1 domain to gradient area in the t_2 domain. For instance, for $t_2 = 4t_1$ the 4th multiple spin echo is equivalent to the 4th coherence transferred echo of the CRAZED experiment (Fig. 10).

The similarity of the physics behind multiple spin echoes and coherence transferred echoes can be also seen from the experiments using a gradient oriented at the magic angle ($\theta_m = 52.7^\circ$) relative to the direction of the main magnetic field $\boldsymbol{B}_0$, [17]. The long-range dipolar field is reduced to zero due to the Legendre polynomial angular dependence. All remaining demagnetization field effects must arise from the sample shape alone. Bowtell et al. reported a significant reduction of the intensity of the high-order nonlinear echoes [12] in agreement with the CRAZED sequence [14,15].

4. Global and spatially localized magnetic resonance spectroscopy (MRS) by iMQCs

Conventional ^{1}H magnetic resonance spectroscopy (MRS) alone or in combination with magnetic resonance imaging (MRI) has become well established as a non-invasive method for studies of biological systems including the brain. This is due to its relatively high sensitivity and ability to detect tissues metabolites, chemical reaction rates, bioenergetics and their dynamic changes in response to brain activities in humans (Fig. 11a) [82–87]. Chemical shift and *J*-indirect couplings were measured and thorough resonance assignments were given for in vivo and in vitro mammalian brain, as shown in the example given in Fig. 11b [82–88]. The availability of metabolite spectral parameters makes it possible to generate model functions for parametric spectral analysis of ^{1}H MRS of brain, as has previously been demonstrated for in vivo proton spectroscopic imaging [89]. Besides, proton MRS the most metabolically relevant nuclei detected by in vivo MRS include ^{13}C, ^{17}O and ^{31}P as were reviewed in Ref. [85]. Volume localized MRS delivered by MRI techniques enabled the detection of metabolites in living organisms at low concentration below 1 mM in the human brain with high spatial specificity [90].

In conventional magnetic resonance spectroscopy as well as in MRI and localized MRS the resolution due to inhomogeneous line broadening is an important issue. A substantial reduction of inhomogeneous line broadening can be achieved along the indirect dimension in 2D NMR experiments, which are designed to use relative frequency differences between nearby spins to create frequency dispersion [3,5,90]. An example of such an experiment employed intramolecular multiple-quantum coherences of J-coupled spins under total spin coherence transfer echo spectroscopy (TSCTES) [5,91]. In this case the active spin system is limited to the isolated molecules. This method was also applied in vivo to obtain resolution-enhanced spectra from the rat brain [70].

The iMQCs spectroscopy methods derive from the prototype pulse sequence CRAZED for the independent detection of different orders of iMQCs. Resolution enhancement in 2D iMQCs spectra was first demonstrated which selects iZQs and was termed HOMOGENIZED (homogeneity enhancement by intermolecular zero-quantum detection) [70]. Further modifications of this pulse sequence to select distinct coherence pathways more efficiently and enlarge the sphere of applications, have been proposed in literature [74,76,92–98].

In the following we will review the principles and especially in vivo applications of proton iMQCs spectroscopy based on long-range dipolar interactions that can provide spectra without inhomogeneous broadening.

4.1. *Global ^{1}H multidimensional NMR spectroscopy using iSQCs and iDQCs*

Information about structure and dynamics of complex material and biological objects can be obtained by homonuclear or heteronuclear multidimensional NMR spectroscopy [3,5,90,91]. These methods can retain all desired spectral features such as chemical shift, *J* scalar couplings, multiplet patterns, and spin concentration for each molecular species. Two dimensional (2D) *J*-resolved spectroscopy is one of the first multidimensional techniques developed to allow separation of chemical shift and *J* coupling information along two spectroscopic axes. The ability of this method can be enhanced by intramolecular multiple-quantum (MQ) *J*-resolved spectroscopy (MQ-JRES) to measure relative *J*-coupling constants [99,100]. The remote J couplings can be determined by DQ and TQ *J*-resolved spectra [101,102]. A single-scan ultrafast technique can be utilized to allow acquisition of a 2D-*J* resolved spectrum [103].

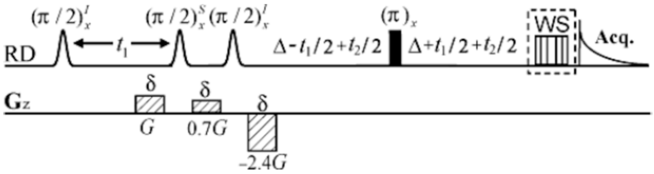

Fig. 12. The iSQCs-JRES pulse sequence in inhomogeneous fields by a 3D acquisition [108]. Gaussian radio-frequency pulses are selective RF pulses. Coherence-selected gradients are represented by dashed rectangles. Solvent (water) suppression pulse sequence is represented by WS module. Reproduced from Ref. [108] with permission.

Moreover, there are many circumstances in which the magnetic field inhomogeneity leads to overleap of peaks as in the case of variations of magnetic susceptibilities among various tissues. Intermolecular multiple-quantum coherences (iMQCs) caused by long-range dipolar interactions among spins in different molecules can be utilized to achieve multidimensional high-resolution spectra in inhomogeneous fields based on a 2D acquisition [71,75,104–108]. Since the direct acquisition results from conventional single-quantum coherences suffers from spectral inhomogeneous broadening, another dimension must be used to produce a high-resolution spectrum. Hence, for a 2D *J*-resolved spectrum in an inhomogeneous field, a 3D acquisition is required as in the case of the iSQC-JRES method [108]. The fundamental requirement of the iSQC-JRES approach is the presence of a distant dipolar field produced by solvent molecules with a highly concentrated proton density. This is the case for many biological objects like brain.

The spin system response during the action of the pulse sequence shown in Fig. 12 was discussed in Ref. [108] using the formalism of the distant dipolar field. The first and third RF pulses are solvent selective (I isolated ½ − spins), while the second RF pulse excites only solute molecules (S, ½ − spins). These molecules are represented by an AX system, with S_k and S_l spins-1/2 coupled by *J* interaction with a scalar coupling constant J_{kl}. To select the coherence transfer pathway 0→ +1→ +2→ +1→ −1 three linear gradients with an area ratio 1:0.7:-2.4 were applied (Fig. 12). Compared to the direct detection period t_3, both the indirect-detection t_1 where iSQC evolves and spin-echo evolution period of t_2 are insensitive to magnetic field inhomogeneity. The distant dipolar field has an equal effect on all solute spins and does not interfere with the *J* coupling. After spatial averaging along *z* direction and considering.

the 3D spectrum projected onto F1-F2 plane for the signal from the S_k and S_l spins, it is possible to write [108],

$$M_{S_k}^{+} \propto exp\{i[(\omega_{Sk} - \omega_I)t_1 + \pi J_{kl}t_2]\}exp\{i2\pi J_{kl}\Delta\} + exp\{i[(\omega_{Sk} - \omega_I)t_1 - \pi J_{kl}t_2]\}exp\{-i2\pi J_{kl}\Delta\} \tag{31}$$

The above equation provides a description for the 2D NMR projection spectrum in the iSQC-JRES method. The peaks in the 2D spectrum are located at the frequencies [ω_{Sk}-ω_I; πJ_{kl}] and [ω_{Sk}-ω_I; $-\pi J_{kl}$] respectively, due to J coupling.

The performances of the iSQC-*J*RES pulse sequence is shown in Fig. 13 for the case of in vitro pig brain [108]. Almost no spectral information can be obtained from the conventional 1D spectrum (Fig. 13 A) due to line broadening caused by magnetic susceptibility and the intense water signal. The use of the 3D iSQC-JRES approach combined with water suppression (Fig. 12) allows detection of a ^{1}H high-resolution spectrum of metabolites with J-coupling information for lactate (Lac, 1.3 ppm), alanine (Ala, 1.47 ppm), and glutamine (Glx, 3.75 ppm). Better acquisition efficiency of the iSQC-JRES pulse sequence important for in vivo applications may be achieved by combining the method with strategies such as the ultra-fast single-scan NMR technique [103], that can overcome the long duration of the 3D acquisition.

Quantitative analysis of the NMR spectra from iSQCs was discussed based on a combination of the dipolar field treatment and the Torrey equations [77]. In this investigation a technique based on selective excitation was used to suppress the strong conventional SQC signals.

It was also shown that the signals from iSQCs possess properties

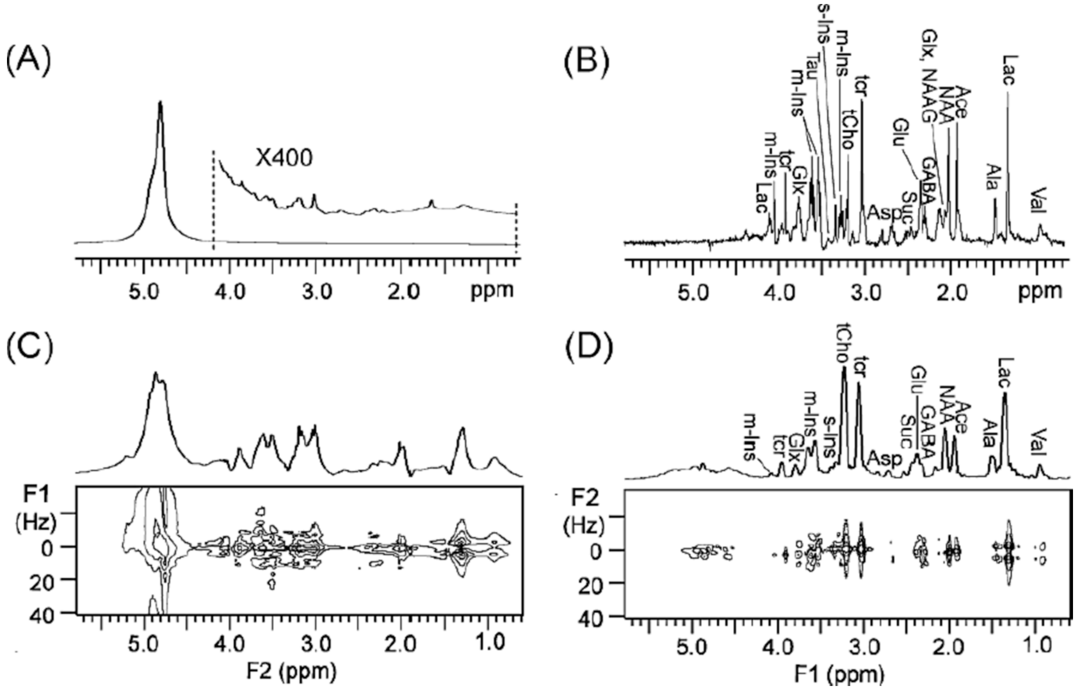

Fig. 13. Proton 1D and 2D SQCs spectra of in vitro pig brain tissue. (A) Conventional 1D SQCs spectrum and the expanded region for metabolites. (B) One-dimensional water presaturated spectrum MAS spin-echo spectrum acquired with the PFG indirect detection method. (C) Conventional 2D water-presaturated J-resolved spectrum, and (D) The projection of ^{1}H spectrum using iSQC-JRES approach and along F1 axis. Reproduced from Ref. [108] with permission.

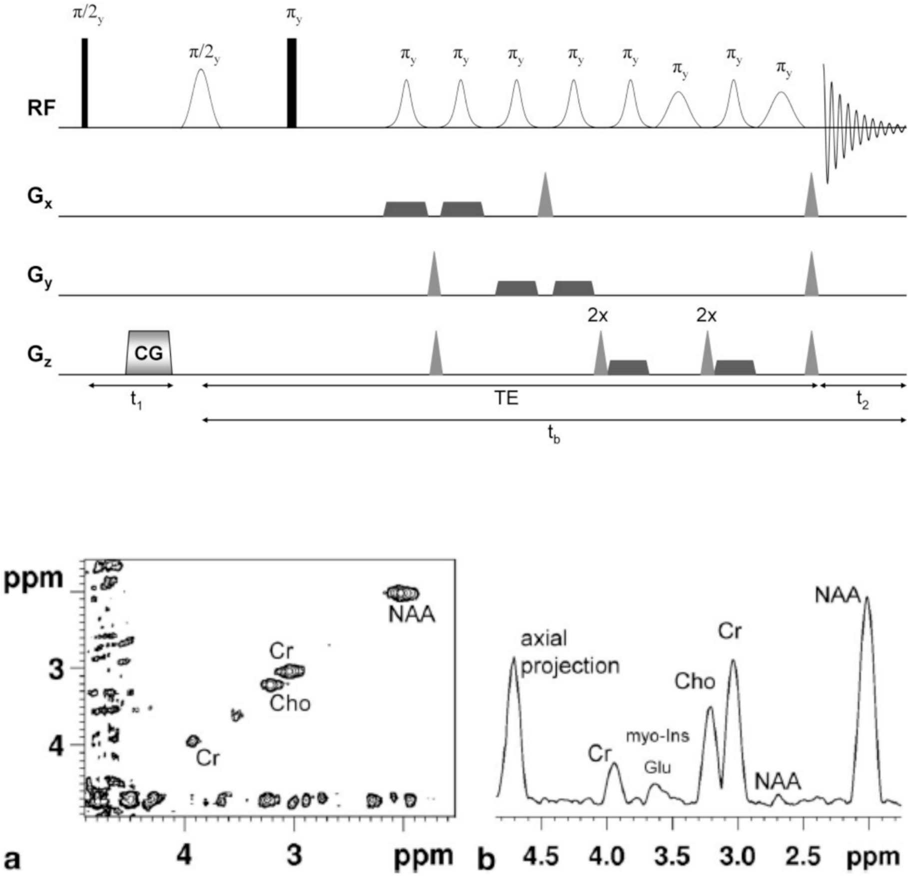

Fig. 14. Top panel: spatially localized HOMOGENIZED pulse sequence with localization immediately prior to acquisition. The hard (black bars) $(\pi/2)_y$ pulse and selective Gaussian pulse $(\pi/2)_y$ are specific for iZQCs selection. A spin echo is generated after the action of a nonselective π_y pulse. The trapezoids are slice-selection gradients and spoiler gradients are represented by gray triangles. Correlation gradient is represented by notation CG. Bottom panel: a) 2D HOMOGENIZED spectrum from a voxel in a rat brain. b) Indirect dimension projection of the ^{1}H 2D spectrum shown in a), for the specified spectral region. Adapted from [96] with permission.

similar to iZQCs and iDQCs providing spatial information related to dipolar correlation scales.

Several pulse sequences based on iMQCs with coherence order different from single-quantum ($m = \pm 1$) evolution using 2D acquisitions have been designed to obtain high-resolution NMR spectra [71,104–108]. Chen et al. proposed a series of intermolecular dipolar-interaction enhanced all lines (IDEAL) sequences which employ iDQCs or iSQCs to obtain global 2D high-resolution spectra [106–109]. A pulse sequence that simultaneously detects both iZQCs and iDQCs filtered spectra with enhanced resolution in inhomogeneous fields was introduced in Ref. [109]. In comparison with separate approaches this method can provide nearly doubled spectral resolution and suppression of strong coupling artifacts.

4.2. Spatially localized MRS using iZQCs and iSQCs for brain

In vivo resolution enhancement for 2D NMR spectra, acquired in presence of magnetic field inhomogeneity was proved to be possible using the HOMOGENIZED pulse sequence for detecting iZQC (see Section 3 and Fig. 14.), as was proposed in Ref. [71] and improved in Refs. [96–98]. Removal of inhomogeneous line broadening can be achieved along the indirect dimension in 2D experiments, which are designed to use relative frequency differences between nearby spins to create frequency dispersion in the presence of long-range dipolar fields. The principle of resolution enhancement in iZQC filtered spectra was discussed in Ref. [97] and the effect is related to the presence of long-range dipolar fields that limit the distortion of the main magnetic field. The signal that is detected in iZQC-MRS results from refocusing in the presence of the long-range dipolar fields. This refocusing is a local process and therefore, it is insensitive towards spatial or temporal variations of the magnetic field on a scale large compared to the experimentally imposed gradient modulation. However, the HOMOGENIZED pulse sequence for detecting iZQC is not capable of reducing spectral line broadening from nanoscale inhomogeneities.

For successful application of the HOMOGENIZED pulse sequence for in vivo MRS, the long-range dipolar field has to be localized in the detection volume of the iZQC filtered signal and residual water signal must be suppressed efficiently. Spatial localization of the iZQC can be made by two different strategies. In the first, the localization is made in the evolution interval which implies localization of both transverse and longitudinal magnetization making up the long-range dipolar field. The problem with this approach is that the dephasing magnetization prior to the second pulse due to the effect of the distant dipolar fields is nonselective. Therefore, transverse magnetization from all of the sample is subject to refocusing during the detection period and clean spatial localization is not achieved. An efficient means to achieve a spatially localized NMR signal from a HOMOGENIZED experiment is to refocus the signal after the second RF pulse, i.e. prior to acquisition, in a spatially selective manner. Slice refocusing modules after the iZQC selection have no effect on the long-range dipolar field. The volume selection of the pulse sequence shown in Fig. 14 – top panel, uses the localization by the adiabatic selective refocusing (LASER) sequence with six adiabatic inversion pulses to selectively refocus the magnetization of three orthogonal slices [110]. Two additional frequency-selective refocusing pulses (π_y) were inserted during slice selection along the z-axis, forming a water suppression module.

Proton 2D and projection spectra of the rat brain that resolve three major metabolites, i.e., creatine (Cr), choline (Cho), N-acetyl aspartate (NAA) are shown in Fig. 14a and b, on bottom panel, respectively, [96]. Such 2D spectra can be acquired in a few minutes using the HOMOGENIZED pulse sequence. The indirect dimension projection (f_1) shows peaks well resolved proving that high-quality spectra can be obtained with iZQC techniques. The spectral quality is not influenced by the large voxel size or the intrinsic inhomogeneity. The spectral linewidth scales with the number of t_1 increments.

For in vivo experiments to avoid artifacts from long term movements, an accelerated version of HOMOGENIZED pulse sequence has been proposed [94]. A limitation of this technique is that sensitivity has to be traded off for the speed. Furthermore, in warm blooded animals, under in vivo conditions faster transverse magnetization relaxation leads to severe signal losses that limit the signal-to-noise of detected signal [99]. In some cases the use of larger voxels provide a solution to the above problem, compensating for the inherent low sensitivity of the iMQCs techniques.

The salient features of the HOMOGENIZED spin system response for two inequivalent spins I and S, was discussed in Refs. [76,97], taking into account the long-range dipolar field of both species. For large chemical shift differences compared to the long-range dipolar field the signal evolution can be derived from the Bloch equations including distant dipolar fields. If the second RF pulse is frequency selective on I spins, then all S spins remain with transverse magnetization and maximum long-range dipolar field is produced from the I spins. The detected S spins transverse magnetization in this 2D MRS experiment is given by

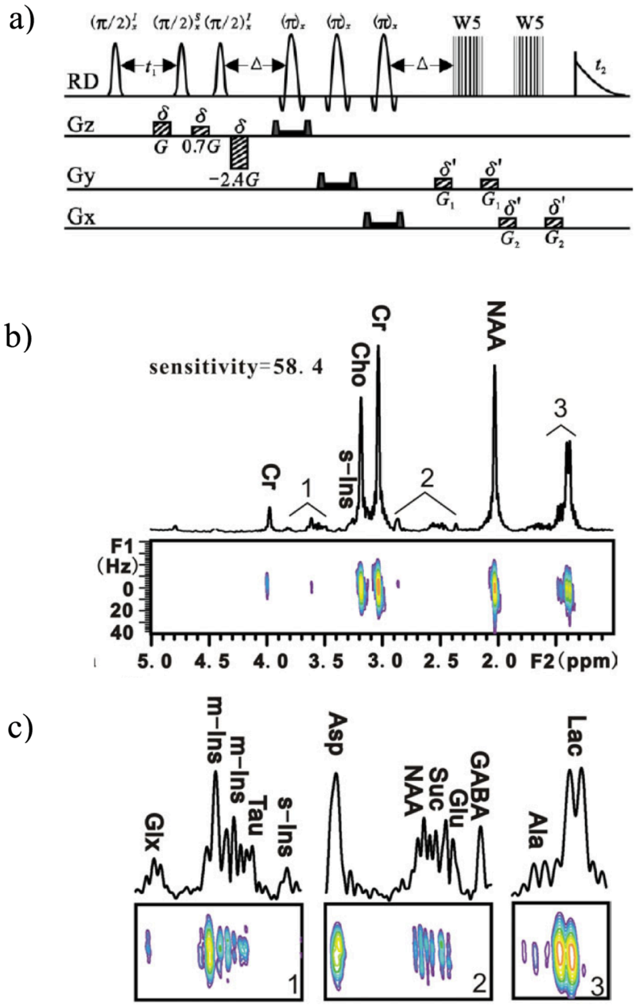

Fig. 15. A) volume localized isqcs pulse sequence for 2d mrs with a press localized module and a water suppression double gradient echo w5 binomial π pulses. The gradient pulses used for coherence selection, slice selection by PRESS approach, and water suppression are marked, along different directions. b) Localized iSQCs 2D spectrum of brain phantom in aqueous solution. c) The spectral expansion of the regions labeled 1, 2, and 3 in (b). The metabolite resonances are assigned in Ref. [116]. Adapted from [116] with permission.

$$M_x(t_2) + iM_y(t_2) = iM_0^S exp\{i\Delta\omega_S t_2\} exp\{i(\Delta\omega_S - \Delta\omega_I)t_1\} J_1\left(-\frac{\frac{2}{3}t_2}{\tau_{dI}}\right) \tag{32}$$

where J_1 is the first order Bessel function. Moreover, relaxation and diffusion were neglected and the symbols are defined in Section 3. If the T_2 and T_1 relaxations of both nuclei are taken into account the above equation can be written as given in Refs. [76,97],

$$M_x(t_2) + iM_y(t_2) = iM_0^S exp\{i\Delta\omega_S t_2\} exp\{i(\Delta\omega_S - \Delta\omega_I)t_1\} exp\{-(t_1+t_2)/T_2^S\} \times J_1\left(-\frac{\frac{2}{3}T_1 \exp\left(-\frac{t_1}{T_2^I}\right)\left(1-\exp\left(-\frac{t_2}{T_1^I}\right)\right)}{\tau_{dI}}\right) \tag{33}$$

The theoretical signal evaluation of a singlet brain metabolite resonance based on Eq. (33) reveals that for shorter T_2 of the detected spin species (i.e., T_2^S) only about 10 % of the equilibrium magnetization will be detectable with the HOMOGENIZED pulse sequence [99]. Moreover, experiments and numerical simulations have suggested that under in vivo conditions the effect of molecular diffusion is small as is expected for the HOMOGENIZED pulse sequence [111–114]. The HOMOGENIZED pulse sequence applied to in vivo experiments provides enhanced spectral resolution, or alternatively in large inhomogeneous voxels higher signal-to-noise efficiency than conventional techniques. It has been mentioned that MRS based on iZQCs is unlikely to provide advantages over conventional localized spectroscopy in the brain using localized shimming procedures [97].

The possibility of using volume localized iSQCs for obtaining in vivo and in vitro ^{1}H 2D high-resolution NMR spectra in inhomogeneous fields in brain tissues was discussed in Refs. [115,116]. This pulse sequence can recover information on chemical shift, *J*-coupling constants, relative peak areas, and multiplet patterns even when spectral information is erased by the field inhomogeneity. Localized iSQCs MRS is efficient for relatively large voxels. Moreover, good solvent suppression can be achieved by this sequence even with imperfect pulse flip angles. Compared with iZQCs methods discussed above iSQCs MRS provides a narrow spectral width in the indirect dimension. Like iZQCs and iDQCs [116–118] methods, the enhancement of spectral resolution is at the cost of signal-to-noise ratio.

Using conventional point-resolved spectroscopy (PRESS) as the volume localization approach [119] and the pulse sequence shown in Fig. 15a, the 2D ^{1}H high-resolution spectrum filtered by iSQCs was obtained from a brain phantom (Fig. 15b and c) [116]. These spectra show a well suppressed solvent signal. Metabolites were assigned according to Refs. [83] and [116]. The linewidth of the projected spectrum is reduced by one order of magnitude and even the doublet splitting of the lactate spectrum (Lac. 1.31 ppm) is retained (Fig. 15b and c).

5. Magnetic resonance imaging (MRI) by intermolecular multiple spin echoes and iMQCs

5.1. Structural investigation by intermolecular multiple spin echoes

Warren and coworkers proposed that through manipulation of the distant dipolar field (DDF), it may be possible to extract structural information using intermolecular multiple-quantum coherences [120]. As a first step in this direction, in a series of papers Bowtell and Robyr established a Fourier-space relationship between the structure of heterogenous objects and the amplitudes of multiple spin echoes (MSEs) which arise in solution NMR as a result of the long-range dipolar field [121–123]. When a sequence of two radio-frequency pulses is applied at the time interval of TE/2 on a liquid sample, it will produce a single spin echo at time TE. In the presence of long-range dipolar fields MSEs occurs at multiples of TE/2 (see Section 2). On this basis, theoretical models for

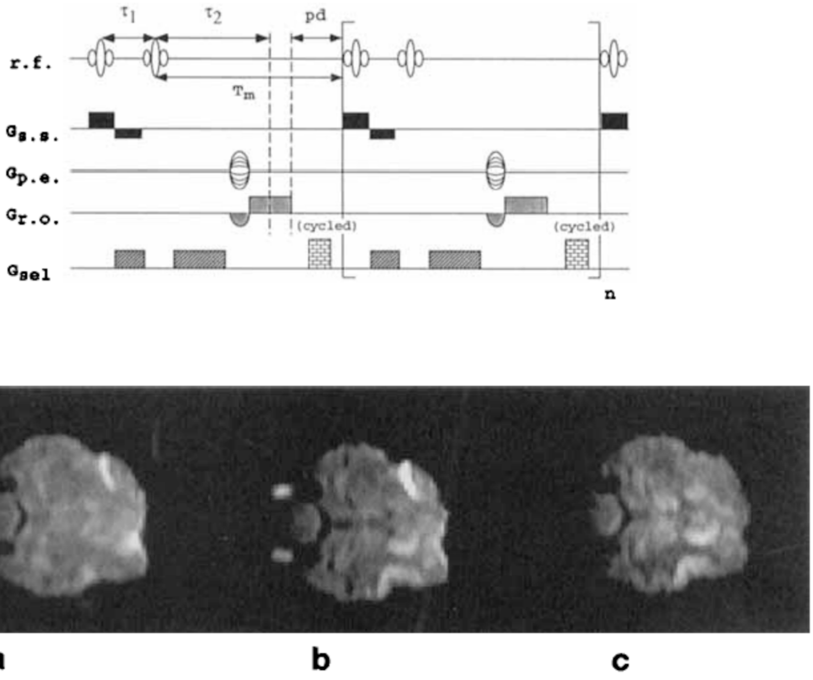

Fig. 16. Top panel: Pulse sequences used for producing images based on shifted stimulated echoes (SSTEs) and multiple spin echoes (MSE). Coherence selection pulsed gradients are denoted by G_{sel}. The other gradients are used for slice selection, phase encoding, and readout. During the interscan delay a crusher gradient is used to avoid interscan gradient-recalled echoes. Bottom panel: Axial images of the basal ganglia of cat brain. a) Reference spin-echo image. b) Diffusion weighted image using a spin-echo/pulsed gradient pulse sequence. c) SSTE image of a cat brain in which middle cerebral artery is occluded. The experimental parameters are given in [127]. Adapted from [127] with permission.

periodic structures have been derived and used to analyze the variation of the NMR signal generated by the distant dipolar field [123]. If the spatial modulations imposed on the transverse and longitudinal magnetization have the same wavelength, the signal generated by the dipolar field is a continuous function of the modulation wavelength and is sensitive to the sample structure. When this condition does not occur, diffraction phenomenon may be possible in a periodic structure [123]. The theoretical framework of the classical Bloch equations was applied to describe model NMR experiments and demonstrated the potential use of NMR methods based on long-range dipolar fields in structural investigations at length scales that are difficult to be probe with conventional NMR imaging methods. In the limit where the distant dipolar fields weakly perturb the evolution of the magnetization and where molecular motions is not significantly restricted by the structure, the autocorrelation function, or Patterson function, of the spin density can be obtained [122]. Compared to other NMR methods that can yield Patterson functions [124] this technique takes advantage of the whole sample by applying field gradients along one of several directions. However, one must mention, that the signal generated in the presence of the long-range dipolar interaction is about one order of magnitude less that that obtained from direct measurements on the whole sample. Moreover, it was shown that in the case of a two-spin system, the NMR signal measured in average structure measurement is related to the spatial cross-correlation function of the spin densities of the two components [125]. In the case of cylindrically symmetrical systems this spatial cross-correlation function is related to the Meijer transform [125]. This work also discussed the effect of modulating the gradient strength upon image contrast which can be expressed in terms of the action of a “dipolar” filter. The image intensity and sharpness resulting from a CRAZED-like pulse sequence becomes sharper and clearer with increasing gradient modulation.

Imaging the spatial variation of the equilibrium nuclear magnetization M_0, can provide important information that can be used in treatment planning for neutron therapy and microwave hyperthermia. However, absolute measurement of M_0 is difficult due to the multiparametric nature of the NMR signal, i.e., dependence on pulse sequence parameters, the relaxation times T_1 and T_2, and the diffusion tensor. Bowtell and coworkers developed an NMR technique that allows mapping of the variation of the absolute value of M_0, based on the effect of distant dipolar fields in liquids [126]. The strength of the NMR signal in this case is proportional to M_0^2 for the CRAZED pulse sequence. This dependence means that the absolute value of M_0, can be measured by taking the ratio of the signal generated by long-range dipolar interaction effects to that generated in a special designed conventional experiment with similar flip-angle dependence for the RF pulses and similar relaxation time weighting [126].

Multiple spin echoes and interscan shifted stimulated echoes (SSTEs) generate a potential new mechanism for image contrast and were investigated by Mori et al. for the in vivo cat brain [127]. In the SSTE method the major signal contribution is due to interscan stimulated echoes for which the signal excited in the first scan is refocused during the acquisition period of the second scan (Fig. 16, top panel). The coherence pathway for SSTE (Fig. 16, top panel) is given by [124],

$$I_{iz} \xrightarrow{90^0} I_i^+ \xrightarrow{90^0} I_{iz} \xrightarrow{scan2,90^0} I_i^+ \xrightarrow{scan2,90^0} I_i^- \tag{34}$$

and in combination with gradient-based coherence filtering and image encoding lead to the images shown in Fig. 16, bottom panel. The SSTE sequence gives strong inverted T_1 contrast at short recycle delays and thus provides excellent gray-white matter contrast at high fields where this contrast is normally reduced due to larger values of T_1.

Multiple spin echoes (MSE) have increased sensitivity to diffusivity

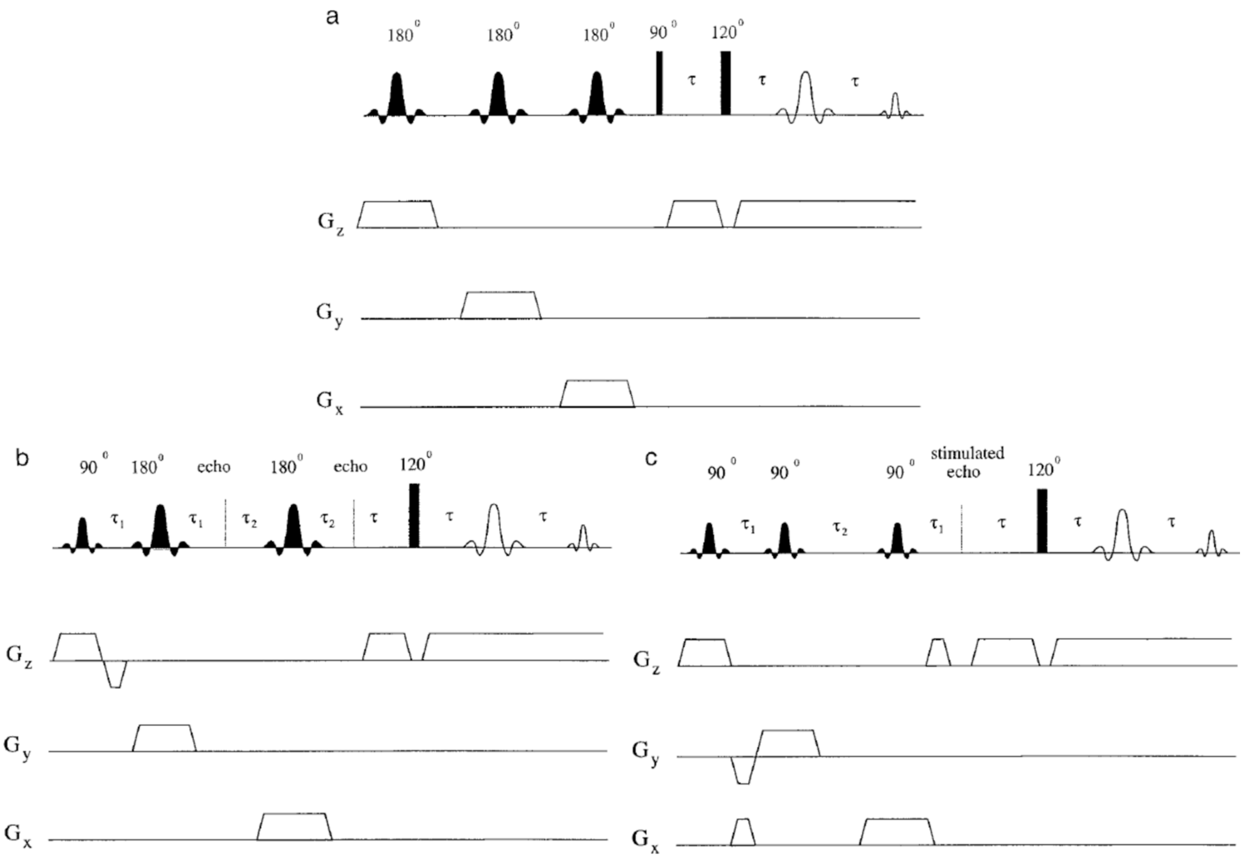

Fig. 17. Radio-frequency pulse sequences for acquiring MSEs from a localized volume. a) ISIS-MSEs, b) PRESS–MSEs, and c) STEAM-MSEs. Reproduced from [128] with permission.

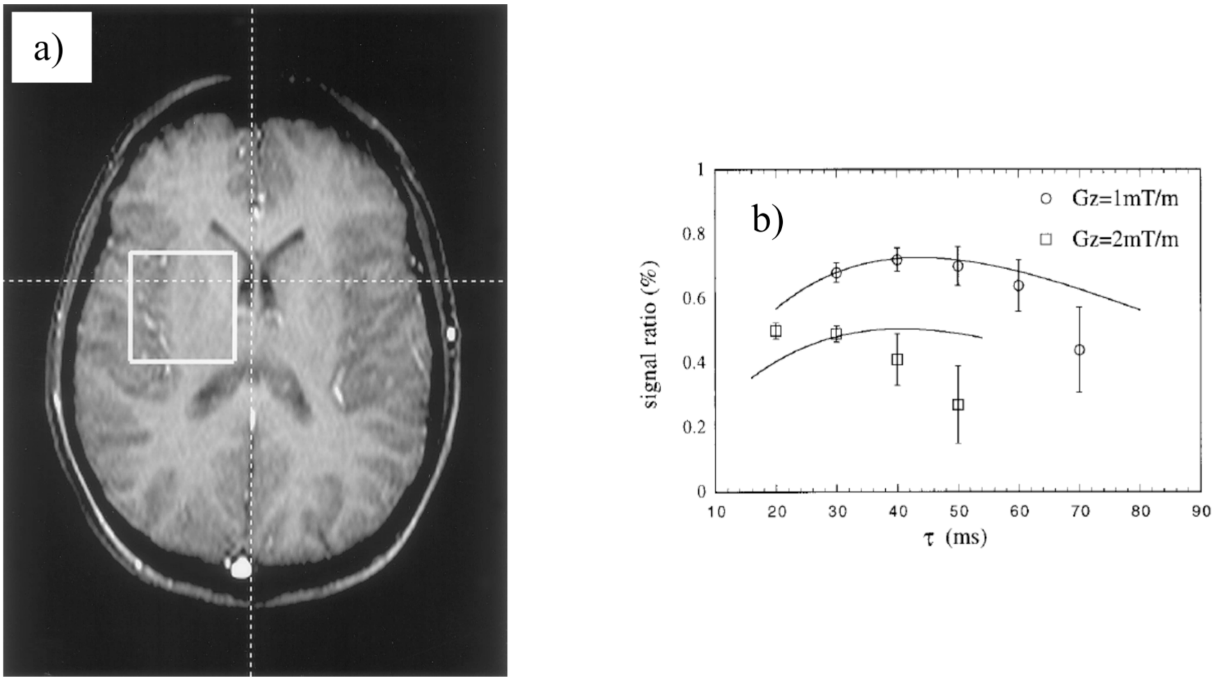

Fig. 18. A) transverse 2d flash mr image of human brain. the mse amplitude measurements were made on the voxel marked by a white box. b) ratios of 2nd and 1st MSE amplitudes. The curves have been generated by Eq. (34) for two values of correlation gradient G_z oriented along the static magnetic field. Adapted from [128] with permission.

and can be useful for in vivo human brain imaging with volume localized detection [128]. Modulation of longitudinal magnetization is destroyed by diffusion processes causing the long-range dipolar field to vanish for long echo times. Thus, the 2nd spin echo amplitude (A_2) strongly depends on the apparent diffusion coefficient D of molecules. Therefore, MSE imaging represents an alternative to the conventional pulsed gradient spin echo. The amplitudes of multiple spin echoes depend on the strength and orientation of the correlation gradient G. The following relation was derived for A_2/A_1 of the 2nd and 1st spin echo amplitudes [128]

$$\frac{A_2}{A_1} = \exp[2D^*/3]\beta F(D^*)\exp[-2\tau/T_2] \tag{35}$$

where $D^* = (\gamma^2 G^2) D\tau^3$, $\beta = \mu_0 \gamma \Delta M_0 [D(\gamma G)^2]^{-1/3}$, and the function F depends on the error function $\mathrm{erf}(D^{*1/2})$, [128].

Selective volume MSEs can be acquired by combining the basis sequence of Fig. 17 with standard volume selective procedures like ISIS [129], PRESS [119], and STEAM [130]. The performances of these volume selective methods, especially related to the effect on the second spin echo is discussed in Ref. [128]. Localized MSEs of brain white matter of in a human brain are shown in Fig. 18. Due to the limited sensitivity of spectrometer operating at 1.5 T only the second and first spin echoes are detected. Ratios of these are shown in Fig. 18b, for two values of the correlation gradient and compared with the theoretical Eq. (35). The theoretical fit used an average value for the D coefficient for different myelin fibers that is however difficult to estimate in the large voxel investigated. These results prove that MSEs are a potentially source of tissue contrast that can be controlled adjusting the correlation gradients without requiring microscopic spatial resolution.

The possibility to use the amplitudes of MSEs to investigate the microstructure of porous media was also discussed [40,131,132]. The 2nd MSE shows dips that can be explained by the role of internal gradients in the pores. The microstructure of porous media can be explored by modifying the correlation distance d changing the intensity of the gradients G, relative to the average pore size.

5.2. MRI of brain using iZQCs

The excitation of intermolecular zero-quantum coherences (iZQC) based on the physics of the CRAZED pulse-gradient sequence can be combined with spin-echo planar imaging (EPI) in order to obtain an image sensitive to the dynamics and structure of tissues. Such information is distributed over the correlation distance, which itself is dictated by the strength and length of the correlation gradient and are typically in the 100 μm – 1 mm range [133]. This dipolar correlation distance $d = \pi/(\gamma G T)$, is half the repeat distance of the magnetization helix created by the correlation gradient of strength G, which is oriented parallel with the static magnetic field and has duration T [121]. The iZQC image has useful characteristics such as: (i) better spatial resolution compared to conventional images, (ii) for short values of the pulse sequence evolution times the iZQC voxel intensities have a magnetization-squared weighting, and (iii) the image voxels show more contrast being encoding by susceptibility differences across the object.

An example of a pulse sequence used for this purpose is shown in Fig. 19a and different iZQC encoded images of human brain are shown in Fig. 19b. The iZQC signals from white matter and gray matter reach a maximum of almost 2 % of the single-quantum coherence signal, while the cerebrospinal fluid (CSF) signal is almost 4 % of this conventional coherence and still increasing in the echo-time region investigated (Fig. 19c), [133]. The measured $T_{2,\mathrm{ZQ}}$ for CSF is smaller compared to the T_2 of CSF and likely reflects flow-related dephasing. Furthermore, a difference between images obtained from single-quantum coherences (SQC) and iZQCs is apparent in the frontal lobe. In this brain region the T_2* decay of SQC causes signal loss that is not seen for an iZQC image. Moreover, the image contrast of the iZQC method is different from any conventional NMR image, particularly in regions with large susceptibility variations (Fig. 19b).

The coherence transfer pathway that was used to detect images via iZQC can be written for two equivalent spins i and j on different molecules as

$$I_{zi}I_{zj}\xrightarrow[\alpha]{}I_i^+I_j^-\xrightarrow[G,\tau_{ZQ}]{}\xrightarrow[\beta]{}I_{xi}I_{zj}\xrightarrow[D_{ij}I_{zi}I_{zj}]{}I_i^+ \tag{36}$$

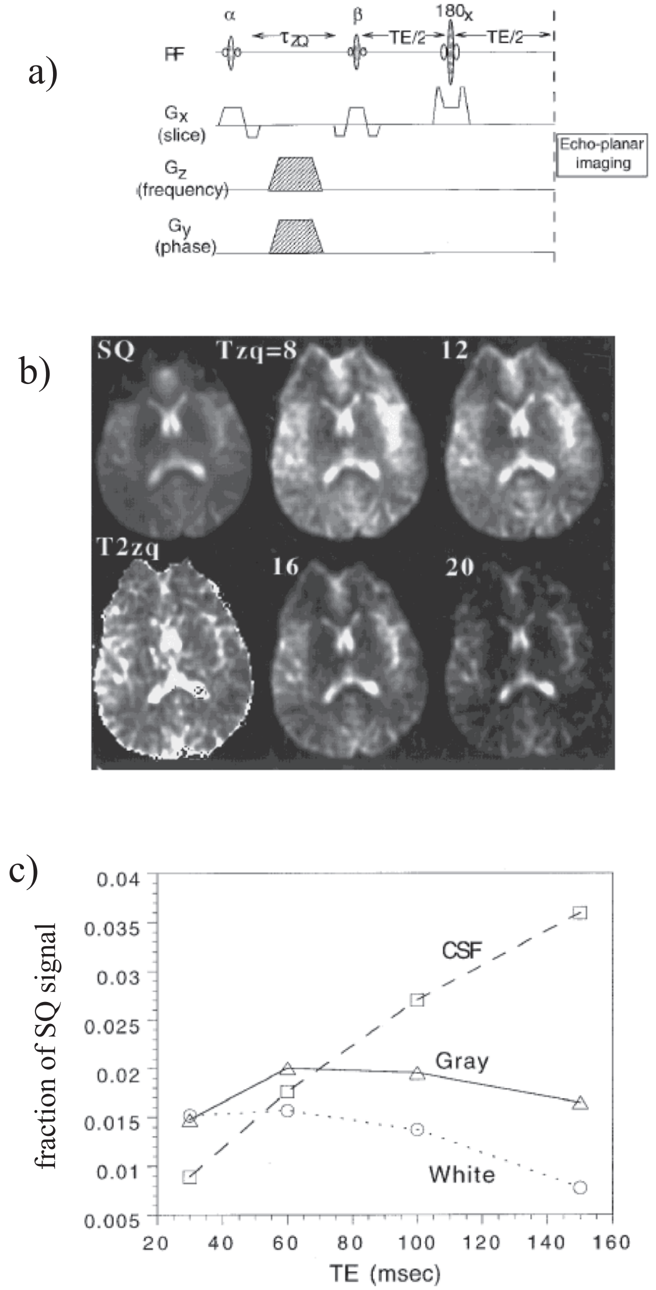

Fig. 19. a) iZQCs imaging pulse sequence with a slice selection gradient G_x and filter gradients during the iZQCs evolution of duration τ_{ZQ}. b) The axial image shown on the top left was obtained using only the EPI procedure. The brain image on bottom left is encoded by T_{2ZQ}. The four images shown on the right-side were obtained using $\tau_{ZQ} = 8$, 12. 16, and 20 ms. The imaging experimental parameters are given in Ref. [133]. c) Volume selective analysis of the relative iZQC signal as a function of echo time TE. Adapted from [133] with permission.

where the notation is defined in Fig. 19a and the long-range dipolar interaction is described by the operator $D_{ij}I_{zi}I_{zj}$. The iZQCs evolving during time τ_d are encoded by a factor related to the spin i and spin j resonance offsets that finally lead to an image voxel sensitive to susceptibility contrast. As discussed in Section 2 the detected spin echo has an amplitude M^+ given by [133],

$$M^+ \propto M_0 cos\beta J_1\left(-\Delta_s sin\beta\frac{TE}{\tau_d}\right) \tag{37}$$

where τ_d is the dipolar demagnetization time, and J_1 is the first-order Bessel function. In Eq (37), Δ_s is the orientation dependent Legendre factor of the distant dipolar coupling [120]. For small arguments of the Bessel function $J_1(x) \approx x/2$ and the voxel intensity is proportional to echo time TE. In this case the predicted signal reaches a maximum of 41 % of the full local magnetization at $TE = 2.6\ \tau_d$. The inverse dipolar demagnetization time is given by relation $\frac{1}{\tau_d} = \gamma\mu_0 M_0$, [120], and consequently. the iZQCs image is proportional to $(M_0)^2$.

The signal-to noise ratio of the image shown in Fig. 19b for a recycle delay RD can be written as: $S/N \propto \left[1-\exp\left(-\frac{RD}{T_1}\right)\right]^2/\sqrt{RD}$, and has a maximum at $RD_{max} = 2.34T_1$, where T_1 is the longitudinal relaxation time of the voxel (Fig. 19c). This maximum time is longer compared to the standard EPI image of $RD_{max} = 1.26T_1$, and therefore, the S/N of the iZQCs voxel image is smaller [133]. Transverse relaxation processes and molecular diffusion were neglected in the above discussion but in realistic images based upon iZQCs the voxel intensity is weaker compared to a conventional image using single-quantum coherence evolution.

We can summarize the salient features of MRI based on iZQC as: (i) The image reflects subvoxel structure. The practical resolution is of the order of a few micrometers for a small molecules with large diffusivity such water. (ii) The image contrast is affected by local susceptibility variations. Such contrast enhancement has been shown to be present for tumors in rat brain and is different from T_2 or T_2*, contrast [134]. (iii) The intensity of the iZQC signals is about one order of magnitude smaller compared to that of a conventional image. (iv) A large spin concentration is required to generate the long-range dipolar field. (v) The iZQC technique is superior to that based on iDQCs, because pulse sequence utilizing the latter leads to images that are more susceptible to motion and flow artifacts.

5.3. *Functional MRI of brain using iDQCs*

Intermolecular double-quantum coherences due to the long-range dipolar field have been utilized to perform functional MRI (fMRI) [135–142]. The results published in these references suggested that iDQC fMRI may provide higher activation contrast than conventional single-quantum coherence (SQC) detection. This is related to the fact that iDQCs show very intriguing properties that include a contrast based on dipolar interaction correlation distances, and the potential for more sensitive detection local distributions in magnetic susceptibility, which are essential for tumor oxygenation and brain functional studies using the BOLD effect. The correlation distance between 10 μm and a few millimeters which is under the control of the experimenter, may supply a structural probe for exploring the distribution of microvascular or cellular structures. The sensitivity of iDQCs to the blood oxygenation level-dependent (BOLD) effect is higher than that of conventional fMRI. However, an important limitation of iDQCs methods is related to their lower signal-to-noise ratio compared to the conventional methods based on SQCs. This effect is partially related to the time dependence of the decay rate of iDQCs that is greater than that of SQCs and the apparent diffusion coefficient for iDQCs is twice that of SQCs [138]. The contrast of MR images base on iDQCs is increased because for instance, $T^*_{2,iDQCs}$ includes the effect of local magnetic susceptibility [138].

Functional MR imaging techniques based on iDQCs are shown in Fig. 20a-c, and includes gradient recalled echo (GRE-iDQC), spin echo (SE-iDQC) and two π refocusing pulses (2π-iDQC). The π pulse within the τ period refocuses dephasing due to magnetic field inhomogeneity while retaining long-range dipolar interactions. It was found that the image intensity change upon auditory activation in the center of the cortex is several times larger in iDQCs images than that in SQC images (Fig. 20e). A higher percentage signal change due to activation was observed for the iDQCs-based measurements in comparison to the conventional SQC acquisition (Fig. 20e), [142]. The results discussed above demonstrate that it is feasible to obtain brain activity maps with iDQCs imaging even at the relatively low field of 1.5 T, if the pulse sequences parameters are

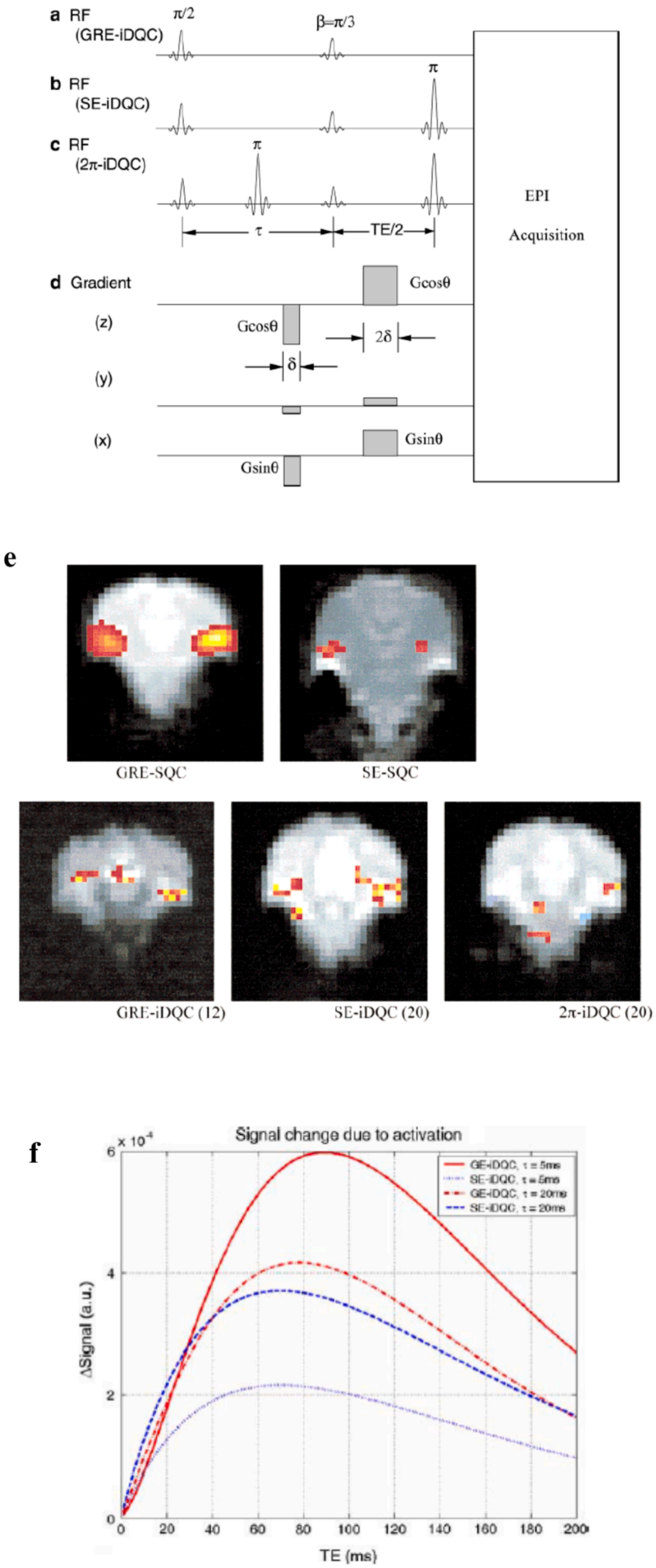

(caption on next page)

Fig. 20. Pulse sequences used for iDQCs imaging (a to c). In each case the EPI acquisition is applied at the end of double-quantum coherence filtration: the correlation gradients shown in d) were applied for all fMRI measurements. The different pulse sequences correspond to a) conventional gradient recalled echo (GRE-iDQC), b) spin echo (SE-iDQC), and c) π pulses applied during the evolution and detection periods (2π-iDQC). e) Activation maps of auditory stimulation in the human brain at 1.5 T using single-quantum coherences (SQCs, top) and iDQCs (bottom) detected by the pulse sequences shown in a)-c). The number in parentheses is the evolution time of the iDQCs in ms. f) Changes in the signal intensity for visual brain activity measured using two pulse sequences similar to a) and b) using the parameters given in Ref. [142]. Adapted from [138] and [142] with permission.

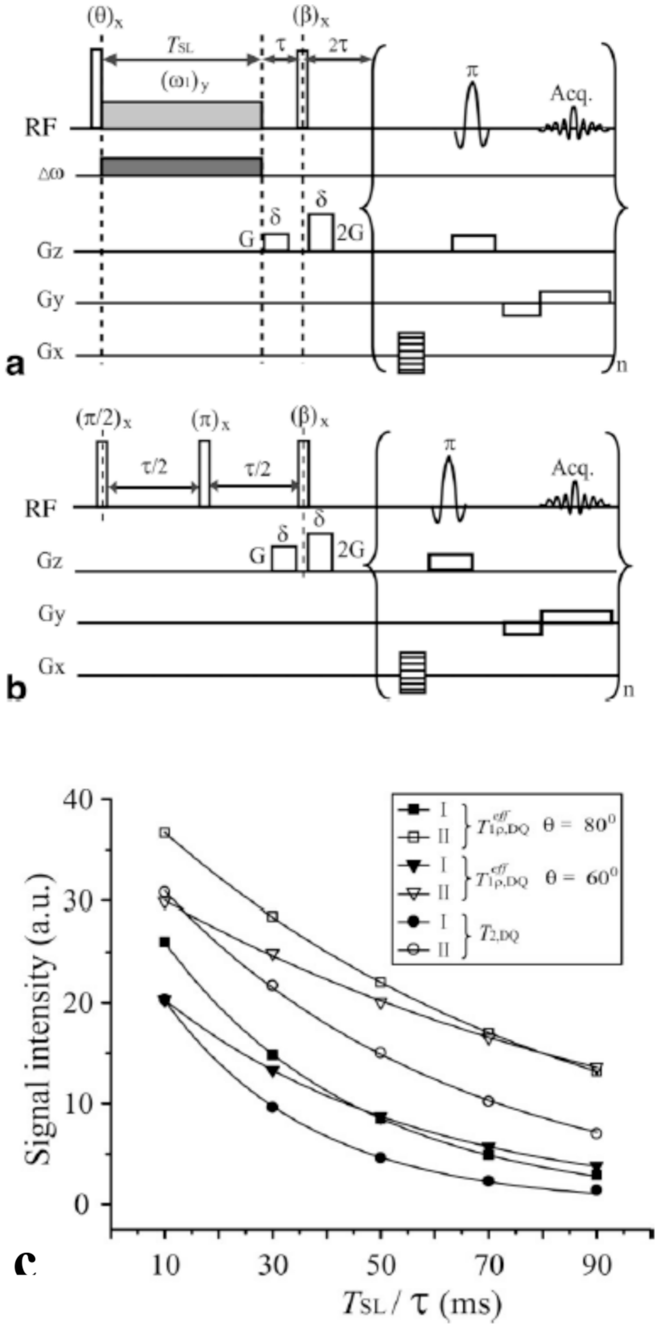

Fig. 21. a) Pulse sequence for forming iDQCs MRI weighted using off-resonance longitudinal relaxation $T^{eff}_{1\rho,DQ}$ in the tilted rotating frame in the presence of a spin-locking RF pulse associated with a resonance offset. b) The encoding of iDQCs images using iDQCs transverse relaxation $T_{2,DQ}$ or $T^{*}_{2,DQ}$. The relaxation parameter maps were obtained by following the modified CRAZED sequence with a standard fast spin echo imaging sequence. c) Region-of-interest signal intensity of an agarose-gel phantom with different concentration (labelled with I and II in the inset) as a function of evolution durations T_{SL} for $T^{eff}_{1\rho,DQ}$ longitudinal relaxation and τ for $T_{2,DQ}$. Adapted from [147] with permission.

optimized for sensitivity.

To investigate parameters that influence iDQCs signal changes observed during neuronal activity, carbogen-inhalation experiments were performed to produce a pure hydrodynamic response without affecting oxidative metabolism [143]. BOLD-weighted fMRI depends on multiple physiological parameters, including changes in the cerebral blood flow, the cerebral blood volume, and the cerebral metabolic rate of oxygen.

The longitudinal relaxation time in the rotating reference frame is a valuable quantity for probing low-frequency molecular processes that occur at a range of frequencies determined by the amplitude of a spin-lock pulse [144]. Magnetic resonance images weighted by $T_{1\rho}$ provide unique contrast, which has been investigated in various biological tissues, including head and neck tumors [145]. The feasibility of quantitative $T_{1\rho}$ imaging in human brain has been tested on a 4 T MRI scanner [146]. The measured $T_{1\rho}$ values were compared with T_2 values in white and gray matter. The results demonstrated differential sensitivity of these methods to proton dipolar interactions and/or exchange as well as diffusion in local microscopic field gradient.

The radio-frequency field with angular amplitude ω_1 and frequency offset $\Delta\omega$ constitute an effective spin-locking field along the $\acute{z}$- axis of the tilted rotating frame, with an effective amplitude $\omega_e = \sqrt{(\omega_1)^2 + (\Delta\omega)^2}$ and a tilt angle $\theta_e = arctan(\omega_1/\Delta\omega)$ with respect to the laboratory frame z-axis. In this tilted rotating frame the intermolecular long-range dipolar field is reduced in strength by a factor of $(-1/2)\sin\theta_e$. It should be noted that $T^{eff}_{1\rho,DQ}$, is sensitive to θ_e and ω_e, [148]. In the presence of slow motions, the dominant terms in the relaxation rate $1/T^{eff}_{1\rho,DQ}$, are related to the spectral density functions $J_0(2\omega_e)$ and $J_0(\omega_e)$, [146]. Therefore, molecular fluctuation rates on the order of the spin-locking frequency will significantly contribute to the $T^{eff}_{1\rho,DQ}$, relaxation. If slow motions are present, a significant increase in the value $T^{eff}_{1\rho,DQ}$ will take place with an increase in the frequency offset $\Delta\omega$ leading to an increase in the effective RF frequency ω_e, and a decrease in the tilt angle θ_e.

The off-resonance spin-locking method can also be applied to spin systems with long-range dipolar interactions using the CRAZED pulse sequence for generating iDQCs MRI [147]. The pulse sequence combining longitudinal off-resonance spin-locking relaxation, the CRAZED pulse sequence by selection of iDQCs and a fast spin-echo imaging sequence is shown in Fig. 21a. Transverse double-quantum coherence relaxation is measured by the sequence shown in Fig. 21b. Signal decays in the region of interest (ROI) for an agarose-gel phantom for the above experiments are shown in Fig. 21c. These results represent are a continuation of a technique for on-resonance iDQCs, $T_{1\rho,DCQ}$-weighted on a 7 T microimiging scanner [148]. Imaging based on $T^{eff}_{1\rho,DQ}$ has reduced radio frequency power deposition compared to on-resonance spin-locking, which is advantageous for human MRI. Moreover, the angle of the effective RF field and spin-locking frequency are two experimental parameters that can be manipulated to obtain different molecular dynamics contrast within tissues.

5.4. *MRI using simultaneous acquisition of iMQCs*

The imaging techniques using iMQCs discussed above only acquire one coherence transferred echo per pulse sequence. A newer pulse sequence called Multiple Echo Detection CRAZED (MultiCRAZED) was reported that detects five order of coherences (2, 1, 0, −1, and −2),

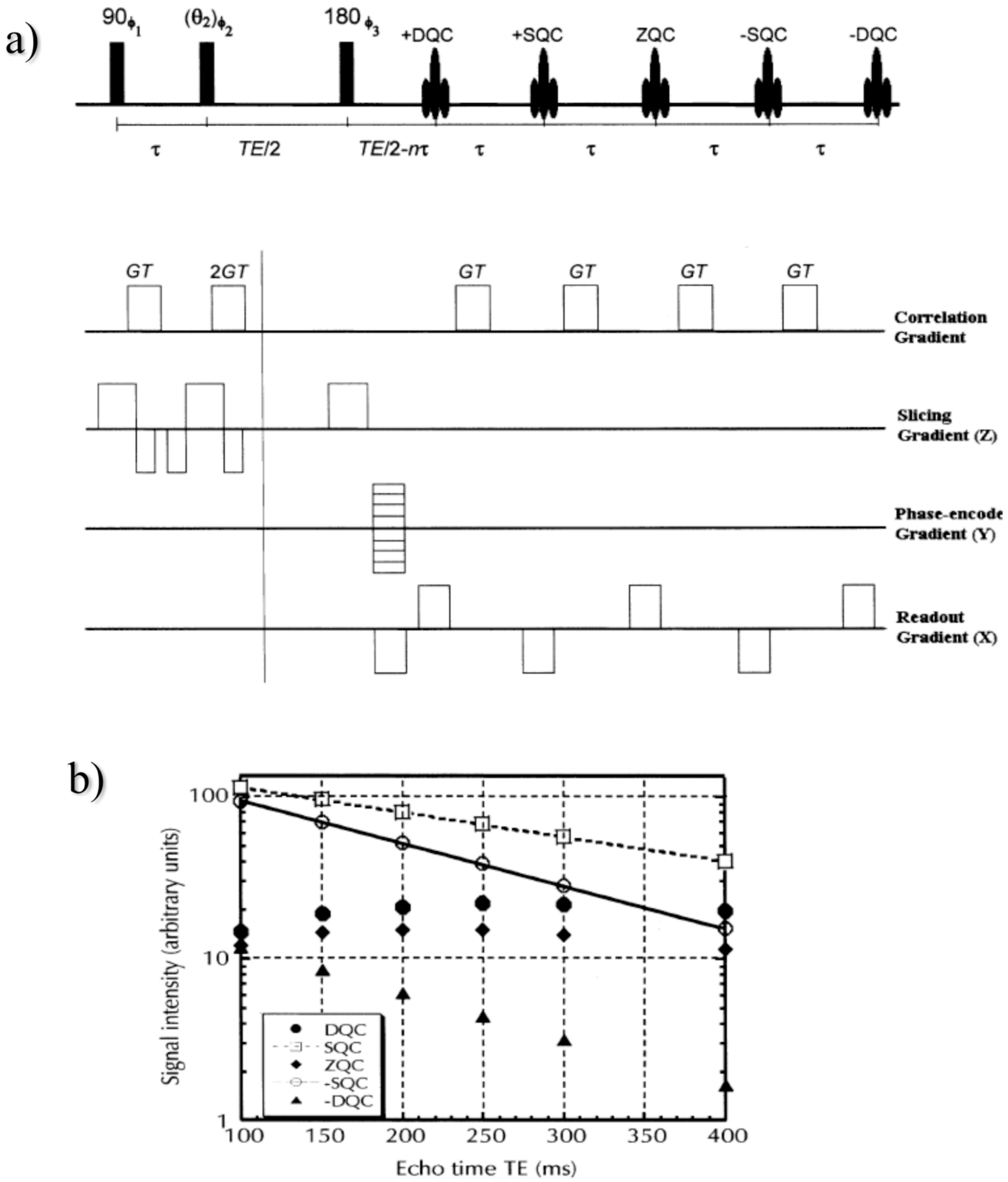

Fig. 22. A) sequence of rf pulses in k-space and gradients for MultiCRAZED. All the five echoes sample the same line in k-space. b) Image intensity variation as a function of spin echo time TE. The correlation gradient was G = 3.958 G/cm giving a correlation distance d = 200 μm. The image parameters are given in Ref. [149]. Adapted from [149] with permission.

[149]. This pulse sequence used for obtaining simultaneous images from double-quantum, zero-quantum and conventional single-quantum coherences is depicted in Fig. 22a and differences in signal intensity as a function of echo time TE are shown in Fig. 22b. The spin echoes are separated by a relatively short time, and hence, the possibility of overlap between different coherences cannot be ignored particularly, for structured objects. However, it was shown that a straightforward method based on phase cycling of the first pulse $90_{\phi1}$ (Fig. 22a), will allow the separation of the signals using a five phase steps. To prevent.

possible complications from 3th order quantum coherences an eight-step phase cycle with a 45° increment was implemented [150]. Moreover, the flip angle of the second RF pulse was switched between θ and π-θ, which suppresses the residual z-magnetization whereas the signal from iZQC will add up. The signal intensities of the images edited by different orders of coherences are compared in Fig. 22b. First order quantum coherences show simple exponential decay; other coherence orders images show more complex behavior. It was proved experimentally that the signal decay changes with correlation distance. For example, −2-quantum correlation images decay more rapidly than do the + 2-quantum images. These differences arise from diffusional effects. The magnetization which originates as n-quantum is modulated as (n-2)γGT. Thus, the + 2-quantum images is minimally affected. The zero-quantum component decays with rate $(2\gamma GT)^2D$, and the −2-quantum images decays with rate $(4\gamma GT)^2D$, [149]. The images edited by multiple quantum coherences reflect different weightings than traditional contrast mechanisms such as diffusion, and also show iMQC contrast that is not any combination of conventional contrast mechanisms. Applications for imaging biological tissues were not reported. To a good approximation the results of the MultiCRAZED technique can be described by a theoretical model based upon the quantum–mechanical coupled-spin approach that considers the spin dipolar interaction separated by the correlation distance which is tuned by correlation gradient pulses of area GT [149].

5.5. Effects of residual single quantum coherences (SQCs) upon iMQCs images

Payne et al. found that a mixture of components arising from iDQCs and residual SQCs produces significant changes in the MRI detected signal at certain correlation distances [150]. Residual SQCs are a potential confounder in iMQCs studies and might explain some of the discrepancies reported in the literature. These residual coherences can be due to three different mechanisms: (i) intense high spatial frequencies, (ii) stimulated echoes, and (iii) strong spatial encoding gradients.

An appropriate RF pulse phase cycling scheme can be employed to suppress high spatial frequency components arising from undesired coherence pathways. Gradient orientation cycling may be used to suppress stimulated echoes when investigating a range of correlation distances, without the need for long repetition times. In imaging experiments, when orienting the correlation gradient parallel to the direction of the frequency or phase encoding gradients, the correlation distance must be significantly smaller than the image pixel dimensions to avoid refocusing coherence pathway echoes in the image k-space data. In this case SQCs can be suppressed via appropriate phase cycling [150].

5.6. Numerical studies of iMQCs contrast enhancement in MRI

An efficient and fast numerical algorithm which switches back and forth between real and Fourier spaces was proposed by Warreńs group to study long-range dipolar field effects for heterogeneous 3D-dimensional structures, high-resolution NMR in inhomogeneous magnetic fields, and contrast enhancement in MRI using iZQCs and iDQCs [29,151].

To describe the spin system response for the CRAZED sequence the quantum-mechanics formalism based on the density operator allows a deep understanding of how the pulse sequence will behave. Nevertheless, the classical Bloch equations formalism is much more efficient for numerical calculations. The components of the local spin magnetization vector $\boldsymbol{M}(\boldsymbol{r}, t)$ are described by nonlinear coupled partial differential

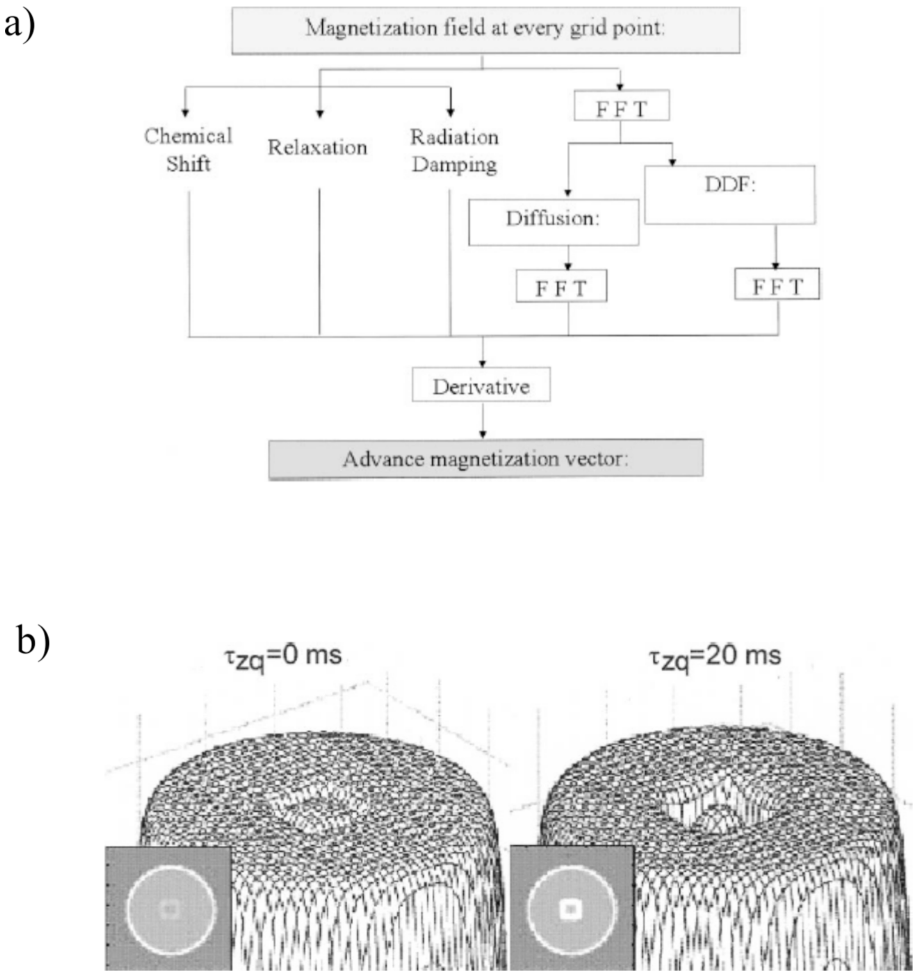

Fig. 23. a) Schematic of the algorithm that allows numerical calculation of long-range dipolar field, diffusion, chemical shift, magnetization relaxation, and radiation damping effects on local magnetization at each time step $\boldsymbol{M}(\boldsymbol{r}, t + \Delta t)$. b) Numerical simulation of the contrast from chemically inequivalent spins using conventional iZQCs CRAZED sequence for two values of the time between the 90° pulses τ_{zq}. The decrease in the amplitude of the voxelś signal produced by the correlation gradients is only significant when spins with different chemical shifts are one half-helix apart. Adapted from [151] with permission.

equations that must be integrated from t = 0 to t = t_{final},

$$\frac{\delta \boldsymbol{M}(\mathbf{r},t)}{\delta t} = \gamma \boldsymbol{M}(\boldsymbol{r}) \times \left\{ \left[\frac{\Delta\omega}{\gamma}\hat{\boldsymbol{z}} + G(\hat{\boldsymbol{s}}\bullet\boldsymbol{r})\hat{\boldsymbol{s}}\right] + \boldsymbol{B}_d(\boldsymbol{r}) + \boldsymbol{B}_r(\boldsymbol{r})\right\} - \frac{M_x(\boldsymbol{r})\hat{\boldsymbol{x}}+M_y(\boldsymbol{r})\hat{\boldsymbol{y}}}{T_2(\boldsymbol{r})} + \frac{M_0(r)-M_z\hat{\boldsymbol{z}}}{T_1(\boldsymbol{r})} - D\nabla^2\boldsymbol{M}(\mathrm{r},t). \tag{38}$$

The expressions for long-range dipolar interactions are given in Section 1. These equations are nonlinear, the magnetization vector of each time step depends explicitly on the starting conditions. Moreover, for chemical shifts, applied correlation gradients and relaxation alone, each partial differential equation expressed as a function of spatial coordinates $\boldsymbol{r}$, is unrelated to the others, so can be calculated directly. To compute numerically the effect of radiation damping, finding the average magnetization in the transverse plane is the only necessary calculation. While this term is nonlocal, it is inexpensive to calculate it because $\boldsymbol{B}_r$ (**r**) needs to be calculated only once per time step [151]. However, the values of the long-range dipolar field and the diffusion term relay explicitly on each point's surroundings. The schematic of the algorithm for calculation of the five terms of Eq. (38) is shown in Fig. 23.

The simulations discussed in Refs. [29,151] have shown that MR images based on iZQCs provide a very powerful method for removing residual inhomogeneous broadening using parameters that approximate the expected distributions from real magnets. In addition, they also show that MR images from the iZQCs and iDQCs CRAZED pulse sequence really do produce fundamentally different contrast than does conventional imaging. Although the actual resolution of the MR image is limited by signal detection sensitivity, the iZQC-CRAZED experiments can specify the distance between correlated spins. Numerical simulations show that the image resolution can be one or two orders of magnitude finer than for conventional images. Moreover, the refocusing 180° RF pulse inserted in the excitation and evolution periods of CRAZED leading to the modified CREAZED, (modCREAZED) sequence eliminate chemical shift evolution as a contrast mechanism. The subtraction of the conventional iZQC-CRAZED image from the mod(iZQC-CRAZED) eliminates contrast from spin density and relaxation, leaving only contrast from chemical shift differences on the distance selected by the correlation gradient.

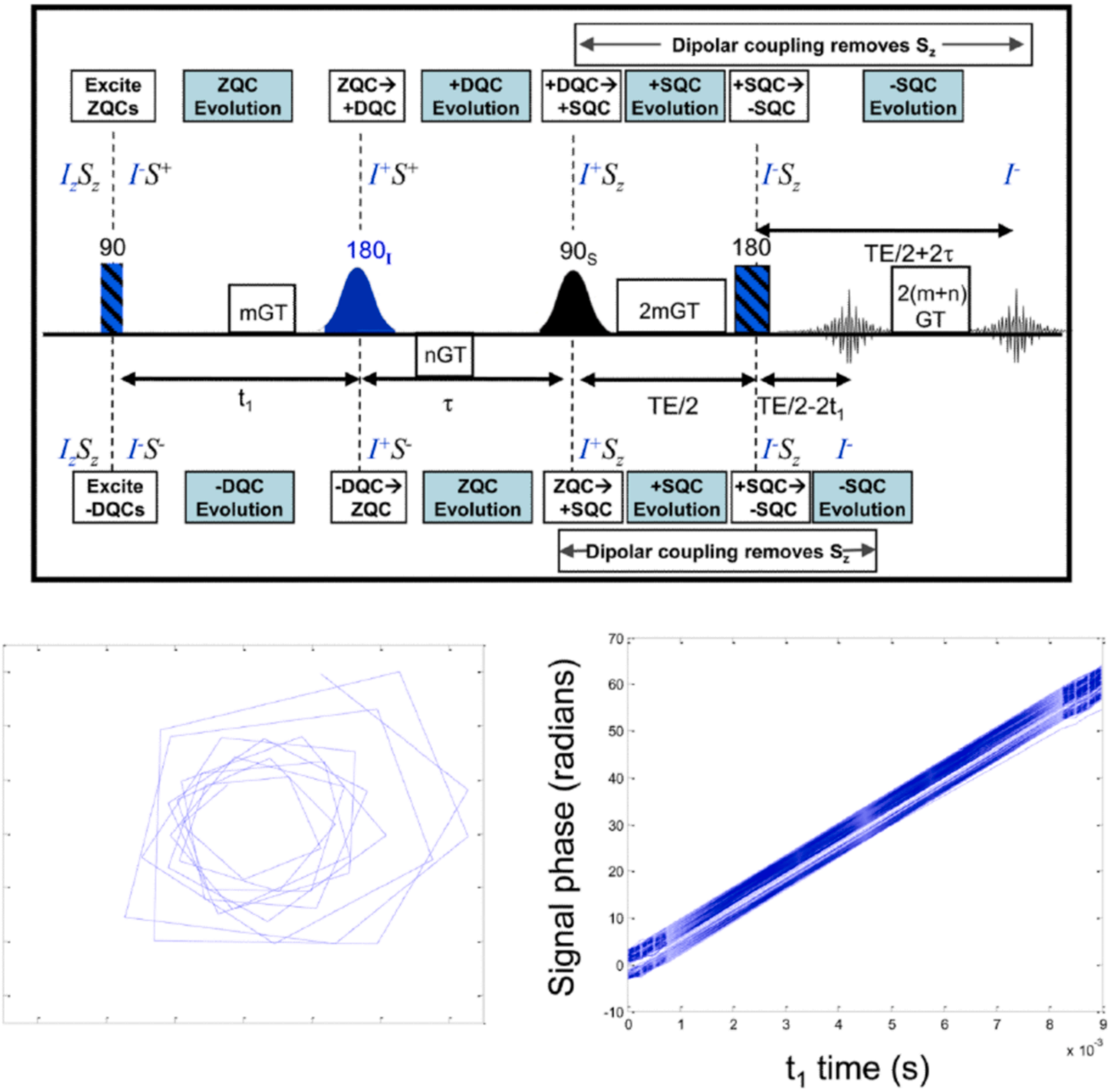

Fig. 24. The HOT pulse sequence used to detect temperatures using iMQCs (upper panel, middle line). In this panel two coherence pathways are shown. The first (top line) initial evolution of iZQCs is converted to iDQCs whereas in the second (bottom line) initial evolution of iDQCs is converted to iZQCs. The left bottom panel shows representative signal evolution due to the HOT pulse sequence. The phase of the NMR signal changes as t_1 changes and the rate of that change can be used to determine the iZQC frequency that is shown in right bottom frame. Reproduced from Ref. [173] with permission.

5.7. *Enhancement of magnetization transfer effects using iMQCs filtered NMR*

The contrast in MRI based on changes of the water magnetization (M_z) as a result of magnetization transfer to tissue macromolecules has been obtained by a variety of methods such as magnetization transfer contrast (MTC), and chemical exchange dependent saturation transfer (CEST), [152–155]. Sensitivity to the macromolecular content of the tissue can be also revealed by various NMR filters such as Goldmann-Shen [156], Edzes-Samulski [157], DQ filtered-magnetization transfer [158], and magnetization exchange imaging [159]. A combination of these methods with iMQCs was reported by Eliav and Navon to enhance the contrast of MRI [160]. For the MTC method an effect of (M_z/M_0) becomes $(M_z/M_0)^l$, where l is the rank of the irreducible tensor operator $T_{l,m}$, constituting the iMQCs. The simplest pulse sequence that combines MTC method with iMQC is described in Ref. [160]. The flip angle β is selected such to maximize the transfer function of the $T_{l,m}$ coherences to $T_{l,-1}$. For instance, for iDQCs with m = -2 it is obtained β = 60°, [160]. The enhanced contrast by combination with iDQCs is not limited to MTC but can be obtained with any experiment that is based on modulation of the water M_z magnetization such as Goldman-Shen filter [156] or other exchange methods [160].

6. Accurate temperature MR imaging using intermolecular multiple-quantum coherences

6.1. *Principles of thermometry using NMR*

In medicine the temperature distribution in the human body has been linked to the critical regulation of metabolism, immune function, and longevity. Moreover, combining hyperthermic therapy with radiotherapy can results in a wide variety of benefits such as increased tumor response and increased survival rates [161–163]. Hyperthermic therapy requires the accurate delivery of a prescribed thermal dose generally in the range of 40 °C-45 °C or higher for thermal ablation [164]. Invasive thermometry usually done via multiple thermocouples was used for in vivo monitoring. A non-invasive approach is given by MR imaging [165–176].

The temperature-sensitive magnetic resonance parameter most commonly used is the change in chemical shift of ^{1}H in water with temperature. The chemical shift is determined by the local electron orbitals [4]. The change in the hydrogen bonding network during heating will lead to a change in chemical shift. These changes cause a shift in ^{1}H resonance frequency of about 0.01 ppm/K, and this effect is referred as the proton resonance frequency shift. It is important to realize that non-water protons are not shifted by the same amount [174]. Furthermore, the observed Larmor frequency of a nucleus in a medium depends both on the local magnetic field and the chemical shift [165,168]. The resonance frequency can be written [177],

$$\sigma = \gamma(1 - \sigma(T))B_{local}(T) \tag{39}$$

where γ is the magnetogyric ratio and σ(T) is the temperature-dependent chemical shift. The local magnetic field strength is given by

$$B_{local}(T) \cong \left(1 - \frac{2\chi(T)}{3} - \sigma(T)\right)B_{macroscopic} \tag{40}$$

where χ is temperature dependent magnetic susceptibility. The temperature dependence of the magnetic susceptibility is affected by the tissue type. Moreover, in lean tissues the chemical shift dominates [165]. The macroscopic magnetic flux density $B_{macroscopic}$, depends on the static magnetic field B_0, the susceptibility distribution and sample geometry. From Eqs. (39) and (40) it is obvious that proton resonance frequency shift methods are strongly affected by magnetic field instability and heterogeneity of the MR imaged object. Therefore, development of novel MR imaging methods for temperature measurements is of interest.

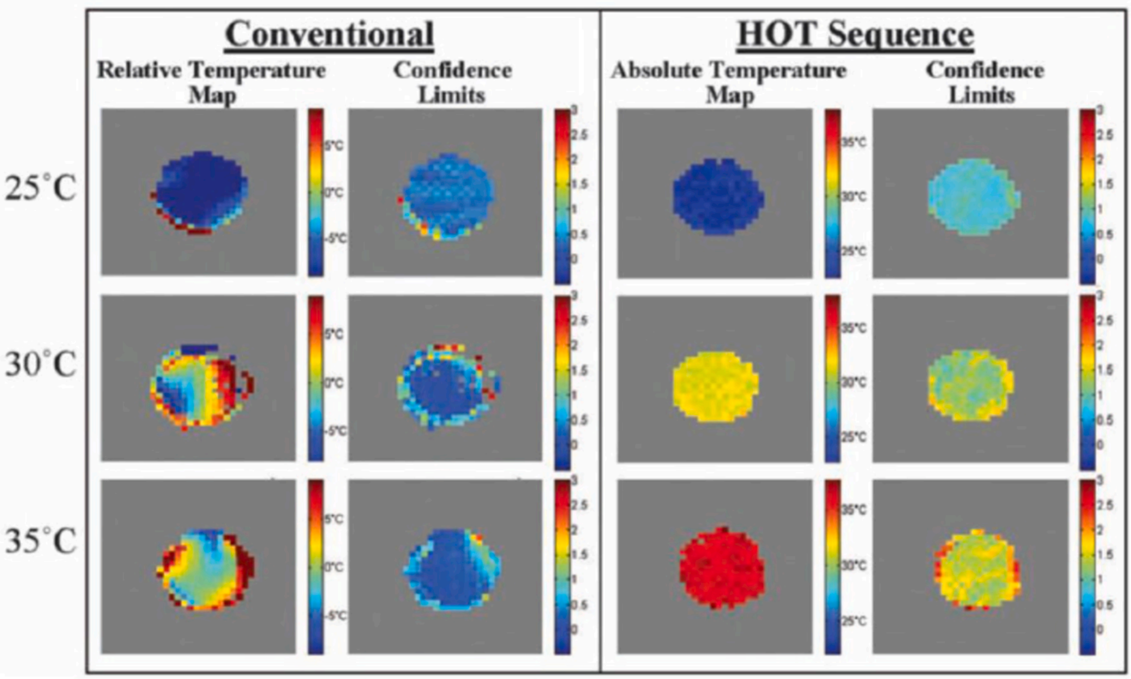

Fig. 25. The temperature MR images obtained using the HOT pulse sequence in a cream phantom represented by a homogenous mixture of water and fat. The sensitivity of the HOT pulse sequence is demonstrated by using it to detect radio-frequency heating. The images were obtained by using the RARE image acquisition method applied after the preparation of iMQCs [178,179]. The conventional temperature maps were taken by monitoring the changes in the phase of the water signal (Fig. 25) as the phantom was heated from 25 °C to 35 °C. Large distortions in the detected temperature were observed. These distortions were eliminated using the HOT method. Reproduced from Ref. [173] with permission.

6.2. Accurate thermometry MR imaging using the HOT pulse sequence

A method to obtain absolute and accurate temperature images insensitive to errors due to changes in magnetic susceptibility, of both water and fat, as well as magnetic field instabilities, magnetic field inhomogeneity, and drift based on iMQCs [172,173] was proposed.

To understand the underlying physics of the iMQCs method we consider a sample comprising a mixture of two chemical species such as water and fat in tissue containing respectively I spins and S spins. Temperature detection with iMQCs requires a mixed spin system e.g. in this example signals from water-fat iMQC transitions, but not from water-water or fat-fat iMQC transitions (which are temperature insensitive) [177] In order to detect clean iMQCs temperature maps insensitive to field inhomogeneity and magnetic susceptibility effects it is therefore necessary that signals from I and S spins coherences should be filtered out by the HOT pulse sequence. The pulse sequence depicted in Fig. 24 selectively transfers coherences that evolve off-resonance in the indirectly detected dimension, prompting the acronym HOMOGENIZED with Off-resonance Transfer, or the HOT pulse sequence [173]. See Fig. 25..

MR images of the objećts temperature distribution were obtained from the pulse sequence depicted in Fig. 24 which is based on a filter that can remove contamination from iZQCs of the same spin species, as well as removing conventional magnetization. The HOT pulse sequence uses frequency selective inversion pulse (π-pulses) applied only to one chemical species for instance either water or fat. This π-pulse converts the mixed spin iZQCs to mixed spin iDQCs and vice-versa as shown in the product operator transformations,

$$I^-S^+ \overset{\pi_I}{\leftrightarrow} I^+S^+ \qquad (41)$$

and

$$I^+S^+ \overset{\pi_I}{\leftrightarrow} I^-S^+ \qquad (42)$$

If a DQ filter is applied on the above coherences, i.e.: τ-GT-θ_{mix}-2τ-2GT, all coherences will be dephased with the exception of iDQCs existing during the interval τ and that are transferred into iSQCs by the mixing pulse θ_{mix}. As mentioned by Jenistra et al. [173] in this single acquisition HOT sequence the magnetic field gradients also dephase the SQCs created before or after the mixing pulse, reducing the large static SQC component of the NMR signal. To apply this idea to thermometry a two-window HOT pulse sequence (Fig. 24) was developed in Ref. [174] and is discussed at length in Ref. [177]. In the first coherence pathway corresponding to the transfer of iDQCs to iZQCs, the signal is refocused in the first acquisition window. The gradient mGT causes a phase shift of 2mGT and the coherences evolves for a period $2t_1$. Subsequently, it is converted to iZQCs by the selective π_I inversion pulse, on which the subsequent gradient nGT has no effect, and the coherence then evolves at the frequencies of the iZQCs, (ω_I-ω_S) during τ. The same NMR physics takes place for the second coherence pathway when iZQCs → iDQCs. For the t_1 evolution the iZQCs experiences no gradient and evolves at the frequency of (ω_I-ω_S). The iDQCs is produced by a frequency selective inversion pulse and acquires a phase shift 2nGT from the gradient and evolves at the frequency ($\omega_I + \omega_S$). After conversion to SQCs by the mixing pulse and an additional phase shift of 2mGT, the net effect of the gradient will be 2(m + n)GT The refocusing pulse is followed by a gradient of area 2(m + n)GT and evolution for 2(τ + t_1) refocuses the coherences that are then acquired in the second acquisition window [177].

Homomolecular spin suppression can be obtained without field gradient filters by using phase cycling methods that achieve higher signal-to-noise ratio and a phase cycle which is compatible with both coherence pathway was given in Ref. [177]. Furthermore, the HOT pulse

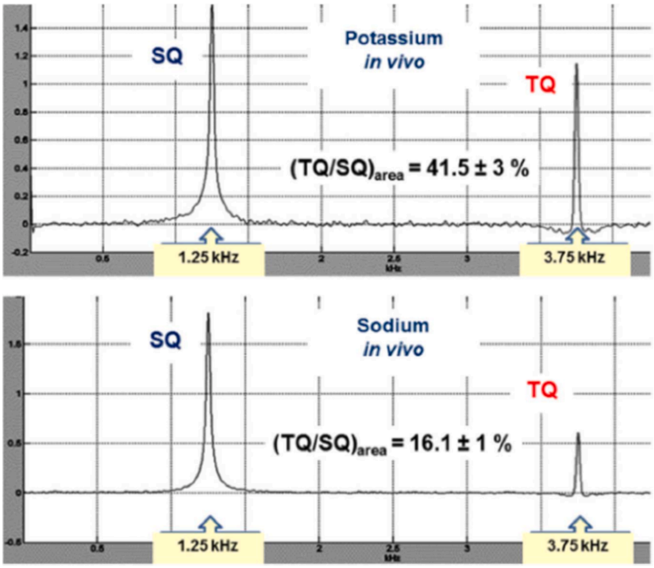

Fig. 27. SQ and TQ edited spectra of ^{39}K and ^{23}Na in the rodent head in vivo. In the case of sodium, the concentration ratios correspond to the total head sodium for the SQ peak and to intracellular sodium concentration for the TQ peak. In the case of potassium, the TQ peak arises mainly from the total intracelular potassium. Reproduced from [180] with permission.

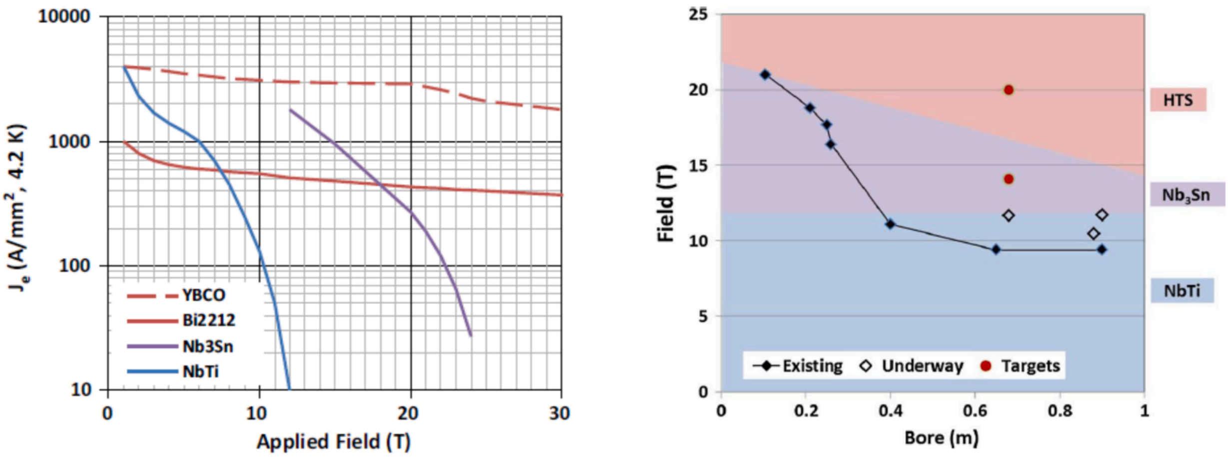

Fig. 26. Left-hand panel shows maximum current density of superconducting wires as a function of the applied magnetic field. Parameters for existing magnets and projects as at 2016 are shown in the right-hand panel, together with the required superconductor. Adapted from Budinger et al. [180] with permission.

sequence can be modified such that this method can obtain spin density images of both species [177].

Temperature imaging methods using iMQCs allowed imaging the temperature on an absolute scale, while for the first time being insensitive to motion, susceptibility effects and instability of magnetic field [173,177]. In a realistic application, the intensity of a mixed spin iMQCs signal between water and a metabolite peak will be approximately 10 % of the metabolite peaks. This is the case in the brain but slightly larger voxels would be required for direct spectroscopic detection and would permit temperature detection without reducing the temperature accuracy [177].

7. Intermolecular magnetic resonance spectroscopy at high and ultra-high magnetic fields

7.1. NMR features at ultrahigh magnetic fields

The traditional advantage of NMR at high magnetic fields is related to improved sensitivity that leads to higher spatial resolution in MRI and volume localized MRS [180–183]. Furthermore, it will lead to enhanced spectral resolution by increasing chemical-shift dispersion [184]. In such conditions NMR spectroscopy of low magnetogyric ratio nuclei in restricted geometry, powders with large quadrupole interactions, molecular alignment due to anisotropic magnetic susceptibility [185] among others can be investigated.

Due to limitation in the value of the upper-critical field of superconductor materials it appears unlikely that persistent pure superconducting magnets beyond 23 T can be constructed for NMR in the near future. NMR spectrometers based on resistive electromagnets or resistive-superconducting hybrid magnets can achieve substantially higher fields such as the 45 T hybrid magnet installed at National High Magnetic Field Laboratory (NHMFL) [180]. However, the spatial homogeneity and temporal stability of this hybrid magnet are such that high-resolution NMR experiments are difficult to be perform. Modeling and experimental studies show that the timing and resolution requirements for imaging the microstructure of human brain require higher magnetic fields than currently available (Fig. 26) [180]. MRI at high fields will allow reduction of the voxel volume to 0.1 μL or less and will provide unprecedented resolution gains in a spatially non-homogeneous and curved structure such as the brain. It will also allow quantitative mapping of the distribution of aggregated proteins by measuring susceptibility anisotropy. Moreover, if we assume that signal-to-noise ratio (SNR) scales linearly with the strength of magnetic field (B_0) in the brain and if we consider the blood oxygen level-dependent (BOLD) effect to increase at least linearly with B_0, then the combined effects on SNR and BOLD contrast would translate into a quadratic gain in contrast-to-noise ratio for mapping functional signal [174]. Single-quantum (SQ) and triple-quantum (TQ) spectra of ^{23}Na and ^{39}K nuclei at 21.1 T in the rodent brain show a slightly better than linear gain in SNR when the field is increased from 9.4 T to 21.1 T (Fig. 27), [180,186]. Finally, this is expected to lead to ultimate resolution of functional maps of the human brain. This can also be supported by optimization of gradient performance and new innovations in radio-frequency and shim coil design [182 and references therein].

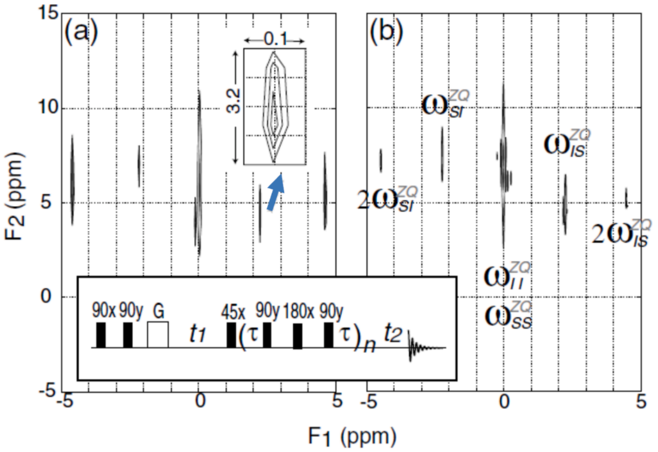

Fig. 28. Experiments at 25.0 T using a resistive electromagnet (a) and simulated iZQCs spectra (b) using composite CPMG-HOMOGENIZED pulse sequence (see insert). The insert in (a) shows the magnified ω_{IS}^{ZQ} peak, plotted at the same contour level. This 2D heteronuclear spectrum was obtained from a 1:1 water/acetone mixture in a 5-mm NMR tube at 20 °C. The simulation assumes a field inhomogeneity of 1 ppm/cm, field fluctuations modeled by Gaussian white noise with 0.5-ppm standard deviation, 1 kHz upper frequency limit, and a sample length of 0.9865 cm sampled by 400 spatial points on the z axis. The pulse sequence parameters are given in Ref. [188]. Reproduced from Lin et al. [188] with permission.

7.2. The HOMOGENIZED pulse sequence at high magnetic fields

A possible approach to recording NMR spectra free from the effects of field instability is based on multiple-quantum NMR. For instance, total spin coherence transfer echo spectroscopy takes advantage of the properties of the unique transition between the extreme eigenstates (i.e., eigenstates with maximal energy separation) of a coupled spin system to record multiple-quantum spectra free from inhomogeneous broadening yet sensitive to *J* couplings and chemical shift differences [187]. The same insensitivity to field variation is offered by zero-quantum coherence (ZQC).

Warren and coworkers suggested a procedure to effectively improve performance at ultra-high magnetic field in terms of resolution and stability by spin manipulation that exploits iZQCs [188]. Hence, high-resolution liquid state NMR at very high magnetic fields was proved to be possible. For this purpose a detection method termed HOMOGENIZED was presented that removes inhomogeneity while retaining chemical shift differences and *J* couplings [71]. This pulse sequence is based on detection of iZQCs between a solute molecule and solvent molecules that are micrometers away. The underlying evolution of the density operator has been discussed in Ref. [15]. The simplest HOMOGENIZED pulse sequence is given by $(\pi/2)_x$-GT-t_1-$(\pi/4)_x$-t_2-$(\pi)_x$ [71]. The distant dipolar field provides the necessary through-space coupling between solute and solvent spins for the detection of iZQCs. Spatial magnetization modulation created by free precession in a filed gradient *GT* can break the initial symmetry and reintroduce the dipolar field. When this field is homogenous over the separation of the solute–solvent spin pair (typically 10–100 mm) the resulting iSQCs spectrum would be just the conventional single-quantum spectrum, shifted by the chemical shift of the solvent. Hence, coupling and chemical shift information for solute molecules are retained, yet the effects of the field inhomogeneity and instability are practically eliminated. The effect of the HOMOGENIZED pulse sequence can be described by the density operator formalism [15]. The radio frequency pulse $(\pi/2)_x$ will produce MQCs when the full equilibrium density operator without the high-temperature approximation is taken into account. The applied pulse gradient GT serves as a ZQCs filter by dephasing all other coherences and leads to the effects of distant dipolar field. During evolution in the indirect dimension t_1, the solvent–solute ZQCs represented by the $I_{+i}S_{-k}$ product operator is active where *I* and *S* are spin operators for solute and solvent, respectively. These multiple-quantum coherences are modulated by the difference of the *I* and *S* Larmor frequencies shown in Fig. 28 as ω_{IS}^{SQ} and $2\omega_{IS}^{SQ}$. The ZQCs represented by $I_{+i}I_{-j}$ and $S_{+l}S_{-k}$ will not be modulated at all and correspond to the superimposed peaks at 0 ppm in the t_1 dimension (Fig. 28). The subscripts represent individual solute (i and j) and solvent (k and l) molecules. The preparation of ZQCs shown in the insert of Fig. 28 used two π/2 pulses that use phase cycling to filter out the other multiple-quantum coherences [15]. During the detection period of the experiment the (π/4) pulse transfer ZQCs into detected single-quantum two-spin anti-phase coherences such as $I_{xi}I_{zj}$, $I_{zi}S_{zk,}$ and $S_{xk}S_{zl.}$ During t_2 evolution, these terms can be rendered observable by the action of the intermolecular dipolar field which needs a time of the order of τ_d to appear [13]. This time depends on the spin equilibrium magnetization and sample shape and for a pure water sample at 300 K, τ_d is 37 ms at 25 T. The two peaks at $2\omega_{IS}^{SQ}$ and $2\omega_{SI}^{SQ}$ arise from higher-order solvent–solute ZQCs represented by four spin coherences [15]. Furthermore, the Carr-Purcell-Meiboom-Gill (CPMG) pulse sequence [189] is less sensitive to molecular diffusion that averages the distant dipolar field and can increase spectral SNR. The pulse sequence used for recording the 2D spectrum shown in Fig. 28 is therefore a combination between CPMG and HOMOGENIZED termed the CPMG-HOMOGENIZED pulse sequence (Fig. 28, insert), [188].

In conclusion, it was proved by Warren and his coworkers that, when using iZQCs, the effects of spatial inhomogeneity and temporal instability of the ultra-high magnetic field on NMR spectra are nearly eliminated, thereby achieving a resolution enhancement by a factor of about 100. This will open new frontiers in NMR spectroscopy and MR imaging. For instance, the biomolecular sizes analyzed by NMR at high magnetic fields could be dramatically extended by transverse relaxation-optimized spectroscopy (TROSY) line narrowing as discussed in Ref. [190]. Significant resolution enhancement can be generated by destructive interference between dipolar and chemical-shift-anisotropy interactions within ^{15}N-^{1}H moieties that are predicted to be nearly complete [190]. This experiment can take advantage of the inherently higher SNR at very high field using spectra generated via heteromolecular iZQCs.

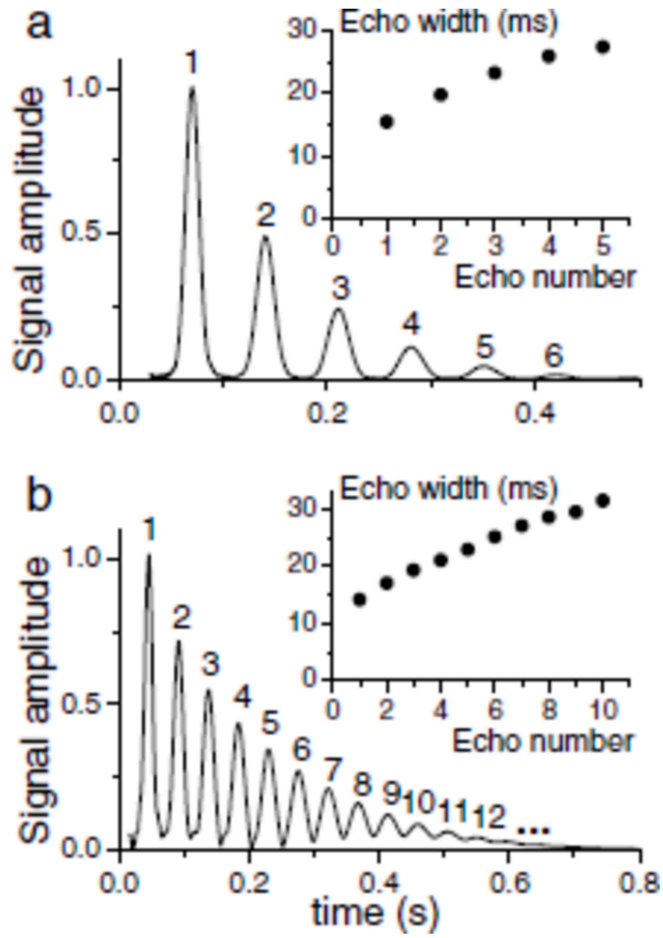

Fig. 29. Multiple spin echoes obtained with the pulse sequence similar to CRAZED using dissolved laser-polarized xenon. A series of spin echoes are observed for inter-echo times of a) $\tau = 70$ ms and b) $\tau = 45$ ms. The inserts display the corresponding echo widths. Reproduced from [212] with permission.

8. Intermolecular multiple-quantum coherences for hyperpolarized nuclei

The last few decades have seen transformative developments in techniques for hyperpolarizing nuclear spins opening new opportunities in the fields of solution NMR, solid-state NMR, and imaging [191]. The applicability of NMR spectroscopy and MR imaging even at high magnetic fields is limited by the lack of sensitivity due to the small values of nuclear magnetic moments compared to those of electrons. This situation can be overcome by creation of metastable states with high polarization (hyperpolarized nuclear states) compared to that of the spin system at thermal equilibrium. The classical methods used are based upon brute force nuclear polarization by intense magnetic fields, the nuclear Overhauser effect, or Hartmann-Hahn cross-polarization [193 and references therein].

More advanced examples of the induced hyperpolarization states are based on laser polarization of noble gases via optical pumping [192,193], dynamic nuclear polarization (DNP) via unpaired electrons [194,195], and parahydrogen-induced polarization (PHIP) [196,197]. The first method to produce hyperpolarization of nuclei was based on the transfer of angular momentum from laser photons to electron spins and finally via hyperfine interaction to nuclear spins [198,199]. State of the art methods can produce up to 70 % polarization on ^{3}He [200,201] and up to about 20 % on ^{129}Xe [202]. For noble gases the hyperpolarized magnetization continually decays towards small thermal polarization due to interatomic collisions and therefore, the temperature and pressure can largely influence the hyperpolarization state. Applications of hyperpolarized xenon in biology and the properties of ^{123}Xe in water, lipids, proteins, globins and blood has also been reviewed [203]. In the case of the DNP method a target molecule is co-mixed with an electron radical, frozen in a glass state under cryogenic conditions, and irradiated at or near the electrons microwave Larmor frequency [204,205]. DNP techniques have been used to give increases in signal-to-noise of more than 10,000 times [206]. Furthermore, coherent redistribution of polarization in parahydrogen experiments using SABRE (Signal Amplification By Reversible Exchange) – like experiments [207,208] were used for hyperpolarization of water and biomaterials [209,210] but not for measuring iMQCs induced by the distant dipolar field. One possible explanation is that, to date, methods based on p-H_2 have not produced polarization levels as large as more established methods. Warren and coworkers showed recently that the level anticrossings (LAC) strategy is responsible for this lack of SABRE efficiency [211].

The large nuclear magnetization induced by different hyperpolarization methods allows detection of intermolecular multiple-quantum coherences in liquids, in low abundance and/or low γ isotopes, and even in low density matter like gases as discussed below.

8.1. *iMQCs in hyperpolarized solids and liquids*

The generation of multiple echoes due to long-range dipolar fields has been reported using thermally polarized water or liquid ^{3}He in high magnetic fields. Based on these results multiple echoes due to distant dipolar field were investigated for hyperpolarized noble gas solutions [212]. Optically pumped spin-1/2 noble gas atoms were studied for ^{129}Xe dissolved in cyclohexane (Fig. 29) or ^{3}He dissolved in superfluid ^{4}He at T = 1.3 K.

There are several reasons for the use of this set-up since higher polarization (>30 %) than that obtained by high magnetic field or by ex situ DNPs can routinely be produced. That allow production of large average dipolar fields compared to those in bulk water in a high magnetic field. Long values for T_1 and T_2 permits several experiments with one polarization batch by slice selection. The results discussed in this study showed that the description of the spin dynamics in terms of the density matrix or mean field are equivalent at low spin temperatures as

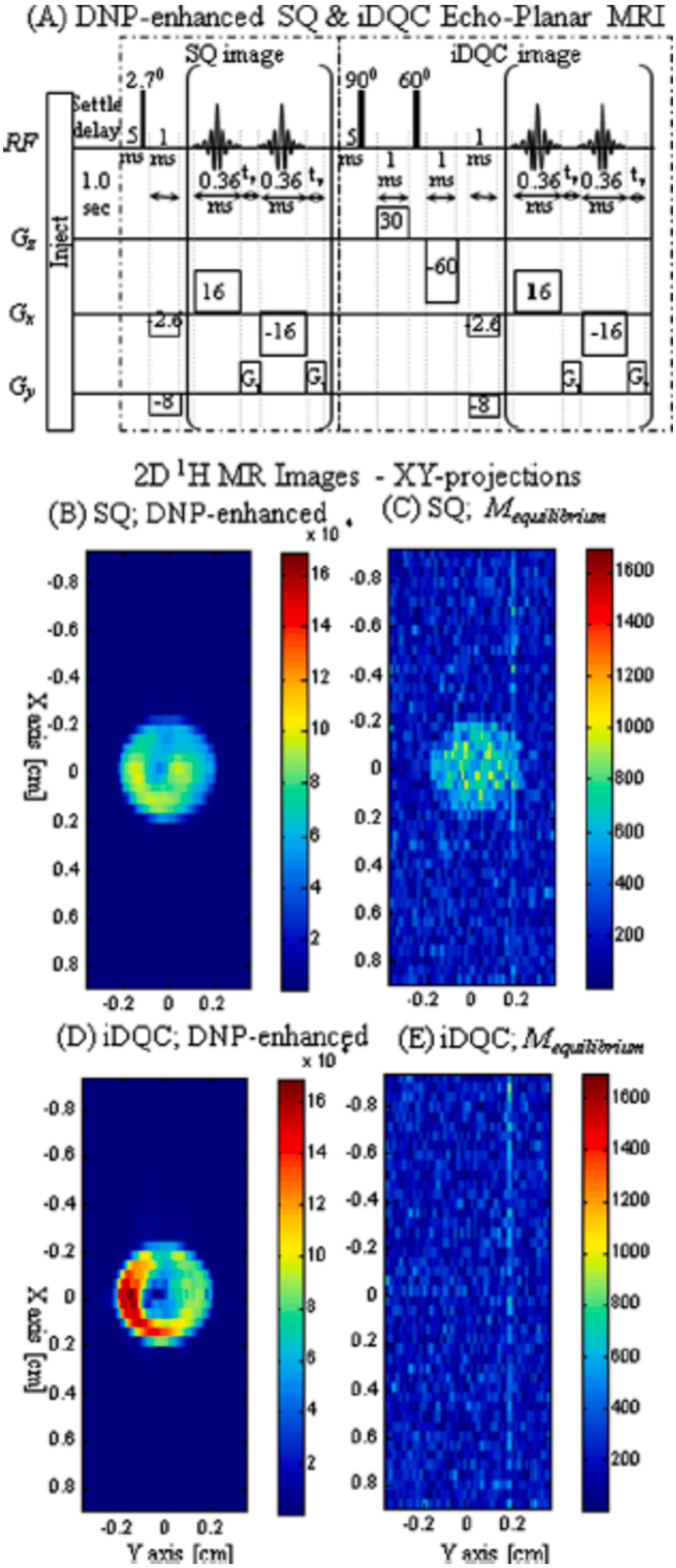

Fig. 30. Comparison between SQCs and iDQCs echo-planar NMR imaging. The parameters for the experiments are given in Ref. [214]. Images obtained from thermally polarized sample using SQCs and iDQCs methods are shown in figures C) and E). Under these conditions no iDQCs image could be discerned for a thermally polarized sample. Reproduced from [214] with permission.

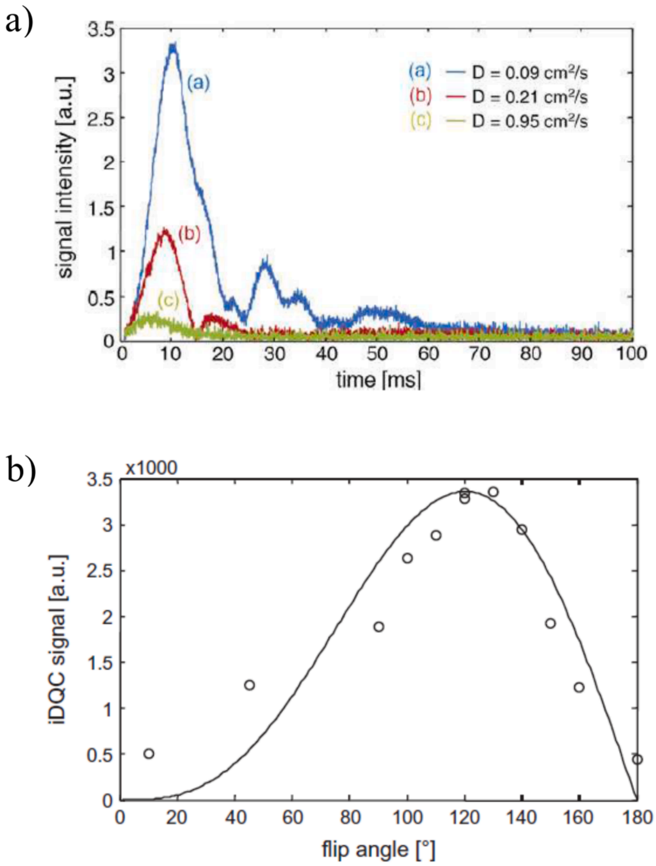

Fig. 31. A) idqcs magnitude-mode nmr signal detected in a crazed experiment of light polarized^{3}He at partial pressure of 1 bar and different partial pressure of SF$_6$. The diffusivities are given in the inset. b) Experimental data and theoretical curve of iDQCs magnitude-mode NMR signal as a function of β angle of CRAZED pulse sequence. For this experiment a gas mixture containing 1 bar ^{3}He and 6 bar SF$_6$. Adapted from [216] with permission.

10 mK for ^{129}Xe or 10 μK for ^{3}He [212].

For typical experimental conditions, well-resolved echoes are obtained (Fig. 29a) and for larger magnetization and a short echo time, up to 14 echoes have been observed (Fig. 29b). In the ideal situation i.e., an infinite medium, no diffusion, no relaxation, and uniform RF excitation pulses, the amplitude $A_{id.}^{(n)}$ of the nth echo normalized to the amplitude of the first echo is given by

$$A_{id.}^{(n)} = \frac{J_n(n\omega_{dip}\tau)}{J_1(\omega_{dip}\tau)} \tag{43}$$

where $\omega_{dip} = \mu_0\gamma M_0$ and J_n is the nth Bessel function of the first kind [212]. This result opens the way to using nonlinear multiple echoes resulting from long-range dipolar fields to determine the absolute magnetization in hyperpolarized liquids without signal calibration, and with application to quantitative imaging.

An interesting result was obtained by Warren et al. for non-proton iMQCs showing that carbon hyperpolarization in urea by ex situ DNP permits iMQCs signals to be detected with intensities comparable to those previously seen in water [213]. For low concentration thermally polarized samples of low γ nuclei such as ^{13}C, the small thermal equilibrium magnetization makes iMQCs detection nearly impossible. However, for hyperpolarized samples the dipolar demagnetization time becomes reasonably short, and in fact the signal gain can be larger for iMQCs sequences than for conventional imaging.

Based on the same approach as discussed above Frydman et al. showed that DNP endows iMQCs-based ^{1}H NMR spectra, with a sensitivity that amply exceeds that of their thermally polarized single-quantum counterpart, as confirmed by single-scan 2D imaging experiments [214]. Hyperpolarization was achieved at 1.5 K on a 50 % v/v solution of CD$_3$OH in DMSO-d_6 with free radical TEMPO. The hyperpolarized sample was transferred to an 11.7 T NMR spectrometer using CD$_3$OD as a melting/carrying solvent. Sequences employed to collect single-scan SQCs and iDQCs using EPI of the same DNA hyperpolarized solution are shown in Fig. 30 along with the pulse angles, timings and field gradients. These results can enable for instance, the observation of metabolites with intrinsically low sensitivity.

8.2. *iDQCs in hyperpolarized gases*

The high nuclear polarization of laser-polarized noble gases allows detection of long-range dipolar fields and consequently, the generation of iMQCs. To this purpose the CRAZED pulse sequence (see Section 3) was used with the second RF pulse having a flip angle of 120° for iDQCs excitation. The experiments were made on hyp-^{3}He/SF$_6$ mixture where a polarization of 60 % is routinely obtained, independent of the external magnetic field strength [215,216]. The iDQCs signal decreases with increase in diffusivity (Fig. 31a). The time of the signal maximum is given by [217],

$$t_{max} \approx 2.2/(\mu_0\gamma M_0) \tag{44}$$

For light-polarized gases $t_{\max}$ is of the order of a few ms and can be controlled by the polarization itself. A major drawback of this approach is that the spin polarization is not renewable after the action of RF pulses. This obstacle is overcome using an automated setup that permits the refilling and mixing of different gases [19]. The dependence of iDQCs signal as a function of time during the detection period of the CRAZED sequence and the RF flip angle β, are given in Fig. 31a and b, respectively. We can note that the correlation distance $d_c = \pi/\gamma GT$, for these experiments was 1.7 mm, that is about 1–2 orders of magnitude longer than typical values in liquids [218].

The large signal intensity for laser-polarized gases makes it possible to investigate the influence of rapid diffusion on the formation of the inhomogeneous spin echo in the presence of an external field gradient. This was studied for hyperpolarized ^{3}He gas at different diffusivities [219]. The fast stochastic molecular motions leads to frequency shifts of isochromats during echo formation that can be detected by a temporal shift of the echo maximum.

This effect can be attenuated in the presence of binary gas mixtures and can be varied over a considerable range by changing the molar fraction of the mixtures and the molar mass ratio of the partners [216]. The reduced diffusivity of hyperpolarized ^{3}He and ^{129}Xe in the gas mixtures allows detection of iMQCs.

9. Collective effects induced by long-range dipolar fields and radiation damping

In low polarized spin systems in the absence of long-range dipolar interactions and radiation damping the spin dynamics can be assumed to be independent of the sample magnetization and thus behave linearly. Where the magnetic field produced by the magnetized sample becomes large enough, there can be a rich behavior of spin dynamics ranging from spectral clustering, precession instabilities, amplification of weak spin precession signal, and spin turbulences. Due to these collective effects, the well-controlled distribution of transverse magnetization in the case of ideal description is not stable against small perturbations that grow exponentially as a function of time and cause turbulence of the spin dynamics. It was shown that these collective effects in spin dynamics arise from long-range dipolar interactions and radiation damping each acting alone or in combination. These complex spin behavior can possible affect the quality of magnetic resonance images made at ultrahigh magnetic fields or under hyperpolarization conditions. Non-

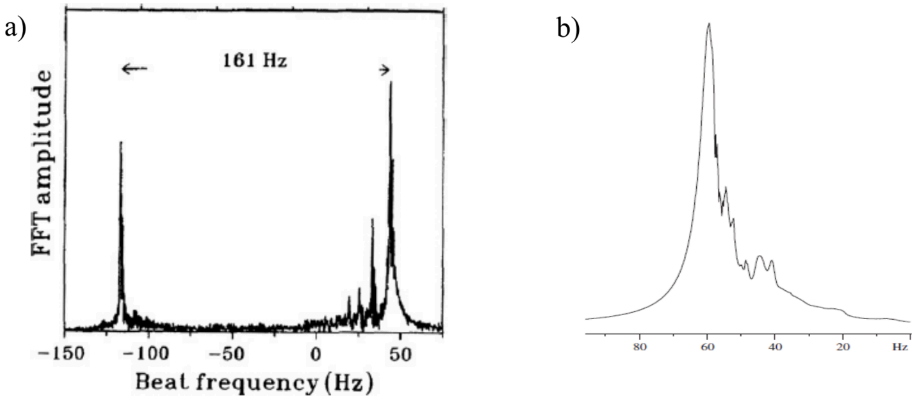

Fig. 32. (a) The highly polarized ^{3}He NMR spectrum that consists of two intense peaks due to a different orientation of liquid mixture in a U-shaped tube. This geometry will lead to different orientation of distant dipolar fields relative to static magnetic field. The other less intense peaks corresponds to spectral clustering. (b) Laser polarized ^{129}Xe spectrum with a polarization of 18% obtained using a small flip angle RF pulse of 2.5°. Adapted from [18] with permission.

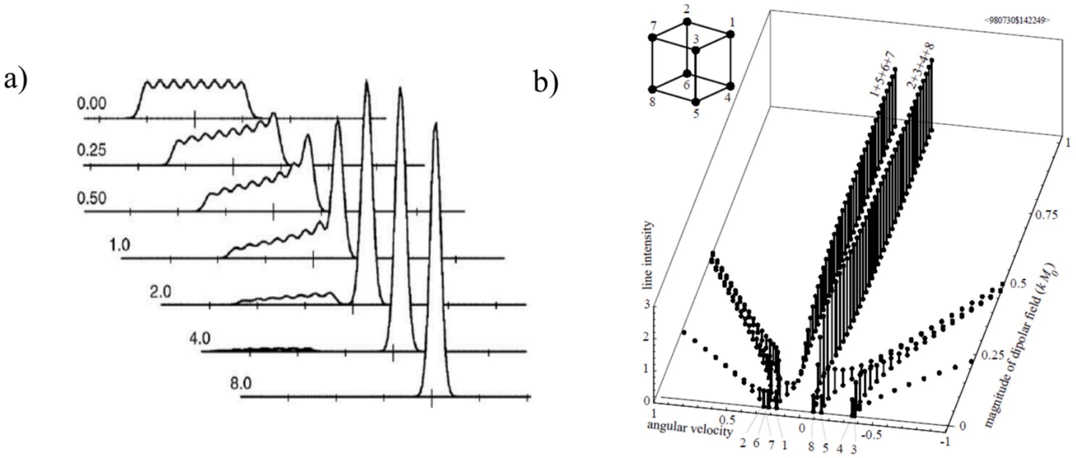

Fig. 33. a) Spectral clustering simulation for small tip angles obtained from the nonlinear Bloch equation [222]. b) An unexpected feature of the spectral clustering is the transformation of an eight-line spectrum without dipolar coupling into an essentially two-line spectrum for large dipolar coupling [221]. Adapted from [221] and [222] with permission.

linear spin effects can severely degrade radio-frequency pulse performances and hence the quality of MR images or high-resolution spectra. Furthermore, the existence of these collective effects stresses, the importance of providing control of radiation damping using simple electronic circuits. The observation of collective effects such as spin turbulence in a standard liquid NMR experiment will also require long relaxation times.

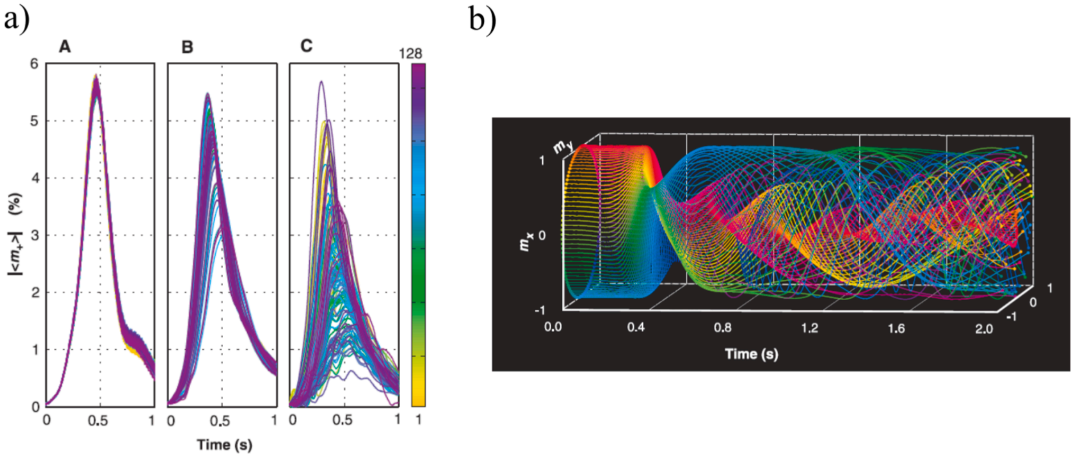

Fig. 34. Left-hand panel: superposition of free induction decays for 95 % water after the pulse sequence $(\pi/2)_x$-$(GT)_z$ with the sample temperature stabilized at (A) 25 °C, (B) 30 °C, and (C) 25 °C beginning 30 min after a magnet fill. Right-hand panel: The numerical simulation of the evolution of helix vector $m^{+}(z,t)$. Adapted from [104] with permission.

9.1. Spectral clustering

The distant dipolar fields are able to induce a distribution of spin resonance frequencies leading to coherent precessions of the different local magnetization voxels in a collective manner [18,20,220–223]. This effect was observed for the first time in a highly polarized liquid sample that consisted of a mixture of 4 % ^{3}He in ^{4}He with a ^{3}He nuclear polarization of 56 % [219]. A small angle (π/32) excitation radio-frequency pulse was applied to obtained the spectrum shown in Fig. 32a.

The existence of multiple narrow peaks is also evident in the NMR spectrum of hyperpolarized ^{129}Xe liquid using a small flip angle RF pulse as shown in Fig. 32b, [16,20,220–224]. The clustering effects were also analyzed in connection with the CRAZED method with the development of the MAXCRAZED and GRACE pulse sequences using small flip angle RF excitation [225,226].

The physics related to the spectral clustering process was discussed by Jenner [20,221,222], being related to the interplay between the distribution of resonance frequencies and the long-range dipolar field that dynamically allows the disappearance of the inhomogeneous line-broadening mechanism. This is shown in Fig. 33. The ratio of the dipolar frequency to the inhomogeneous external magnetic field is indicated on each simulated spectrum [222].

For the case of small tip angles of RF pulses the spectral clustering occurs in standard high-resolution NMR in liquids, when the maximum equilibrium of the dipolar demagnetization field is comparable to or larger than, the static magnetic field inhomogeneity over the sample. The spectral clustering was illustrated on a discrete model involving eight equal spin magnetizations at the corner of a cube, in a large external magnetic field oriented along the 1–4 direction with small inhomogeneity. Initially, the spin system is in thermal equilibrium and the response is simulated after the action of a small RF pulse. The peak intensities are plotted as a function of distant dipolar field strength. The spectral clustering effect is represented by the transformation of an eight-line spectrum without DDF into an essentially two-line spectrum for large coupling. Moreover, by increasing the tip angle, numerical simulations shown in Fig. 33b indicate that the clustering persists until spin instability sets in [221]. We can notice that the clustering and spin turbulence effects (vide infra) are classical phenomena related to spatial inhomogeneity of the macroscopic magnetization, which do not require a quantum–mechanical description for their interpretation [221].

As pointed out by Desvaux, [18] a qualitative description of spin clustering can be obtained based on the series of non-local coupled Bloch equations associated with the evolution of each local complex magnetization M_+^k of spin k, i.e.,

$$\frac{d}{dt}M_+^k = i\omega_k' M_+^k + \frac{1}{2}\sum_{l\neq k} d_{lk} M_+^l - \frac{1}{T_2} M_+^k \tag{45}$$

where ω_k' is the local resonance frequency that is related to the local average dipolar field characterized by the constant d_{lk}. The solution of the set of coupled differential equation leads to the simulated clustered spectra shown in Fig. 33. When the average dipolar frequency is larger compared to the local chemical shifts the eigenvectors of Eq. (45) become a combination of a large number of local magnetization voxels leading finally to the collective effects as shown in Fig. 33, [18].

9.2. Spin turbulence and magic sandwiches as a probe of spin instabilities

Warren et al. demonstrated experimentally and theoretically that resurrection of the crushed magnetization and the presence of spin instabilities can take place in solution NMR spectroscopy [225]. The long-range dipolar field and radiation damping can combine to generate chaotic dynamics of the spin magnetization even with the simplest pulse sequences. In many imaging and solvent suppression experiments the RF pulse/gradient scheme as $(\pi/2)_x$-$(GT)_z$ has been used, where the crusher gradient has the strength G and duration T [106 and references therein]. This spin system behavior is shown in Fig. 34a after the action of $(\pi/2)_x$-$(GT)_z$ pulse scheme. The onset of instabilities is found by numerically

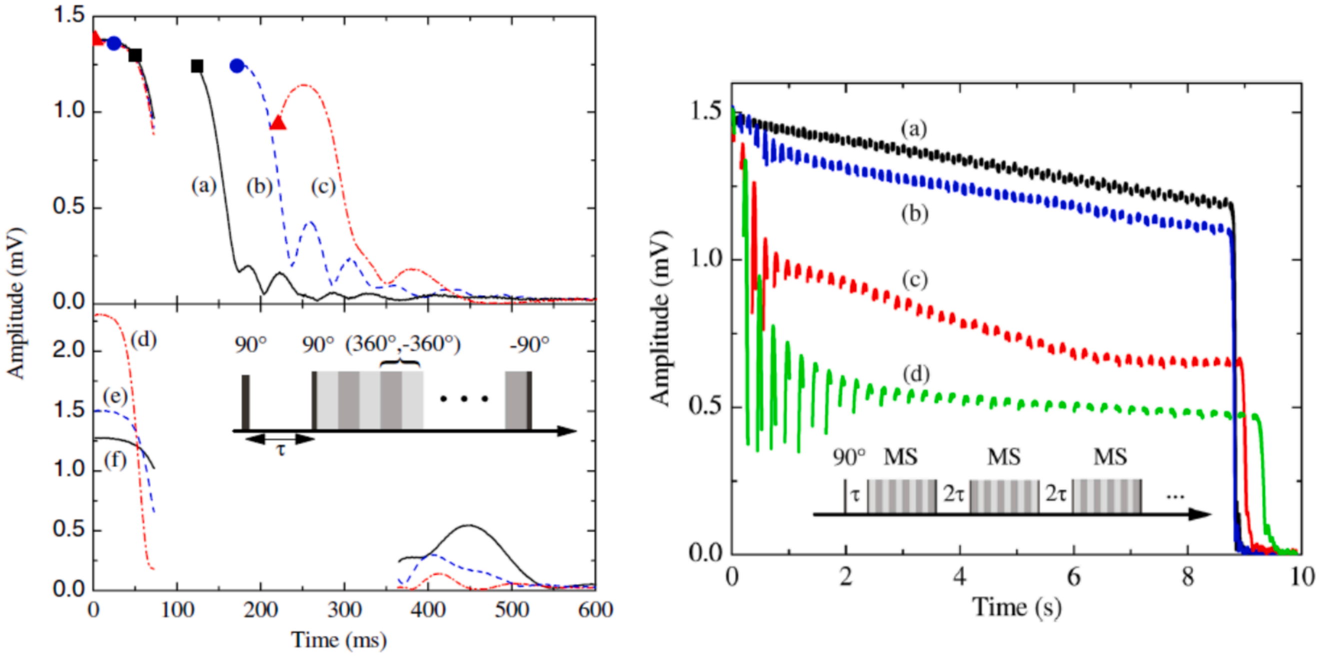

Fig. 35. Left-hand side panel: The formation of magic spin echoes for the initial time evolution of τ = 70 ms after the 90° preparation time. Magic sandwiches of various duration t are then used to progressively refocus the magnetization. The signal traces (a), (b), and (c) are detected immediately after the magic sandwich for times t = 2τ/3 (black square), t = τ/3 (blue circle) and t = 0 (red triangle). Traces (d) – (f) show the free induction decay evolution at t = -τ when the magic or mixed echo is formed. Right-hand side panel: Traces (a) to (d) correspond to magic echo trains that are observed when repeated magic sandwich (RMS) sequences with delay times t = 16, 24, 32, and 40 ms, respectively, are applied to the magnetization. The symmetries of alternating magic sandwiches are inverted to reduce phase errors. The parameters of these experiments are described in Ref. [233]. Adapted from Ref. [233] with permission. (For interpretation of the references to colour in this figure legend, the reader is referred to the web version of this article.)

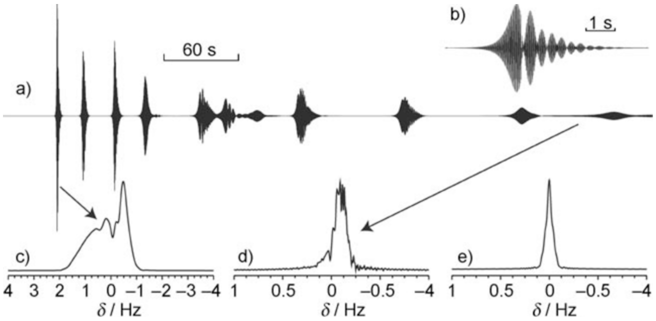

Fig. 36. Spontaneous emission of optically polarized ^{129}Xe (polarization of 27 %) with a negative Boltzmann temperature. a) Free induction decay of ^{129}Xe with a duration of 8.5 min. b) The FID structure for the first NMR maser beat showing the presence of distant dipolar field. c) to e) show the Fourier transform of the partial FIDs indicated by arrows. The narrower linewidth (about 0.034 Hz) of the NMR spectrum in e) is resulting from the decrease in the average dipolar field due to decay of spin polarization. Reproduced from [235] with permission.

integrating the Bloch equations without relaxation and diffusion effects (Fig. 34b). Moreover, for a spin concentrated sample or in the presence of hyperpolarization as well as at ultrahigh magnetic fields the partially canceled magnetization is amplified by a large factor 10^2-10^4 (resurrection) before it decays away. The essential role played by the distant dipolar field in the process of spin turbulence was proved by detecting an NMR signal with a magic-angle gradient that makes the distant dipolar field very small. In this situation the resurrected signal detected after the gradient is almost cancelled [104].

NMR time-reversal pulse sequences based on magic and mixed spin echoes acting in the presence of homonuclear and heteronuclear dipolar coupled spin network [227–232], prove to be efficient tools to manipulate the long-range dipolar interaction present in the spin system with strong magnetization induced by hyperpolarization [233]. This NMR approach was applied for many-body dipolar coupled nuclei in solids showing that it is possible to generate MR images of residual dipolar couplings [230–232]. Furthermore, the possibility of generating magic and mixed spin echoes was proven for spin systems in liquids [233]. This sheds light on the deleterious effects of spin turbulence that can be controlled or suppressed.

The reported experiments where performed on dilute non-degenerate mixtures of hyperpolarized ^{3}He (typically $\leq$ 40%) in liquid ^{4}He at temperature of about 1 K, and a magnetic field flux density of 2.3 mT [233]. The time reversal pulse sequence was applied at the ^{3}He resonance frequency. The experimental results shown in Fig. 35 can be interpreted by taking into account that (i) the radio-frequency field of the magic sandwich (see Ref. [227]) must be larger than the long-range dipolar field, and (ii) during the action of the magic sandwich the value of long-range dipolar coupling is scaled by a factor of $-1/2$.

The most important feature of the results shown in Fig. 35 (left-hand side panel) is that large NMR signals are detected long after the net transverse magnetization normally would have averaged to zero. The evolution of magnetization after the action of magic sandwich trains of different duration are shown in Fig. 35 (right-hand side panel). In this case two distinct signal behaviors were detected [233]. In the initial period, the imperfect refocusing dominates. In the second phase magnetization losses continue to be incurred, but at significantly lower rates. The apparent lifetimes of these dynamically sustained precession signals are in some cases more than three orders of magnitude longer than the characteristic coherence time decay of the freely evolving nuclear magnetization.

The results discussed above have demonstrated the existence of magic echoes and spin echoes trains in highly polarized liquid samples that are dominated by nonlinear and nonlocal, long-range dipolar interactions. Repeated magic sandwich pulse sequence can be used to dynamically stabilize modes of nuclear precession that are otherwise intrinsically unstable. Hence, the effective precession lifetimes of nuclear magnetization was prolonged [233]. Moreover, the competition between nonlinear spin dynamics and spin diffusion can explain the experimental results. The approach based on mixed echoes [232,233] gives information about the control of spin instabilities.

9.3. Collective effects in a hyperpolarized NMR maser

In a series of papers some new and old established collective effects were reported [228–237]. When the magnetization of dissolved hyperpolarized ^{129}Xe is intense and prepared in a state with an inverted Boltzmann population the spin system spontaneously emits a series of random radio-frequency bursts characterized by a very narrow bandwidth without RF pulse excitation (Fig. 36) [235–237]. The characteristic of this chaotic NMR-maser can be explained in the framework of non-linear Bloch equations that takes into account the inhomogeneous spatial organization of the ^{129}Xe magnetization, and which can be described by the distant dipolar field corroborated with radiation damping. The detection of spectral clustering in laser-polarized ^{129}Xe with inverse Boltzmann spin distribution indicates the presence of distant dipolar couplings [235].

^{129}Xe multiple spontaneous NMR maser emissions are shown in Fig. 36 [235]. The Fourier transform of the free induction decay for a particular burst reveals the existence of a superposition of frequencies in each burst. This effect is detected without any renewal of the xenon magnetization inside the detection region by macroscopic transport mechanisms.

Furthermore, this can be correlated with the presence of the distant dipolar field that decays in strength due to reduction of negative longitudinal magnetization during the multiple RF emissions. The interplay between spin system dynamics, radiation damping and long-range dipolar field was proved using numerical simulations [237]. These simulations are based on non-linear Maxell – Bloch differential equations that prove that observed random amplitude modulations require long-distance dipolar couplings between nuclear spins with the feedback field acting as an amplifier. Due to this process the magnetization is largely tilted off the longitudinal axis, as an apparent transverse self-relaxation which destroys coherence. It is suggested that this mechanism explains why the final magnetization after emission can still be in the opposite direction to the magnetic field [237].

The effects of the long-range dipolar field in combination with radiation damping in a solid-state NMR maser pumped by dynamic nuclear polarization (DNP) was reported by Abergel and coworkers [238,239]. The nuclear spins represented by fully protonated compounds like H_2O were efficiently polarized by TEMPOL having a broad EPR line typical of nitroxides. The DNP experiments were performed at a temperature of about 1.27 K, and the microwave frequency was set so as to negatively polarize nuclear spin. The buildup time was set to 40 min after which the acquisition started typically lasting for tens of thousands of seconds. This leads to multiple ^{1}H maser burst, triggered by noise or an RF pulse [239]. Sustained maser bursts upon continuous microwave irradiation obtained as a pseudo-2D experiment on solid paramagnetically doped water similar with those shown in Fig. 36 was also reported [239]. A theoretical model was proposed for the collective dynamics of a spin ensemble subject to the combination of radiation feedback from the NMR probe, long-range dipolar field, and DNP in the thermal mixing regime. The dynamics of the spin system are non-local and nonlinear being described semi-quantitatively by modified Bloch-Maxwell equations. Numerical simulations based on these equations allow the complex time evolution of the total nuclear magnetization to be studied. These partially explain the experimental results due to a large number of parameters and time scales that include the shape of the sample and the spin density [239]. The effect of the distant dipolar field is revealed in the magnetization time evolution and can be explained by the presence of efficient radiation feedback that leads to a persistent coherence on the time scales of minutes.

10. Conclusions and outlook

This review discusses the basic foundation of nonlinear NMR revealed in solid, liquid, and gaseous samples by dedicated experiments such as multiple spin echoes and intermolecular multiple quantum coherences 2D spectroscopy. The high harmonic resonances which are signature of iMQCs have triggered extensive theoretical and experimental activity. This resulted in exciting novel applications in magnetic resonance 2D spectroscopy under spatially localized conditions, magnetic resonance imaging, and magnetic resonance thermometry. These spin non-linear effects can severely deteriorate radio-frequency pulse performances and hence the quality of MR images or high-resolution spectra especially at ultrahigh magnetic field or under hyperpolarization conditions.

Recently MRI at low magnetic fields (0.05–1 T) has becomes an active field of investigation [240–244], and hence it is of interest to analyze whether intermolecular multiple-quantum coherences can be excited with enough efficiency at such fields. To this purpose, the contribution of high-order terms in the density operator at thermal equilibrium at two magnetic flux densities of $B_{0,low} = 0.05$ T and $B_{0,high} = 7$ T should be compared. The terms of the density operator expansion related to the bilinear spin operators have a relative factor proportional to $(B_{0,low}/B_{0,high})^2$, leading to cross peaks in a CRAZED-like experiment at low field about 10^{-4} times smaller compared to the that measured at high field. Moreover, a reduction in the strength of the dipolar demagnetization field will take place with negative consequences on the amplitude of nonlinear spin echoes and the intensities of cross-peaks. For water at room temperature, in a magnetic field corresponding to a proton Larmor frequency of 600 MHz, the demagnetization field shift for protons in a cylindrical sample was estimated to be -0.8 Hz [22], but the shift of $-2\text{x}10^{-3}$ Hz at 0.05 T is very low. For experiments made at low magnetic fields M_0 is smaller and therefore, the dipolar demagnetization time becomes longer reducing the intensity of cross-peaks generated by the CRAZED pulse sequence. Hence, MRI and MRS using iMQCs are unlikely to be achievable at low magnetic fields without applying efficient hyperpolarization methods.

CRediT authorship contribution statement

Dan Eugen Demco: Writing – review & editing, Writing – original draft, Investigation, Conceptualization. **Ana-Maria Oros-Peusquens:** Writing – review & editing, Validation, Resources, Conceptualization. **Nadim Jon Shah:** Writing – review & editing, Validation, Supervision, Resources, Conceptualization.

Declaration of competing interest

The authors declare that they have no known competing financial interests or personal relationships that could have appeared to influence the work reported in this paper.

Acknowledgements

This work was funded in part by Forschungszentrum-Jülich, INM-4, Germany, under the contract 42333242. D.E.D. gratefully acknowledge the support of Prof. Andreas Herrmann and Prof. Andrij Pich at DWI-Leibniz, RWTH-Aachen. The authors acknowledge useful discussions with Prof. Daniel David, Prof. Simion Simon, Prof. Radu Fechete and Dr. Ruben Nechifor from INSPIRE platform of University Babes-Bolyai.

Data availability

No data was used for the research described in the article.

References

[1] F. Bloch, W.W. Hansen, M.E. Packard, Nuclear induction, PhysRev. 69 (1946) 127, https://doi.org/10.1103/PhysRev.69.127.

[2] E.M. Purcell, H.C. Torrey, R.V. Pound, PhysRev. 69 (1946) 37–38, https://doi.org/10.1103/PhysRev.69.37.

[3] R.R. Ernst, G. Bodenhausen, A. Wokaun, Principles of nuclear magnetic resonance in one and two dimensions, Clarendon Press, Oxford, 1987.

[4] A. Abragam, The principles of nuclear magnetism, Oxford University Press, 1961.

[5] G. Bodenhausen, Multiple-quantum NMR, Prog. Nucl. Magn. Reson. Spec. 14 (1980) 137–173, https://doi.org/10.1016/0079-6565(80)80007-0.

[6] M. Munowitz, A. Pines, Principles and applications of multiple-quantum NMR, Adv. Chem. Phys. 66 (1987) 2–152, https://doi.org/10.1002/9780470142929.ch1.

[7] O.W. Sorensen, G.W. Eich, M.H. Levitt, G. Bodenhausen, R.R. Ernst, Product operator formalism for the description of NMR pulse experiments, Progress Nucl. Magn. Reson. Spec. 16 (1983) 163–192, https://doi.org/10.1016/0079-6565(84)80005-9.

[8] M. Goldman, Quantum description of high-resolution NMR in liquids, Oxford University Press, 1988.

[9] R. Kimmich, NMR tomography, diffusometry, relaxometry, Springer, Berlin, 1997.

[10] P. Mansfield, P.G. Morris, NMR imaging in biomedicine, Academic Press, New York, 1982.

[11] D. Deville, M. Bernier, J.M. Delrieux, NMR multiple echoes observed in solid ^{3}He, PhysRevB 19 (1979), https://doi.org/10.1103/PhysRevB.19.5666.

[12] R. Bowtell, R.M. Bowley, P. Glover, Multiple spin echoes in liquids in a high magnetic field, J. Magn. Reson. 88 (1990) 643–651, https://doi.org/10.1016/0022-2364(90)90297-M.

[13] W.S. Warren, W.A. Richter, H. Andreotti, B.T. Farmer II, Generation of impossible cross-peaks between bulk water and biomolecules in solution NMR, Science 262 (1993) 2005–2009, https://doi.org/10.1126/science.8266096.

[14] Q. He, W. Richter, S. Vathyam, W.S. Warren, Intermolecular multiple quantum coherences and cross correlations in solution nuclear magnetic resonance, J. Chem. Phys. 98 (1993) 6779–6800, https://doi.org/10.1063/1.464770.

[15] S. Lee, W. Richter, S. Vathyam, W.S. Warren, Quantum treatment of the effects of dipole-dipole interactions in solution nuclear magnetic resonance, J. Chem. Phys. 105 (1996) 874–900, https://doi.org/10.1063/1.471968.

[16] W. Richter, W.S. Warren, Intermolecular multiple quantum coherences in liquids, Concepts Magn. Reson. 12 (2000) 396–409, https://doi.org/10.1002/1099-0534(2000)12:6<396::AID-CMR3>3.0.CO;2-Y.

[17] E.D. Minot, P.T. Callaghan, N. Kaplan, Multiple echoes, multiple quantum coherence and the dipolar field: demonstrating the significance of high order terms in the equilibrium density matrix, J. Magn. Reson. 140 (1999) 200–205, https://doi.org/10.1006/jmre.1999.1793.

[18] H. Desvaux, Non-linear liquid-state NMR, Prog. Nucl. Magn. Reson. Spec. 70 (2013) 50–71, https://doi.org/10.1016/j.pnmrs.2012.11.001.

[19] R.H. Acosta, L. Agulles-Pedrós, S. Komin, D. Sebastiani, H.-W. Spiess, P. Blümler, Diffusion in binary gas mixtures studied by NMR of hyperpolarized gases and molecular dynamics simulations, Phys. Chem. Chem. Phys. 8 (2006) 4182–4188, https://doi.org/10.1039/b609316g.

[20] J. Jenner, Dynamical instabilities in liquid nuclear magnetic resonance with large nuclear magnetization with and without pulsed field gradients, J. Chem. Phys. 116 (2002) 8439–8446, https://doi.org/10.1063/1.1469020.

[21] J. Jeener, Equivalence between the "classical" and the "Warren" approaches for the effects of long range dipolar couplings in liquid nuclear magnetic resonance, J. Chem. Phys. 112 (2000) 5091–5094, https://doi.org/10.1063/1.481063.

[22] M.H. Levitt, Demagnetization effects in two-dimensional solution NMR, Concepts Magn. Reson. 8 (1996) 77–103, https://doi.org/10.1002/(SICI)1099-0534(1996)8:2<77::AID-CMR1>3.0.CO;2-L.

[23] B.I. Bleaney, B. Bleaney, Electricity and Magnetism, Oxford University Press, Oxford, 1967.

[24] D. Einzel, G. Eska, Y. Hirayoshi, T. Kopp, P. Wölfle, Multiple spin echoes in a normal Fermi liquid, PhysRevLett. 53 (1984) 2312–2315, https://doi.org/10.1103/PhysRevLett.53.2312.

[25] H. Körber, E. Dormann, G. Eska, Multiple spin echoes for protons in water, J. Magn. Reson. 93 (1991) 589–595, https://doi.org/10.1016/0022-2364(91)90085-8.

[26] H.T. Edzes, The nuclear magnetization as the origin of transient changes in the magnetic field in pulsed NMR experiments, J. Magn. Reson. 86 (1990) 293–303, https://doi.org/10.1016/0022-2364(90)90261-7.

[27] W.S. Warren, S. Lee, W. Richter, S. Vathyam, Correcting the classical dipolar demagnetization field in solution NMR, Chem. Phys. Lett. 247 (1995) 207–214, https://doi.org/10.1016/0009-2614(95)01184-5.

[28] M.A. McCoy, F. Loaiza, K. Valentine, W.S. Warren, Self-refocused solvent suppression with shaped pulses, J. Magn. Reson. 80 (1988) 155–161, https://doi.org/10.1016/0022-2364(88)90069-8.

[29] T. Enss, S. Ahn, W.S. Warren, Visualization the dipolar field in solution NMR and MR imaging: three-dimensional structure simulation, Chem. Phys. Lett. 305 (1999) 101–108, https://doi.org/10.1016/S0009-2614(99)00366-8.

[30] J. Jeener, A. Vlassenbroek, P. Broekaert, Unified derivation of the dipolar field and relaxation terms in the Block-Redfield equations of liquid NMR, J. Chem. Phys. 103 (1995) 1309–1332, https://doi.org/10.1063/1.469809.

[31] N. Bloembergen, R.V. Pound, Radiation damping in magnetic resonance experiments, PhysRev. 95 (1954) 8–12, https://doi.org/10.1103/PhysRev.95.8.

[32] S. Bloom, Effects of radiation damping on spin dynamics, J. Appl. Phys. 28 (1957) 800–8005, https://doi.org/10.1063/1.1722859.

[33] A. Vlaassenbroek, J. Jeener, P. Broekaert, Radiation damping in high resolution liquid NMR: A simulation study, J. Chem. Phys. 103 (1995) 5886–5897, https://doi.org/10.1063/1.470468.

[34] W.S. Warren, S.L. Hammes, J.L. Bates, Dynamics of radiation damping in nuclear magnetic resonance, J. Chem. Phys. 91 (1989) 5895–5904, https://doi.org/10.1063/1.457458.

[35] X. -an Mao, J. -xin Guo, C.-hui Ye, Nuclear-magnetic-resonance line-shape theory in the presence of radiation damping, PhysRevB 49 (1994) 15702–15711, https://doi.org/10.1103/PhysRevB.49.15702.

[36] D. Abergel, M.A. Delsuc, J.-Y. Lallemand, Comment on: Is multiple quantum nuclear magnetic resonance spectroscopy of liquid water real? J. Chem. Phys. 96 (1992) 1657–1658, https://doi.org/10.1063/1.462155.

[37] S. Ahn, S. Lee, W.S. Warren, The competition between intramolecular J coupling, radiation damping, and intermolecular dipolar couplings in two-dimensional solution nuclear magnetic resonance, Molec. Phys. 95 (1998) 769–785, https://doi.org/10.1080/002689798166404.

[38] P. Broekaert, J. Jenner, Suppression of radiation damping in NMR in liquids by active electronic feedback, J. Magn. Reson. A 113 (1995) 60–64, https://doi.org/10.1006/jmra.1995.1056.

[39] E. Hahn, Spin echoes, PhysRev. 80 (1950) 580–594, https://doi.org/10.1103/PhysRev.80.580.

[40] F.M. Alessandri, S. Capuani, B. Maraviglia, Multiple spin echoes in heterogeneous systems: physica origins of the observed dips, J. Magn. Reson. 156 (2002) 72–78, https://doi.org/10.1006/jmre.2002.2543.

[41] I. Ardelean, E. Kossel, R. Kimmich, Attenuation of homo- and heteronuclear multiple spin echoes by diffusion, J. Chem. Phys. 114 (2001) 8520–8529, https://doi.org/10.1063/1.1365111.

[42] E. Kossel, R. Kimmich, I. Ardelean, The influence of J-coupling on heteronuclear nonlinear (or multiple) spin echoes, Chem. Phys. Lett. 347 (2001) 157–162, https://doi.org/10.1016/S0009-2614(01)01007-7.

[43] R. Bowtell, Indirect detection via the dipolar demagnetization field, J. Magn Reson 100 (1992) 1–17, https://doi.org/10.1016/0022-2364(92)90361-A.

[44] J.C. Waterton, R.P. Jones, G.A. Morris, A spatial editing of NMR spectra by use of heteronuclear multiple spin echoes, J. Magn. Reson. 97 (1992) 218–221, https://doi.org/10.1016/0022-2364(92)90253-4.

[45] R. Kimmich, I. Ardelean, Intermolecular multiple-quantum coherence transfer echoes and multiple echoes in nuclear magnetic resonance, J. Chem. Phys. 110 (1999) 3708–3713, https://doi.org/10.1063/1.478261.

[46] I. Ardelean, R. Kimmich, Diffusion measurements with the pulsed gradient nonlinear spin echo method, J. Chem. Phys. 112 (2000) 5275–5280, https://doi.org/10.1063/1.481123.

[47] I. Ardelean, S. Stapf, D.E. Demco, R. Kimmich, The nonlinear stimulated echo, J. Magn. Reson. 124 (1997) 506–508, https://doi.org/10.1006/jmre.1996.1081.

[48] I. Ardelean, R. Kimmich, S. Stapf, D.E. Demco, Multiple nonlinear stimulated echo, J. Magn. Reson. 127 (1997) 217–224, https://doi.org/10.1006/jmre.1997.1197.

[49] I. Ardelean, R. Kimmich, Diffusion measurements using nonlinear stimulated echo, J. Magn. Reson. 143 (2000) 101–105, https://doi.org/10.1006/jmre.1999.1975.

[50] I. Solomon, Rotary spin echoes, PhysRevLett. 2 (1959) 301–302, https://doi.org/10.1103/PhysRevLett.2.301.

[51] D. Canet, Radiofrequency field gradient experiments, Prog. NMR Spectrosc. 30 (1997) 101–135, https://doi.org/10.1016/S0079-6565(96)01031-X.

[52] G.S. Karczmar, D.B. Twieg, T.J. Lawry, G.B. Matson, M.W. Weiner, Detection of motion using B_1 gradients, Magn. Reson. Med. 7 (1988) 111–116, https://doi.org/10.1002/mrm.1910070113.

[53] D. Canet, B. Diter, A. Belmajdoub, J. Brondeau, J.C. Boubel, K. Elbayed, Self diffusion measurements using a radiofrequency field gradient, J. Magn. Reson. 81 (1989) 1–12, https://doi.org/10.1016/0022-2364(89)90263-1.

[54] R. Dupeyre, P.H. Devoulon, D. Bourgeois, M. Decorps, Diffusion measurements using stimulated rotary echoes, J. Magn. Reson. 95 (1991) 589–596, https://doi.org/10.1016/0022-2364(91)90174-R.

[55] R. Kimmich, B. Simon, H. Köstler, Magnetization-grid rotating-frame technique for diffusion and flow measurements, J. Magn. Reson. A 112 (1995) 7–12, https://doi.org/10.1006/jmra.1995.1002.

[56] F. Humbert, M. Valtier, A. Retournard, D. Canet, Diffusion measurements using radiofrequency field gradients: artifacts, remedies, practical hints, J. Magn. Reson. 134 (1998) 245–254, https://doi.org/10.1006/jmre.1998.1541.

[57] D.I. Hoult, Rotating frame zeugmatography, J. Magn. Reson. 33 (1979) 183–197, https://doi.org/10.1016/0022-2364(79)90202-6.

[58] F. Humbert, B. Diter, D. Canet, NMR microscopy by strong radiofrequency-field gradients with spatial resolution better than five micrometers, J. Magn. Reson. A 123 (1996) 242–245, https://doi.org/10.1006/jmra.1996.0245.

[59] R. Kimmich, I. Ardelean, Y.-Y. Lin, S. Ahn, W.S. Warren, Multiple spin echo generation by gradients of the radio frequency amplitude. Two-dimensional nutation spectroscopy and multiple rotary echoes, J. Chem. Phys. 111 (1999) 6501–6509, https://doi.org/10.1063/1.480026.

[60] I. Ardelean, A. Scharfenecker, R. Kimmich, Two-pulse nutation echoes. generated by gradients of the radiofrequency amplitude and the main magnetic field, J. Magn. Reson. 144 (2000) 45–52, https://doi.org/10.1006/jmre.2000.2017.

[61] S. Ahn, S. Lee, W.S. Warren, The competition between intramolecular J couplings, radiation damping, and intermolecular dipolar couplings in two-dimensional nuclear magnetic resonance, Molec. Phys. 95 (1998) 769–785, https://doi.org/10.1080/002689798166404.

[62] R.T. Branca, S. Capuani, B. Maraviglia, About the Crazed sequence, Concepts Magn. Reson. 21 (2004) 22–36, https://doi.org/10.1002/cmr.a.20001.

[63] C. Ramanathan, R. Bowtell, Dynamics of the nuclear magnetic resonance COSY-revamped by asymmetric z-gradients (CRAZED) experiment, J. Chem. Phys. 114 (2001) 10854–10859, https://doi.org/10.1063/1.1375026.

[64] C.K. Wong, J. Zhong, Roles of magnetic gradient field and transverse relaxation in distant field signal, Concepts Magn. Reson. 34A (2009) 76–90, https://doi.org/10.1002/cmr.a.20135.

[65] M. Schneider, L. Gasper, D.E. Demco, B. Blümich, Residual dipolar couplings by ^{1}H dipolar-encoded longitudinal magnetization, double- and triple-quantum nuclear magnetic resonance in cross-linked elastomers, J. Chem. Phys. 111 (1999) 402–415, https://doi.org/10.1063/1.479291.

[66] K. Saalwächter, Proton multiple-quantum NMR for the study of chain dynamics and structural constraints in polymeric soft materials, Progress Nucl. Magn. Reson. Spec. 51 (2007) 1–35, https://doi.org/10.1016/j.pnmrs.2007.01.001.

[67] W.P. Aue, E. Bartholdi, R. r., Ernst, Two-dimensional spectroscopy. Application to nuclear magnetic resonance, J. Chem. Phys. 64 (1976) 2229–2246, https://doi.org/10.1063/1.432450.

[68] U. Piantini, O.W. Sorensen, R.R. Ernst, Multiple quantum filters for elucidating NMR coupling networks, J. Am. Chem. Soc. 104 (1982) 6800–6801, https://doi.org/10.1021/ja00388a062.

[69] A.J. Shaka, R. Freeman, Simplification of NMR spectra by filtration through multiple-quantum coherence, J. Magn. Reson. 51 (1983) 169–173, https://doi.org/10.1016/0022-2364(83)90117-8.

[70] S. Vathyam, S. Lee, W.W. Warren, Homogeneous NMR spectra in inhomogeneous fields, Science 272 (1996) 92–96, https://doi.org/10.1126/science.272.5258.92.

[71] W.W. Warren, S. Ahn, M. Mescher, M. Garwood, K. Ugurbil, W. Richter, R.R. Rizi, J. Hopkins, J.S. Leigh, MR imaging contrast enhancement based on intermolecular zero quantum, Science 281 (1998) 247–251, https://doi.org/10.1126/science.281.5374.247.

[72] J. Zhong, Z. Chen, E. Kwok, In vivo intermolecular double-quantum imaging on a clinical 1.5 T MR scanner, Magn. Reson. Med. 43 (2000) 335–341, https://doi.org/10.1002/(SICI)1522-2594(200003)43:3<335::AID-MRM3>3.0.CO;2-1.

[73] Z. Chen, Z.W. Chen, J. Zhong, Quantitative characterization of intermolecular dipolar interactions of two-component systems in solution nuclear magnetic resonance, J. Chem. Phys. 115 (2001) 10769–10779, https://doi.org/10.1063/1.1417503.

[74] Z. Chen, Z. Chen, J. Zhong, High-resolution NMR spectra in inhomogeneous fields via IDEAL (Intermolecular dipolar-interaction enhanced all lines) method, J. Am. Chem. Soc. 128 (2004) 446–447, https://doi.org/10.1021/ja036491f.

[75] Z. Chen, S. Zheng, J. Zhong, Optimal RF flip angles for multiple spin-echoes and iMQCs of different order with CRAZED pulse sequence, Chem. Phys. Lett. 347 (2001) 143–148, https://doi.org/10.1016/S0009-2614(01)01042-9.

[76] X. Zhu, Z. Chen, S. Cai, J. Zhong, Formation and identification of pure intermolecular zero-quantum coherence signal in liquid NMR, Chem. Phys. Lett. 421 (2006) 171–178, https://doi.org/10.1016/j.cplett.2006.01.041.

[77] Z. Chen, Z. Chen, S.J. Zhong, Observation and characterization of intermolecular homonuclear single-qauntum coherences in liquid nuclear magnetic resonance, J. Chem. Phys. 117 (2002) 8426–8435, https://doi.org/10.1063/1.1512649.

[78] P.R. Bachiller, S. Ahn, W.S. Warren, Detection of intermolecular heteronuclear multiple-quantum coherences in solution NMR, J. Magn. Reson. A 122 (1996) 94–99, https://doi.org/10.1006/jmra.1996.0183.

[79] S. Ahn, W.S. Warren, S. Lee, Quantum treatment of intermolecular multiple-qauntum coherences with intramolecular J coupling in solution NMR, J. Magn. Reson. 128 (1997) 114–119, https://doi.org/10.1006/jmre.1997.1226.

[80] S. Ahn, N. Lisitza, W.S. Warren, Intermolecular zero-quantum coherences of multi-component spin systems in solution NMR, J. Magn. Reson. 133 (1998) 266–272, https://doi.org/10.1006/jmre.1998.1461.

[81] B. Jiang, H. Liu, M. Liu, G. Ye, X.-an Mao, Multiple –quantum correlated spectroscopy revamped by asymmetric *z*-gradient echo detection signal intensity as a function of the read pulse flip angle as verified by heteronuclear ^{1}H/^{31}P experiments, J. Chem. Phys. 126 (2007) 054502, https://doi.org/10.1063/1.2429657.

[82] C. Arús, M. Bárány, W.M. Westler, J.L. Markley, ^{1}H NMR of intact tissues at 11.1T, J. Magn. Reson. 57 (1984) 519–525, https://doi.org/10.1016/0022-2364(84)90269-5.

[83] C. Arús, Y.-C. Chang, M. Bárány, Proton nuclear magnetic resonance of excised rat brain. Assignments of resonances, Physiol. Chem. Phys. Med. 17 (1985) 23–33. PMID: 4034678.

[84] V. Govindaraju, K. Young, A.A. Maudsley, Proton NMR chemical shifts and coupling constants for brain metabolites, NMR Biomed. 13 (2000) 129–153, https://doi.org/10.1002/1099-1492(200005)13:3<129::aid-nbm619>3.0.co;2-v.

[85] W. Chen, X.-H. Zhu, Dynamic study of cerebral bioenergetic and brain function using in vivo multinuclear MRS approaches, Conc. Magn. Reson. 27A (2005) 84–121, https://doi.org/10.1002/cmr.a.20046.

[86] R.A. Wevers, U. Engelke, A. Heerschap, High-resolution ^{1}H-NMR spectroscopy of blood plasma for metabolic studies, Clin. Chem. 40 (1994) 1245–1250, https://doi.org/10.1093/clinchem/40.7.1245.

[87] R.A. Wevers, U. Engelke, U. Wendel, J.G. de Jong, F.J. Gabreels, A. Heerschap, Standardized method for high-resolution ^{1}H-NMR of cerebrospinal fluid, Clin. Chem. 41 (1995) 744–751, https://doi.org/10.1093/clinchem/41.5.744.

[88] K. Young, B.J. Soher, A.A. Maudsley, Automated spectral analysis II: application of wavelet shrinkage for characterization of non-parametrized signals, Magn. Reson. Med. 40 (1998) 816–821, https://doi.org/10.1002/mrm.1910400606.

[89] D.Z. Balla, C. Faber, Localized intermolecular zero-quantum coherence spectroscopy in vivo, Conc. Magn. Reson. 32A (2007) 117–121133, https://doi.org/10.1002/cmr.a.20104.

[90] K. Wüthrich, NMR of proteins and nucleic acids, John Wiley & Sons, 1986.

[91] J.R. Garbow, D.P. Weitekamp, A. Pines, Total spin coherence transfer echo spectroscopy, J. Chem. Phys. 79 (1983) 5301–5310, https://doi.org/10.1063/1.445692.

[92] Z. Chen, Z.W. Chen, D.W. Hwang, J.H. Zhong, L.P. Hwang, Separation and characterization of different signals from intermolecular three-spin orders in solution NMR, J. Magn. Reson. 171 (2004) 244–252, https://doi.org/10.1016/j.jmr.2004.08.023.

[93] Z. Chen, T. Hou, Z.W. Chen, D.W. Hwang, L.P. Hwang, Selective intermolecular zero-quantum coherence in high-resolution NMR under inhomogeneous fields, Chem. Phys. Lett. 386 (2004) 200–205, https://doi.org/10.1016/j.cplett.2004.01.055.

[94] G. Galiana, R.T. Branca, W.S. Warren, Ultrafast intermolecular zero quantum spectroscopy, J. Am. Chem. Soc. 127 (2005) 17574–17575, https://doi.org/10.1021/ja054463m.

[95] X.Q. Zhu, Z. Chen, S.H. Cai, J.H. Zhong, Selection of intra- or inter-molecular multiple-quantum coherences in NMR of highly polarized solution, Phys. B 362 (2005) 286–294, https://doi.org/10.1016/j.physb.2005.02.026.

[96] D.Z. Balla, G. Melkus, C. Faber, Spatially localized intermolecular zero-quantum coherence spectroscopy for in vivo applications, Magn. Reson. Med. 56 (2006) 745–753, https://doi.org/10.1002/mrm.21007.

[97] D. Z. Balla, C. Faber, Localized intermolecular zero-quantum coherence spectroscopy in vivo, Conc. Magn. Reson. 32 A (2008) 117-133. DOI: 10.1002/cmr.a.20104.

[98] C. Faber, Resolution enhancement in vivo NMR spectroscopy, Annu. Rep. NMR Spectroscopy 61 (2007) 1–50, https://doi.org/10.1016/S0066-4103(07)61101-6.

[99] W.P. Aue, J. Kahran, R.R. Ernst, Homonuclear broad band decoupling and two-dimensional J-resolved NMR spectroscopy, J. Chem. Phys. 64 (1976) 4226–4227, https://doi.org/10.1063/1.431994.

[100] M. Liu, X. Zhang, Multiple-quantum J-resolved NMR spectroscopy (MQ-JRES) measurement of multiple-quantum relaxation rates and relative signs of spin coupling constants, J. Magn. Reson. 146 (2000) 277–282, https://doi.org/10.1006/jmre.2000.2149.

[101] B. Baishya, N. Suryapraksh, Spin selective multiple quantum NMR for spectral simplification, determination of relative signs, and magnitudes of scalar couplings by spin state selection, J. Chem. Phys. 127 (2007) 214510–221451, https://doi.org/10.1063/1.2803900.

[102] B. Baishya, N. Suryapraksh, Spin state selective detection of single quantum transitions using multiple quantum coherence: Simplifying the analyses of complex NMR spectra, J. Phys. Chem. A 111 (2007) 5211–5217, https://doi.org/10.1021/jp071187k.

[103] L. Frydman, D. Blazina, Ultrafast two-dimensional nuclear magnetic resonance spectroscopy of hyperpolarized solutions, Nat. Phys. 3 (2007) 415–419, https://doi.org/10.1038/nphys597.

[104] Y.Y. Lin, N. Lisitza, S.D. Ahn, W.S. Warren, Resurrection of crushed magnetization and chaotic dynamics in solution NMR spectroscopy, Science 290 (2000) 118–121, https://doi.org/10.1126/science.290.5489.118.

[105] D.Z. Balla, C. Faber, Solvent suppression in liquid state NMR with selective intermolecular zero-quantum coherences, Chem. Phys. Lett. 393 (2004) 464–469, https://doi.org/10.1016/j.cplett.2004.06.087.

[106] Z. Chen, S.H. Cai, Z.W. Chen, J.H. Zhong, Fast Acquisition of high-resolution NMR spectra in inhomogeneous fields via intermolecular double-quantum coherences, J. Chem. Phys. 130 (2009) 084504, https://doi.org/10.1063/1.3076046.

[107] Y.Q. Lin, Z. Chen, S.H. Cai, Z.W. Chen, J.H. Zhong, High-resolution J-scaling nuclear magnetic resonance spectra in inhomogeneous fields via intermolecular multiple-quantum coherences, Appl. Spectrosc. 63 (2009) 585–590. https://opg.optica.org/as/abstract.cfm?URI=as-63-5-585.

[108] Y. Huang, S.H. Cai, Y.Q. Lin, Z. Chen, An intermolecular single-quantum coherence detection scheme for high-resolution two-dimensional J-resolved spectroscopy in inhomogeneous fields, Appl. Spectrosc. 64 (2010) 235–240. https://opg.optica.org/as/abstract.cfm?URI=as-64-2-235.

[109] C. Wang, L. Zhang, Z. Wie, L. Lin, Z. Chen, High-resolution NMR spectroscopy via simultaneous acquisition of intermolecular zero- and double-quantum coherence signals in inhomogeneous magnetic fields, Chem. Phys. Lett. 625 (2015) 41–47, https://doi.org/10.1016/j.cplett.2015.02.028.

[110] M. Garwood, I. DelaBarre, The return to the frequency seep: designing adiabatic pulses for contemporary NMR, J. Magn. Reson. 153 (2001) 155–177, https://doi.org/10.1006/jmre.2001.2340.

[111] W. Barros Jr., D.F. Gochberg, Fast single-gradient simultaneous measurements of D and T_2 in liquid via the distant dipolar field, Chem. Phys. Lett. 431 (2006) 174–178, https://doi.org/10.1016/j.cplett.2006.09.033.

[112] J. Zhong, Z. Chen, E. Kwok, S. Kennedy, Enhanced sensitivity to molecular diffusion with intermolecular double-quantum coherences: implications and potential applications, Magn. Reson. Imag. 19 (2001) 33–39, https://doi.org/10.1016/S0730-725X(01)00223-5.

[113] J. Jeener, Macroscopic molecular diffusion in liquid NMR, revised, Conc. Magn. Reson. 14 (2002) 79–88, https://doi.org/10.1002/cmr.10006.

[114] W. Barros Jr., J.C. Gore, D.F. Gochberg, Simultaneous measurements of D and T_2 in liquid using the distant dipolar field, Chem. Phys. Lett. 431 (2006) 174–178, https://doi.org/10.1016/j.jmr.2005.09.013.

[115] Y.Q. Huang, S.H. Cai, X. Chen, Z. Chen, Intermolecular single-quantum coherence sequences for high-resolution NMR spectra in inhomogeneous fields, J. Magn. Reson. 203 (2010) 100–107, https://doi.org/10.1016/j.jmr.2009.12.007.

[116] X. Cui, J. Bao, Y. Huang, S. Cai, Z. Chen, In vivo spatial localized high resolution 1H MRS via intermolecular single-quantum coherence of rat brain at 7 T, J. Magn. Reson. Imag. 37 (2013) 359–364, https://doi.org/10.1002/jmri.23839.

[117] Y.Q. Lin, T.L. Gu, Z. Chen, S. Kennedy, M. Jakob, J.H. Zhong, High-resolution MRS in the presence of filed inhomogeneity via intermolecular double-quantum coherences on a 3 T whole body scanner, Magn. Reson. Med. 63 (2011) 303–310, https://doi.org/10.1002/mrm.22224.

[118] Y.Q. Lin, Z. Zhang, S. Cai, Z. Chen, Spatially-encoded intermolecular single-quantum coherence method for high-resolution NMR spectra in inhomogeneous fields, Chem. Phys. Lett. 634 (2015) 11–15, https://doi.org/10.1016/j.cplett.2015.05.030.

[119] P. A. Bottomley, Selective volume method for performing localized NMR spectroscopy, U. S. patent 4480228. 1984.

[120] W. Richter, S. Lee, W.S. Warren, Q. He, Imaging with intermolecular multiple-quantum coherences in solution nuclear magnetic resonance, Science 267 (1995) 654–657, https://doi.org/10.1126/science.7839140.

[121] R. Bowtell, P. Robyr, Structural investigation with the dipolar demagnetization field in solution NMR, PhysRevLett. 76 (1996) 4971–4974, https://doi.org/10.1103/PhysRevLett.76.4971.

[122] P. Robyr, R. Bowtell, Measuring Patterson functions of inhomogeneous liquids using the nuclear dipolar field, J. Chem. Phys. 107 (1997) 702–706, https://doi.org/10.1063/1.474435.

[123] P. Robyr, R. Bowtell, Nuclear magnetic resonance microscopy in liquids using the dipolar field, J. Chem. Phys. 106 (1997) 467–476, https://doi.org/10.1063/1.473388.

[124] A. Barrall, L. Frydman, G.C. Chingas, NMR diffraction and spatial statistics of stationary systems, Science 255 (1992) 714–717, https://doi.org/10.1126/science.255.5045.714.

[125] C. Ramanathan, R.W. Bowtell, NMR imaging and structure measurements using the long-range dipolar field in liquids, PhysRevE 66 (2002) 041201–041210, https://doi.org/10.1103/PhysRevE.66.041201.

[126] S. Gutteridge, C. Ramanathan, R. W. Bowtell, Mapping the absolute value of M_0 using dipolar field effects. DOI: 10.1002/mrm.10142 .

[127] S. Mori, R.E. Hurd, P.C.M. van Zijl, Imaging of shifted stimulated echoes and multiple spin echoes, Magn. Reson. Med. 37 (1997) 336–340, https://doi.org/10.1002/mrm.1910370305.

[128] A. Bifone, G.S. Payne, M.O. Leach, In vivo multiple spin echoes, J. Magn. Reson. 135 (1998) 30–36, https://doi.org/10.1006/jmre.1998.1540.

[129] R.J. Ordidge, A. Connelly, J.A.B. Lohman, Image-selected in vivo spectroscopy (ISIS). A new technique for spatially selective nmr spectroscopy, J. Magn. Reson. 66 (1986) 283–294, https://doi.org/10.1016/0022-2364(86)90031-4.

[130] J. Frahm, K.D. Merboldt, W. Hanicke, A. Hasse, Stimulated echo imaging, J. Magn. Reson. 64 (1985) 81–93, https://doi.org/10.1016/0022-2364(85)90033-2.

[131] S. Capuani, F. Curzi, F.M. Alexandri, B. Maraviglia, A. Bifone, Characterization of trabecular bone by dipolar demagnetization field MRI, J. Magn. Med. 46 (2001) 683–689, https://doi.org/10.1002/mrm.1246.

[132] S. Capuani, M. Alesiani, F.M. Alessandri, B. Maraviglia, Characterization of porous media structure by nonlinear NMR methods, Magn. Reson. Imag. 19 (2001) 319–323, https://doi.org/10.1016/s0730-725x(01)00243-0.

[133] R.R. Rizi, S. Ahn, D.C. Alsop, S. Garrett-Roe, M. Mescher, W. Richter, M. D. Schnall, J.S. Leigh, W.S. Warren, Intermolecular zero-quantum coherence imaging of the human brain, Magn. Reson. Med. 43 (2000) 627–632, https://doi.org/10.1002/(SICI)1522-2594(200005)43:5<627::AID-MRM2>3.0.CO;2-J.

[134] W.S. Warren, S. Ahn, R.R. Rizi, J. Hopkins, J.S. Leigh, M. Mescher, W. Richter, M. Garwood, K. Ugurbil, MR imaging contrast enhancement based on intermolecular zero quantum coherences, Science 281 (1998) 247–251, https://doi.org/10.1126/science.281.5374.247.

[135] W. Richter, M. Richter, W.S. Warren, H. Merkel, P. Andersen, G. Adriany, K. Ugurbil, Functional magnetic resonance imaging with intermolecular multiple-quantum coherences, Magn. Reson. Imaging 18 (2000) 489–494, https://doi.org/10.1016/S0730-725X(00)00133-8.

[136] J. Zhong, Z. Chen, E. Kwok, In vivo intermolecular double-quantum imaging on a clinical 1.5T MR scanner, Magn. Reson. Med. 43 (2000) 335-341. DOI: 10.1002/(SICI)1522-2594(200003)43:3<335::AID-MRM3>3.0.CO;2-1.

[137] J. Zhong, Z. Chen, E. Kwok, New image contrast mechanisms in inter-molecular double-quantum coherence human MR imaging, J. Magn. Reson. Imag. 12 (2000) 311–320, https://doi.org/10.1002/1522-2586(200008)12:2<311::AID-JMRI14>3.0.CO;2-6.

[138] J. Zhong, E. Kwok, Z. Chen, fMRI of auditory stimulation with intermolecular double-quantum coherences (iDQCs) at 1.5T, Magn. Reson. Med. 45 (2001) 356-364. DOI: 10.1002/1522-2594(200103)45:3<356::aid-mrm1046>3.0.co;2-5 .

[139] J. Zhong, Z. Chen, E. Kwok, S.K. Kennedy, Z. You, Optimization of BOLD sensitivity in MR imaging using intermolecular double-quantum coherences (iDQC), J. Magn. Reson. Imag. 16 (2002) 733–740, https://doi.org/10.1002/jmri.10208.

[140] A. Schäfer, T.H. Jochimsen, H.E. Möller, Functional magnetic resonance imaging with intermolecular double-quantum coherences at 3T, Magn. Reson. Med. 53 (2005) 1402–1408, https://doi.org/10.1002/mrm.20506.

[141] A. Schäfer, H.E. Möller, Functional contrast based on intermolecular double-quantum coherences: influence of the correlation distance, Magn. Reson. Med. 58 (2007) 696–704, https://doi.org/10.1002/mrm.21406.

[142] T. Gu, S.D. Kennedy, Z. Chen, K.A. Scheneider, J. Zhong, Functional MRI at 3T intermolecular double-quantum coherence (iDQC) with spin-echo (SE) acquisition, Magn. Reson. Mater. Phys. 20 (2007) 255–264, https://doi.org/10.1007/s10334-007-0093-z.

[143] A. Schäfer, S. Zysset, W. Heinke, H.E. Möller, Hypercapnia-induced effects on image contrast based on intermolecular double-quantum coherences, Magn. Reson. Med. 60 (2008) 1306–1312, https://doi.org/10.1002/mrm.21768.

[144] C. Faber, C. Heil, B. Zahneisen, D.Z. Balla, R. Bowtell, Sensitivity to local dipolar fields in the CRAZED experiment: An approach to bright spot MRI, J. Magn. Reson. 182 (2006) 315–324, https://doi.org/10.1016/j.jmr.2006.05.002.

[145] A.T. Markkola, H.J. Aronen, T. Paavonen, E. Hopsu, L.M. Sipila, J.I. Tanttu, Sepponen, Spin lock magnetization transfer imaging of head and neck tumors, Radiology 200 (1996) 369–375, https://doi.org/10.1148/radiology.200.2.8685328.

[146] H.I. Gröhn, S. Michaeli, M. Garwood, R.A. Kauppinen, O.H.J. Gröhn, Quantitative $T_{1\rho}$ and adiabatic Carr-Purcell T_2 magnetic resonance imaging of human occipital lobe at 4 T, Magn. Reson. Med. 54 (2005) 14–19, https://doi.org/10.1002/mrm.20536.

[147] B. Zheng, Z. Chen, S.D. Kennedy, J. Zhong, iDQC MRI weighted by longitudinal relaxation in the rotating frame, Magn. Reson. Med. 56 (2006) 327–333, https://doi.org/10.1002/mrm.20954.

[148] B.W. Zheng, D.W. Hwang, Z. Chen, S.D. Kennedy, L.P. Hwang, Magn. Reson. Med. 53 (2005) 930–936, https://doi.org/10.1002/mrm.20432.

[149] X. Tang, H. Ong, K. Shannon, W.S. Warren, Simultaneously acquisition of multiple orders of intermolecular multiple-quantum coherences images, Magn. Reson. Imaging 21 (2003) 1141–1149, https://doi.org/10.1016/j.mri.2003.08.015.

[150] G.D. Charles-Edwards, G.S. Pyne, M.O. Leach, A. Bifane, Effects of residual single-quantum coherences in intermolecular multiple-quantum coherence studies, J. Magn. Reson. 166 (2004) 215–227, https://doi.org/10.1016/j.jmr.2003.10.017.

[151] S. Garrett-Roe, W.S. Warren, Numerical studies of intermolecular multiple quantum coherences: high-resolution NMR in inhomogeneous fields and contrast enhancement in MRI, J. Magn. Reson. 146 (2000) 1–13, https://doi.org/10.1006/jmre.2000.2096.

[152] S.D. Wolff, R.S. Balaban, Magnetization transfer contrast (MTC) and tissue water proton relaxation in vivo, Magn. Reson. Med. 10 (1989) 135–144, https://doi.org/10.1002/mrm.1910100113.

[153] K.M. Ward, A.H. Aletras, R.S. Balaban, A new class of contrast agents for MRI based on proton chemical exchange dependent saturation transfer (CEST), J. Magn. Reson. 143 (2000) 79–87, https://doi.org/10.1006/jmre.1999.1956.

[154] M. Woods, D.E. Woessner, A.D. Sherry, Paramagnetic lanthanide complexes as PARACEST agents for medical images, Chem. Soc. Rev. 35 (2006) 500–511, https://doi.org/10.1039/B509907M.

[155] M. Zaiss, M. Schuppert, A. Deshmane, K. Herz, P. Ehses, L. Füllbier, T. Lindig, B. Bender, U. Ernemann, K. Scheffler, Chemical exchange saturation transfer MRI contrast in the human brain at 9.4 T, NeuroImage 179 (2018) 144–155, https://doi.org/10.1016/j.neuroimage.2018.06.026.

[156] M. Goldman, L. Shen, Spin-spin relaxation in LaF_3, PhysRev. 144 (1966) 321–331, https://doi.org/10.1103/PhysRev.144.321.

[157] H.T. Edzes, E.T. Samulski, Cross relaxation and spin diffusion in proton NMR of hydrated collagen, Nature 265 (1977) 521–523, https://doi.org/10.1038/265521a0.

[158] A. Neufeld, U. Eliav, G. Navon, New MRI method with contrast based on macromolecular characteristics of tissues, Magn. Reson. Med. 50 (2003) 229–234, https://doi.org/10.1002/mrm.10546.

[159] D. Carasso, U. Eliav, G. Navon, Nuclear magnetic resonance parameters for monitoring coagulation in liver tissue, Magn. Reson. Med. 54 (2005) 1082–1086, https://doi.org/10.1002/mrm.20693.

[160] U. Eliav, G. Navon, Enhancement of magnetization transfer effects by inter-molecular multiple quantum filtered NMR, J. Magn. Reson. 190 (2008) 149–153, https://doi.org/10.1016/j.jmr.2007.09.017.

[161] P. Wurst, B. Hildebrandt, G. Sreenivasa, B. Rau, J. Gellermann, H. Riess, R. Felix, P.M. Schlag, Hyperthermia in combined treatment of cancer, Lancet Oncl. 3 (2002) 487–497, https://doi.org/10.1016/s1470-2045(02)00818-5.

[162] M.H. Falk, R.D. Issels, Hyperthermia in oncology, Int. J. Hyperthermia 17 (2001) 1–18, https://doi.org/10.1080/02656730118511.

[163] H. Furusawa, K. Namba, S. Thomses, F. Akiyama, A. Bendet, C. Tanaka, Y. Yasuda, H. Nakahara, Magnetic resonance-guided focused ultrasound surgery of breast cancer: Reliability and effectiveness, J. Am. Coll. Surg. 23 (2006) 54–63, https://doi.org/10.1016/j.jamcollsurg.2006.04.002.

[164] A.N. Mirza, B.D. Fornage, N. Sneige, H.M. Kuerer, L.A. Newmann, F.C. Ames, E. Singletary, Radiofrequency ablation of solid tumors, Cancer J. 7 (2001) 95–102. PMID:11324771.

[165] J. De Poorter, Noninvasive MRI thermometry with the proton-resonance frequency method: Study of susceptibility effects, Magn. Reson. Med. 34 (1995) 359–367, https://doi.org/10.1002/mrm.1910340313.

[166] J. De Poorter, C. Dewagter, Y. Dedeene, C. Thomson, F. Stahlberg, E. Achten, Noninvasive MRT thermometry with the proton-resonance frequency (PRF) method- In vivo results in human muscle, Magn. Reson. Med. 33 (1995) 74–81, https://doi.org/10.1002/mrm.1910330111.

[167] J.W. Gellermann, W. Feussner, A. Fähling, H. Nadobny, B. Hilderbrandt, R. Felix, P. Wurst, Method and potential of magnetic resonance imaging for monitoring radiofrequency hyperthermia in a hybrid system, Int. J. Hyperthermia 21 (2005) 497–513, https://doi.org/10.1080/02656730500070102.

[168] Y. Ishihara, A. Calderon, H. Watanabe, K. Okamoto, Y. Suzuki, K. Kuroda, Y. Suzuki, Precise and fast temperature mapping using water proton chemical shift, Magn. Reson. Med. 34 (1995) 814–823, https://doi.org/10.1002/mrm.1910340606.

[169] V. Rieke, K.B. Pauly, MR thermometry, J. Magn. Reson. Imaging 27 (2008) 376–390, https://doi.org/10.1002/jmri.21265.

[170] N. McDonnald, Quantitative MRI-based temperature mapping based on proton resonance frequency shift: Review of validation studies, Int. J. Hyperthermia 21 (2005) 533–546, https://doi.org/10.1080/02656730500096073.

[171] R. Stollberger, P.W. Asher, D. Huber, W. Renhart, H. Radner, F. Ebner, Temperature monitoring of interstitial thermal tissue coagulation using MR phase images, J. Magn. Reson. Imaging 8 (1998) 188–196, https://doi.org/10.1002/jmri.1880080132.

[172] G. Galiana, R.T. Branca, E.R. Jenista, W.S. Warren, Accurate temperature imaging based on intermolecular coherences in magnetic resonance, Science 17 (2008) 421–424, https://doi.org/10.1126/science.1163242.

[173] E.R. Jenista, R.T. Branca, W.S. Warren, Absolute temperature imaging using intermolecular multiple quantum MRI, Int. J. Hyperthermia 26 (2010) 725–734, https://doi.org/10.3109/02656736.2010.499527.

[174] E.B. Cady, P.C. Dsouza, J. Penrice, A. Lorek, The estimation of local brain temperature by in-vivo H-1 magnetic resonance spectroscopy, Magn. Reson. Med. 33 (1995) 862–867, https://doi.org/10.1002/mrm.1910330620.

[175] K. Hynynen, N. McDonald, R.V. Mulkern, F.A. Jolesz, Temperature mapping in fat using the water proton chemical shift, Magn. Reson. Med. 43 (2000) 901–904, https://doi.org/10.1002/1522-2594(200006)43:6<901::AID-MRM18>3.0.CO;2-A.

[176] I. Marshall, B. Karaszewski, J.M. Wardlaw, V. Cvoro, K. Wartolowska, P. A. Armitage, T. Carpenter, M.E. Bastin, A. Farrall, K. Haga, Measurement of regional brain temperature using proton spectroscopic imaging: validation and application to acute ischemic stroke, J. Magn. Reson. Imaging 24 (2006) 699–706, https://doi.org/10.1016/j.mri.2006.02.002.

[177] E.R. Jenistry, G. Galiana, R.T. Branca, P.S. Yarmolenko, A.M. Stokes, M. W. Dewhirst, W.S. Warren, Application of mixed spin iMQCs for temperature and chemical-selective imaging, J. Magn. Reson. 204 (2010) 208–218, https://doi.org/10.1016/j.jmr.2010.02.021.

[178] J. Hennig, A. Nauerth, H. Friedburg, RARE imaging - a fast imaging method for clinical MR, Magn. Reson. Med. 3 (1986) 823–833, https://doi.org/10.1002/mrm.1910030602.

[179] J.T. Schneider, C. Faber, BOLD imaging in the mouse brain using a TurboCREZED sequence at high magnetic fields, Magn. Reson. Med. 60 (2008) 850–859, https://doi.org/10.1002/mrm.21716.

[180] T.E. Budinger, M.D. Bird, L. Frydman, J.R. Long, T.H. Mareci, W.D. Rooney, B. Rosen, J.E. Schneck, V.S. Springer, A.D. Sherry, D.K. Sodickson, C.S. Springer, K.R. Thuiborn, K. Ugurbil, L.L. Wald, Toward 20 T magnetic resonance for human brain studies: opportunities for discovery and neuroscience rationale, MAGMA 29 (2016) 617–639, https://doi.org/10.1007/s10334-016-0561-4.

[181] T.E. Budinger, M.D. Bird, MRI and MRS of the human brain at magnetic fields of 14 T to 20 T: Technical feasibility, safety, and neuroscience horizons, Neuroimage 168 (2018) 509–531, https://doi.org/10.1016/j.neuroimage.2017.01.067.

[182] D. Ivanov, F. DeMartini, E. Formisa, F.J. Fritz, R. Goebel, L. Huber, G. Kemper, D. Kurban, S. Kashyap, V.G. Kemper, D. Kurban, A. Roebroeck, S. Sengupta, B. Sorger, D.H.Y. Tse, K. Uludag, C.J. Wiggins, B.A. Poser, Magnetic resonance imaging at 9.4 T: The Maastricht journey, MAGMA 36 (2023) 159–173, https://doi.org/10.1007/s10334-023-01080-4.

[183] S. Bates, S.O. Dumoulin, P.J.M. Folkers, E. Formisano, R. Goebel, A. Haghnejad, R.C. Helmich, D. Klomp, A.G. van der Kolk, Y. Li, A. Nederveen, D.G. Norris, N. Petridou, S. Roeil, T.W.J. Schenen, M.M. Schoonheim, I. Voogt, A version of 14 T MR for fundamental and clinical science, MAGMA 36 (2023) 211–225, https://doi.org/10.1007/s10334-023-01081-3.

[184] T. Meersmann, M. Schwager, V. Varma, G. Bodenhausen, Little-known advantages of very high fields in NMR, J. Magn. Reson. A 119 (1996) 275–279, https://doi.org/10.1006/jmra.1996.0087.

[185] J.S. Brooks, J.E. Crow, W.G. Moulton, Science opportunities at high magnetic fields, J. Phys. Chem. Solids 59 (1997) 569–590, https://doi.org/10.1016/S0022-3697(97)90232-8.

[186] V. D. Schepkin, B. M. Odintsov, I. Litvak, P.L. Goŕkov, W. W. Brey, A. Neubauer, F. Budinger, Efficient detection of bound potassium and sodium using TQTPPI pulse sequence, Proceedings of International Society for Magnetic Resonance in Medicine, vol. 23 (2015) p. 2375.

[187] M. Munowitz, A. Pines, Multiple-quantum nuclear magnetic resonance, Science 233 (1986) 525–531, https://doi.org/10.1126/science.233.4763.525.

[188] Y.-Y. Lin, S. Ahn, N. Murali, W. Brey, C.R. Bowers, W.S. Warren, High-resolution, >1 GHz NMR in unstable magnetic fields, PhysRevLett. 85 (2000) 3732–3735, https://doi.org/10.1103/PhysRevLett.85.3732.

[189] H.Y. Carr, E.M. Purcell, Effect of diffusion on free precession in nuclear magnetic resonance experiments, PhysRev. 94 (1954) 630–638, https://doi.org/10.1103/PhysRev.94.630.

[190] K. Pervushin, R. Riek, G. Wider, K. Wüthrich, Attenuated T2 relaxation by mutual cancellation of dipole-dipole coupling and chemical shift anisotropy indicates an avenue to NMR structures of very large biological macromolecules in solutions, Proc. Natl. Acad. Sci. u.s.a. 94 (1997) 12366–12371, https://doi.org/10.1073/pnas.94.23.12366.

[191] R.A. Green, R.W. Adams, S.B. Duckett, R.E. Merwis, D.C. Williamson, G.G. R. Green, The theory and practice of hyperpolarization in magnetic resonance using parahydrogen, Prog. Nucl. Magn. Reson. Spectroscop. 67 (2012) 1–48, https://doi.org/10.1016/j.pnmrs.2012.03.001.

[192] J. Brossel, A. Kastler, La detection de la resonance magnetique des niveaux excites-leffect de depolarization des radiations de resonance optique et de fluorescence, Comp. Rendu, Hebdomadaires Seances L Acad. Sci. 229 (1949) 1213–1215.

[193] A. Kastler, Optical methods of atomic orientation and of magnetic resonance, J. Opt. Soc. Am. 47 (1957) 460–465, https://doi.org/10.1364/JOSA.47.000460.

[194] A. Abragam, M. Goldman, Principles of dynamic nuclear polarization, Rep. Prog. Phys. 41 (1978) 395-, https://doi.org/10.1088/0034-4885/41/3/002.

[195] D.A. Hall, D.G. Maus, G.J. Gerfen, S.J. Inati, L.R. Becerra, F.W. Dahlquist, R. G. Griffin, Polarization-enhanced NMR spectroscopy of biomolecules in frozen solution, Science 276 (1997) 930–932, https://doi.org/10.1126/science.276.5314.930.

[196] C.R. Bowers, D.P. Weitekamp, Transformation of symmetrization order to nuclear-spin magnetization by chemical reaction and nuclear magnetic resonance, PhysRevLett. 57 (1986) 2645–2648, https://doi.org/10.1103/PhysRevLett.57.2645.

[197] S.B. Duckett, C.J. Sleigh, Application of parahydrogen phenomenon: a chemical perspective, Prog. Nucl. Magn. Reson. Spectrosc. 34 (1999) 71–92, https://doi.org/10.1016/S0079-6565(98)00027-2.

[198] M.A. Bouchiat, T.R. Carver, C.M. Varnum, Nuclear polarization in 3He gas induced by optical pumping and dipolar exchange, Phys. Rev. Lett. a: at. Mol. Opt. Phys. 58 (1998) 1412–1439, https://doi.org/10.1103/PhysRevLett.5.373.

[199] T.G. Walker, W. Happer, Spin-exchange optical pumping of noble-gas nuclei, RevModPhys. 69 (1997) 629–642, https://doi.org/10.1103/RevModPhys.69.629.

[200] E. Babcock, B. Chann, T.G. Walker, W.C. Chen, T.R. Gentile, Limits to the polarization for spin-exchange optical pumping of ^{3}He, PhysRevLett. 96 (2006) 083003, https://doi.org/10.1103/PhysRevLett.96.083003.

[201] B.M. Goodson, Nuclear magnetic resonance of laser-polarized noble gases in molecules, materials, and organisms, J. Magn. Reson 155 (2002) 157–216, https://doi.org/10.1006/jmre.2001.2341.

[202] N.J. Shah, T. Unlu, H.-P. Wegener, H. Halling, K. Zilles, S. Appelt, Measurement of rubidium and xenon absolute polarization at high temperatures as a means of improving production of hyperpolarized ^{129}Xe, NMR Biomed. 13 (2000) 214–219, https://doi.org/10.1002/1099-1492(200006)13:4<214::AID-NBM634>3.0.CO;2-G.

[203] A. Cherubini, A. Bifone, Hyperpolarized xenon in biology, Prog. Nucl. Magn. Reson. Spectrosc. 43 (2003) 1–30, https://doi.org/10.1016/S0079-6565(02)00052-3.

[204] D.H. Hall, D.G. Maus, G.J. Gerfen, I.R. Inati, F.W. Becerra, F.W. Dahlquist, R. G. Griffin, Polarization-enhanced NMR spectroscopy of biomolecules in frozen solutions, Science 276 (1997) 930–932, https://doi.org/10.1126/science.276.5314.930.

[205] A. Abragam, M. Goldman, Nuclear magnetism: order and disorder, Clarendon Press, 1982.

[206] J.H. Ardenkjaer-Larsen, B. Friedlund, A. Gram, G. Hannson, L. Hannson, M. H. Lerch, R. Servin, K. Thaning, K. Golman, Increase in signal-to-noise at >10,000 in liquid state NMR, Proc. Nat. Am. Soc. 100 (2003) 10158–10161, https://doi.org/10.1073/pnas.1733835100.

[207] R.W. Adams, J.A. Aguilar, K.D. Atkinson, M.J. Cowley, P.I.P. Elliot, S.B. Duckett, G.G. Green, I.G. Khazal, J. López-Serrano, D.C. Williamson, Science 323 (2009) 1708–1711, https://doi.org/10.1126/science.1168877.

[208] K.D. Atkinson, M.J. Cowley, P.I.P. Elliot, S.B. Duckett, G.G.R. Green, J. López-Serrano, A.C. Whitwood, Spontaneous transfer of parahydrogen derived spin order to pyridine at low magnetic field, J. Am. Chem. Soc. 131 (2009) 13362–13368, https://doi.org/10.1021/ja903601p.

[209] M. Emondts, D. Schikowski, J. Klankermayer, P.P.M. Schleker, Non-pairwise interactions in parahydrogen experiments: nuclear exchange of single protons enables bulk water hyperpolarization, ChemPhysChem 19 (2018) 2614–2620, https://doi.org/10.1002/cphc.201800521.

[210] K.-O. Brenske, M. Emondts, S.T. Hörning, S. Panitz, M.I. Pieper, A. Ligori, A. Schascht, J. Henkel, J. Klankermayer, A. Herrmann, Parahydrogen-induced polarization of a labeled cancer-targeting DNA aptamer, Angew. Chem. Int. Ed. 62 (2023) e20230531, https://doi.org/10.1002/anie.202300531.

[211] S.L. Eriksson, J.R. Lindale, X. Li, W.S. Warren, Improving SARBE hyperpolarization with highly nonintuitive pulse sequences: moving beyond avoided crossing to describe dynamics, Sci. Adv. 8 (2022) eabl3708, https://doi.org/10.1126/sciadv.abl3708.

[212] S.W. Morgan, E. Baudin, G. Huber, P. Berthault, G. Tastevin, M. Goldman, P.-J. Nacher, H. Desvaux, Multiple echoes due to distant dipolar fields in hyperpolarized noble gas solutions, Eur. Phys. J. D 67 (2013) 29–38, https://doi.org/10.1140/epjd/e2012-30470-0.

[213] E.R. Jenista, R.T. Branca, W.S. Warren, Hyperpolarized carbon-carbon intermolecular multiple quantum coherences, J. Magn. Reson. 196 (2008) 74–77, https://doi.org/10.1016/j.jmr.2008.09.027.

[214] M. Mishkovshy, U. Eliav, G. Navon, L. Frydman, Nearly 10^6-fold enhancement in intermolecular ^{1}H double-quantum NMR experiments by nuclear hyperpolarization, J. Magn. Reson. 200 (2009) 142–146, https://doi.org/10.1016/j.jmr.2009.06.002.

[215] M.S. Conradi, B.T. Saam, D.A. Yablonskiy, J.C. Woods, Hyperpolarized ^{3}He and perfluorocarbon gas diffusion MRI of lungs, Prog. Nucl. Magn. Reson. Spectrosc. 48 (2006) 63–83, https://doi.org/10.1016/j.pnmrs.2005.12.001.

[216] R.H. Acosta, P. Blümer, K. Münnemann, H.-W. Spiess, Mixture and dissolution of laser polarized noble gases: Spectroscopic and imaging applications, Prog. Nucl. Magn. Reson. Spectrosc. 66 (2012) 40–69, https://doi.org/10.1016/j.pnmrs.2012.03.003.

[217] P.P. Zänker, J. Schmidt, J. Schmiedeskamp, R.H. Acosta, H.-W. Spiess, Spin echo formation in the presence of stochastic dynamics, PhysRevLett. 99 (2007) 263001, https://doi.org/10.1103/PhysRevLett.99.263001.

[218] A. Shafer, H.E. Möller, Functional contrast based on intermolecular double-quantum coherences: influence of the correlation distance, Magn. Reson. Med. 58 (2007) 696–704, https://doi.org/10.1002/mrm.21406.

[219] D. Candela, M.E. Hayden, P.J. Nacher, Steady-state production of high nuclear polarization in ^{3}H-^{4}He mixture, PhysRevLett. 73 (1994) 2587–2590, https://doi.org/10.1103/PhysRevLett.73.2587.

[220] K.L. Sauer, F. Marion, P.J. Nacher, G. Tatevin, NMR instabilities and spectral clustering in laser-polarized liquid xenon, PhysRevB 63 (2001) 184427, https://doi.org/10.1103/PhysRevB.63.184427.

[221] J. Jenner, Dynamical effects of the dipolar field inhomogeneities in high-resolution NMR: spectra clustering and instabilities, PhysRevLett. 82 (1999) 1772–1775, https://doi.org/10.1103/PhysRevLett.82.1772.

[222] J. Jenner, Collective effects in liquid NMR: dipolar field and radiation damping, in: D.M. Grant, R.K. Harris (Eds.), Encyclopedia of NMR, vol. 9, Wiley, 2002, p. 642.

[223] P.J. Nacher, G. Tastevin, B. Villard, N. Piegay, F. Marionb, K.L. Sauer, NMR instabilities in spin-polarized liquids: ^{3}He-^{4}He mixtures and ^{129}Xe, J. Low Temp. Phys. 121 (2000) 743–750, https://doi.org/10.1023/A:1017512921929.

[224] M. Ledbetter, M. Romalis, Nonlinear effects from dipolar interactions in hyperpolarized liquid ^{129}Xe, PhysRevLett. 89 (2002) 287601–287604, https://doi.org/10.1103/PhysRevLett.89.287601.

[225] Y.M. Chen, R.T. Branca, W.S. Warren, Revisiting the mean-field picture of dipolar effects in solution NMR, J. Chem. Phys. 136 (2012) 204509–204511, https://doi.org/10.1063/1.4721637.

[226] E. Stoltz, J. Tannenhauser, P.J. Nacher, Effect of dipolar field in highly magnetized samples of liquid ^{3}He-^{4}He mixtures, J. Low Temp. Phys. 101 (1995) 839–844, https://doi.org/10.1007/BF00753400.

[227] W.-K. Rhim, A. Pines, J.S. Waugh, Time-reversal experiments in dipolar-coupled spin system, PhysRevB 3 (1971) 684–695, https://doi.org/10.1103/PhysRevB.3.684.

[228] D.E. Demco, Tetrahedral magic echo, Phys. Lett. A 45 (1973) 113–114, https://doi.org/10.1016/0375-9601(73)90447-7.

[229] S. Matsui, Solid-state NMR imaging by magic sandwich echoes, Chem. Phys. Lett. 179 (1991) 187–190, https://doi.org/10.1016/0009-2614(91)90313-X.

[230] D.E. Demco, S. Hafner, R. Kimmich, Spatially resolved homonuclear NMR. III. Magic-echo and rotary magic-echo encoding imaging, J. Magn. Reson. 96 (1991) 307–322, https://doi.org/10.1016/0022-2364(92)90084-K.

[231] S. Hafner, D.E. Demco, R. Kimmich, Magic-echoes and NMR imaging of solids, Solid State Nucl. Magn. Reson. 6 (1996) 275–293, https://doi.org/10.1016/0926-2040(96)01234-9.

[232] D.E. Demco, A. Oros-Peusquens, N.J. Shah, Molecular dynamics parameter maps by ^{1}H Hahn echo and mixed-echo phase-encoding MRI, J. Magn. Reson. 227 (2013) 1–8, https://doi.org/10.1016/j.jmr.2012.11.005.

[233] M.E. Hayden, E. Baudin, G. Tastevin, P.J. Nacher, NMR time reversal as a probe of incipient turbulent spin dynamics, PhysRevLett. 99 (2007) 137602, https://doi.org/10.1103/PhysRevLett.99.137602.

[234] M.P. Augustine, S.D. Bush, E.L. Hahn, Noise triggering of radiation damping from the inverted state, Chem. Phys. Lett. 322 (2000) 111–118, https://doi.org/10.1016/S0009-2614(00)00390-0.

[235] D.-J.-Y. Marion, G. Huber, P. Berthault, H. Desvaux, Observation of noise-triggered chaotic emissions in an NMR maser, ChemPhysChem 9 (2008) 1395–1401, https://doi.org/10.1002/cphc.200800113.

[236] D.-J.-Y. Marion, P. Berthault, H. Desvaux, Spectral and temporal features of multiple spontaneous NMR maser emissions, Eur. Phys. J. 51 (2009) 357–367, https://doi.org/10.1140/epjd/e2009-00027-7.

[237] V. Henner, H. Desvaux, T. Belozerova, D.-J.-Y. Marion, A. Petr Kharebov, Klots, Collective effects due to dipolar fields as the origin of the extremely random behavior in hyperpolarized NMR maser. A theoretical and numerical study, J. Chem. Phys. 139 (2013) 144111–144119, https://doi.org/10.1063/1.4823823.

[238] E.M.M. Weber, D. Kurzbach, D. Abergel, A DNP-hyperpolarized solid-state water NMR MASER: observation and qualitative analysis, Phys. Chem. Chem. Phys. 21 (2019) 21278–21286, https://doi.org/10.1039/c9cp03334c.

[239] V.F.T.J. Chacko, D. Abergel, Dipolar effects in solid-state NMR maser pumped by dynamic nuclear polarization, Phys. Chem. Chem. Phys. 25 (2023) 10392–10404, https://doi.org/10.1039/d2cp05696h.

[240] J.P. Marques, F.F.J. Simonis, A.G. Webb, Low-field MRI: An MR physics perspective, J. Magn. Reson. Imag. 49 (2019) 1528–1542, https://doi.org/10.1002/jmri.26637.

[241] M. Hori, A. Hagiwara, M. Goto, A. Wada, A. Aoki, Low-field magnetic resonance imaging, Invest. Radiol. 56 (2021) 669–679, https://doi.org/10.1097/RLI.0000000000000810.

[242] Y. Liu, A.T.L. Leong, Y. Zhao, L. Xiao, L. Xiao, H.K.F. Mak, A.C.O. Tsang, G.K. K. Lau, G.K.K. Leung, E.X. Wu, A low-cost and shielding-free ultra-low-field brain MRI scanner, Nat. Commun. 12 (2021) 7238, https://doi.org/10.1038/s41467-021-27317-1.

[243] T.C. Arnold, C.W. Freeman, B. Litt, J.M. Stein, Low-field MRI: Clinical promise and challenges, J. Magn. Reson. Imag. 57 (2023) 25–44, https://doi.org/10.1002/jmri.28408.

[244] A.E. Campbell-Washburn, K.E. Keenan, P. Hu, J.P. Mugler III, K.S. Nayak, A. G. Webb, J. Obungoloch, K.N. Sheth, J. Henning, M.S. Rosen, N. Salameh, D. K. Sodickson, J.M. Stein, J.P. Marques, O.P. Simonetti, Low-field MRI: A report on the, ISMARM workshop, Magn. Reson. Med. 90 (2023) (2022) 1682–1694, https://doi.org/10.1002/mrm.29743.

Glossary

BOLD: blood oxygenation level-dependent
CEST: chemical exchange saturation transfer

CSF: cerebrospinal fluid
CPMG: Carr-Purcell-Meiboom-Gill pulse sequence
COSY: correlation spectroscopy
CRAZED: correlation spectroscopy revamped by asymmetric z-gradient echo detection
DDF: distant dipolar field
DNP: dynamic nuclear polarization
EPI: spin-echo planar imaging
EPR: electron paramagnetic resonance
FLASH: fast low angle shot
IDEAL: intermolecular dipolar-interaction enhanced all lines
HeMQ: heteronuclear multiple quantum
HOMOGENIZED: homogeneity enhancement by intermolecular zero-quantum
HOT: homogenized with off-resonance transfer
iMQCs: intermolecular multiple-quantum coherences
ISIS: image-selected in vivo spectroscopy
iZQCs: intermolecular zero-quantum coherences
iDQCs: intermolecular double-quantum coherences
iSQCs: intermolecular single-quantum coherences
fMRI: functional magnetic resonance imaging
MQCs: multiple-quantum coherences
MRI: magnetic resonance imaging
MRS: magnetic resonance spectroscopy
MSE: multiple spin echoes
MTC: magnetization transfer contrast
NOSE: nonlinear stimulated echoes
PDMS: poly(dimethylsiloxane)
PHIP: parahydrogen induced polarization
PRESS: point resolved spectroscopy
RARE: rapid imaging with refocused echoes
RF: radio-frequency
SABRE: signal amplification by reversible exchange
SNR: signal-to-noise ratio
SSTE: shifted stimulated echoes
STEAM: stimulated echo acquisition mode
TEMPOL: 4-hydroxy-2,2,6,6-tetramethylpiperidine-1-oxyl
TQ: triple quantum
TROSY: transverse relaxation-optimized spectroscopy